

<https://doi.org/10.15388/vu.thesis.238>
<https://orcid.org/0000-0002-2099-1417>

VILNIUS UNIVERSITY
CENTER FOR PHYSICAL AND TECHNOLOGICAL SCIENCE

Ričardas
GOLUBEVAS

Fabrication and Evaluation of Inorganic- Organic Composites for Bone Tissue Engineering

DOCTORAL DISSERTATION

Natural Sciences,
chemistry (N 003)

VILNIUS 2021

This dissertation was written between 2015 and 2019 while studying at Vilnius University and will be defended externally.

Academic supervisor:

Assoc. Prof. Dr. Edita Garškaitė (Vilnius University, Faculty of Chemistry and Geosciences, Natural Sciences, chemistry – N 003).

This doctoral dissertation will be defended in a public meeting of the Dissertation Defence Panel:

Chairman – Prof. Habil. Dr. Albertas Malinauskas (Centre for Physical Sciences and Technology, Natural Sciences, Chemistry – N 003).

Members:

Prof. Dr. Ingrida Ancutienė (Kaunas University of Technology, Natural Sciences, Chemistry – N 003).

Assoc. Prof. Dr. Inga Grigoravičiūtė-Purionienė (Vilnius University, Natural Sciences, chemistry – N 003).

Prof. Dr. Jiri Pinkas (Masaryk University Brno, Natural Sciences, Chemistry – N 003).

Prof. Habil. Dr. Arūnas Ramanavičius (Vilnius University, Natural Sciences, Chemistry – N 003).

The dissertation shall be defended at a public/closed meeting of the Dissertation Defence Panel at 16 p.m. on 12 November 2021 in Inorganic Chemistry auditorium 141 of the Institute of Chemistry, Faculty of Chemistry and Geoscience, Vilnius University. Address: Naugarduko g. 24, LT-03225 Vilnius, Lithuania. Tel.: +370 5 2193108. Fax: +370 5 2330987.

The text of this dissertation can be accessed at the libraries of (name of the institutions granted the right to conduct doctoral studies in alphabetical order), as well as on the website of Vilnius University:

www.vu.lt/lt/naujienos/ivykiu-kalendorius

<https://doi.org/10.15388/vu.thesis.238>

<https://orcid.org/0000-0002-2099-1417>

VILNIAUS UNIVERSITETAS
FIZINIŲ IR TECHNOLOGIJOS MOKSLŲ CENTRAS

Ričardas
GOLUBEVAS

Neorganinių-organinių kompozitinių medžiagų, skirtų kaulinio audinio atstatymui, sintezė ir tyrimai

DAKTARO DISERTACIJA

Gamtos mokslai,
chemija (N 003)

VILNIUS 2021

Disertacija rengta 2015 – 2019 metais studijuojant Vilniaus universitete ir bus ginama eksternu.

Mokslinė konsultantė:

doc. dr. Edita Garškaitė (Vilniaus universitetas, Chemijos ir geomokslų fakultetas, gamtos mokslai, chemija – N 003).

Gynimo taryba:

Pirmininkas – **prof. habil. dr. Albertas Malinauskas** (Fizinių ir technologijos mokslų centras, gamtos mokslai, chemija – N 003).

Nariai:

prof. dr. Ingrida Ancutienė (Kauno technologijos universitetas, gamtos mokslai, chemija – N 003);

doc. dr. Inga Grigoravičiūtė-Purionienė (Vilniaus universitetas, gamtos mokslai, chemija – N 003);

prof. dr. Jiri Pinkas (Masaryko universitetas, Vilniaus universitetas, gamtos mokslai, chemija – N 003);

prof. habil. dr. Arūnas Ramanavičius (Vilniaus universitetas, gamtos mokslai, chemija – N 003).

Disertacija ginama viešame Gynimo tarybos posėdyje 2021 m. lapkričio mėn. 12 d. 14 val. Vilniaus universiteto Chemijos ir geomokslų fakulteto Chemijos instituto Neorganinės chemijos auditorijoje.

Adresas: Naugarduko g. 24, LT-03225 Vilnius, Lietuva. Tel.: 2193108.
Faksas: 2330987.

Disertaciją galima peržiūrėti Vilniaus universiteto, Fizinių ir technologijos mokslų centro bibliotekose ir VU interneto svetainėje adresu: <https://www.vu.lt/naujienos/ivykiu-kalendorius>

TABLE OF CONTENTS

INTRODUCTION.....	7
LIST OF SYMBOLS AND ABBREVIATIONS.....	9
1. LITERATURE REVIEW.....	10
1.1 Bone.....	10
1.2 Inorganic Biomaterials.....	12
1.2.1 Physico-Chemical Properties of Calcium Phosphates and Glass-Ceramic Materials.....	18
1.2.2 Synthesis Methods of Inorganic Biomaterials.....	21
1.2.3 Mechanical Properties of Biomaterials.....	24
1.3 Biocompatible Polymers.....	25
1.3.1 Physico-Chemical Properties of Biocompatible Polymers.....	26
1.4 Hybrid Biomaterials for Bone Scaffold Engineering.....	28
1.5 Porous Scaffolds (Polymer-Matrix Composites).....	30
1.6 Biomaterial Studies Using Computed Tomography.....	31
2. EXPERIMENTAL PART.....	35
2.1. Chemicals and Reagents.....	35
2.2. Synthesis and Processing.....	36
2.3 Characterization Techniques.....	40
3. RESULTS AND DISCUSSIONS.....	44
3.1 Glass-Ceramic (GC)-Polymethyl Methacrylate (PMMA) Composite ...	44
3.1.1 Sol-Gel Synthesis of Na-Ca-Si-P-O Glass-Ceramics.....	44
3.1.2 Structural Characterization of Na-Ca-Si-P-O Glass-Ceramics.....	45
3.1.3 Structural and Morphological Evaluation of GC-PMMA Composites	46
3.1.4 Mechanical Properties of GC-PMMA Composites.....	49
3.1.5 GC-PMMA Composite Dissolution in SBF.....	50
3.1.6 Morphological and Structural Characterization of GC-PMMA Composites after the Dissolution in SBF.....	52
3.2 Porous cHAP-Acrylate Composites Prepared Using Dipentaerythritol Hexaacrylate (Miramer M600) and Gelatin.....	57

3.2.1 Structural Evaluation of cHAP	57
3.2.2 Morphological Evaluation of Formed Acrylate-Gelatin-cHAP Composites	60
3.2.3 Computed Tomography Studies of cHAP-Acrylate Composites	63
3.2.4 Surface Hydrophilicity Evaluation of cHAP- Acrylate Composite.....	66
3.3 Porous Carbonated Hydroxyapatite (cHAP)-Poly(ethylene glycol) Diacrylate (PEGDA) Composite Prepared Using Foaming Agent Azodicarbonamide (ADCA).....	68
3.3.1 Purity of cHAP-PEGDA Evaluation Using Chromatorgraphy and DSC	68
3.3.2 Density and Morphology Evaluation of cHAP-PEGDA Composites .	71
3.3.3 Studies of Methylene Blue (Toluidine Blue) Dye Absorption on Low Crystallinity cHAP-PEGDA.....	72
4. CONCLUSIONS	73
5. LIST OF PUBLICATIONS.....	75
5.1 Articles in Journals	75
5.2 Attended Conferences	75
REFERENCES	77
ACKNOWLEDGEMENTS	94
SANTRAUKA	95
CURRICULUM VITAE	118
CONFERENCES	120
PUBLICATIONS	121

INTRODUCTION

Bone defects are among the main causes of reduced life quality due to trauma, diseases (e.g. cancer, osteoporosis-related fractures, congenital bone malformations), aging process, intense sport activity, obesity, or ions deficiency (e.g. leads to dysfunction and diseases in bone tissue, such as osteoporosis and osteomalacia). The natural process of bone repair is enough to regenerate in most of the bone fractures, although bone tissue can not handle with large size “critical” lesion.

Autografts, allografts and xenografts were the first used therapeutic approaches in bone tissue replacement and still a major choice for surgeons. Prior to select the ideal graft, i.e. autografts (i.e. bone transplantation from one part to another part of the same body), allografts (i.e. bone transplantation from donor of the same species) and xenografts (i.e. from other species), bone disabilities, bone defect sizes, tissue viability, biomechanical properties, graft handling and costs are studied.

Osteoinductivity and osteoconductivity are the main characteristics of allografts and xenografts, while autografts are defined as “gold standard” due to their osteoinductivity, osteoconductivity and osteogenic properties, relevant on bone healing, modelling and remodelling. Moreover, various drawbacks, such as risk of rejection, infection, diseases transmission, pain, bone graft loss/resorption, lack of vascularisation, reduced availability and high cost were identified; thus new strategies have been designed and investigated. Bone substitutes based on calcium phosphate, bioactive glasses, polymers and composites were the targets for investigation. The problems with bone grafts availability and donor site morbidity were supported, but still new achievements must be implemented, mainly on synthetic materials that closely mimic the structure and function of bone tissue and the production of scaffolds with suitable mechanical properties for regeneration of critical sized bone defects.

Intensive efforts on development of smart materials were performed, with the perspective to present customised and efficient solutions for the recovery of tissue functionality. In respect to bone tissue regeneration, the challenge is to achieve effective therapies that helps on completely function recovery from diseased tissues without second surgery intervention. On the other hand, smart biomaterials can be engineered as systems for delivery of therapeutic substances directly on the target site, thus avoiding systemic administration. Progress in this respect can guarantee standardized performances (e.g. contrary to autologous or heterologous bone), as well as reduced adverse

effects and improvement on osteoconductivity, osteoinductivity and osseointegration.

Tissue Engineering (TE) has been investigated as an innovative approach to develop biomimetic templates for regeneration of bone tissue defects. In mid-1980s, Langer and Vacanti defined TE as “an emerging and multidisciplinary scientific area that applies principles of engineering and life sciences towards the development of biological substitutes that repair, restore or enhance tissue and organs functions”, by combining cells, biomaterials and biomolecular signals (e.g. growth factors or bone morphogenic proteins) and osteogenicity, osteoconductivity and osteoinductivity properties of biomaterials are improved. On the other hand, suitable mechanical properties and appropriated degradation rate have been achieved on bone scaffold design, as well as easy-to-use in clinical practise.

The scope of my PhD thesis was to develop novel biomimetic hybrid biomaterials with potential of use in innovative smart and personalized applications in medicine, with particular respect to bone tissue engineering. The relevance of this activity is in the need of bioactive, bioresorbable and smart biomaterials, able to substantially activate, promote and sustain biologic processes yielding tissue regeneration. Nowadays this need is made extremely crucial by the steady ageing of the population and increase in the occurrence of bone diseases generating high disability and remarkable healthcare costs. Particularly, smart, stimuli- responsive biocompatible materials are highly desired, as they can enable more effective and personalized therapies in medicine.

The **main aim** of this doctoral thesis is fabrication of multifunctional inorganic (bioceramic)-organic(polymer) composites as a potential bone-tissue substitute material.

The tasks of the present thesis are formulated as follows:

1.To synthesise and characterize Na-Ca-Si-P-O glass-ceramic biomaterial and a single phase nanocrystalline carbonated hydroxyapatite (cHAP).

2.To prepare hybrid inorganic-organic composites consisting of Na-Ca-Si-P-O glass-ceramic and polymethyl methacrylate (PMMA), and characterise their dissolution and mechanical properties.

3.To prepare hybrid inorganic-organic composites consisting of cHAP, acrylate and gelatin, and investigate their hydrophilicity properties.

4.To prepare porous hybrid inorganic-organic composites consisting of cHAP and poly(ethylene glycol) diacrylate PEGDA using blowing agent foaming agent azodicarbonamide (ADCA) and investigate their liquid sorption properties.

LIST OF SYMBOLS AND ABBREVIATIONS

2D – two-dimensional
3D – three-dimensional
ALP – alkaline phosphatase
cHAP – carbonated hydroxyapatite
DSC – differential scanning calorimetry
DTG – derivative thermogravimetry
GC – glass ceramic
HAP - hydroxyapatite
PCL – poly(ϵ -caprolactone)
PEG – poly(ethylene glycol)
PELA – poly(D,L-lactic acid-co-ethylene glycol-co-D,L-lactic acid)
PGA – poly(glycolic acid)
PLA – poly(lactic acid)
PLGA – poly(lactic-co-glycolic acid)
Rf – strain fixing ratio
Rr – strain recovery ratio
SEM – scanning electron microscopy
SMP – shape memory polymer
TG - thermogravimetry
Tg – glass transition temperature
TGA – thermogravimetric analysis
Tm – melting temperature
UV – ultraviolet
 μ -CT – micro-computed tomography

1. LITERATURE REVIEW

In this part we provide an overview of the biomaterials, i.e. inorganic (calcium phosphates), organic (polymers) and hybrid, combined of calcium phosphates and polymers materials, used for bone-tissue engineering applications. We review the synthesis and processing methods, and emphasize the importance of precursors and synthesis parameters to achieve multifunctionality of the hybrid composite materials.

1.1 Bone

Bone, a structural component of body, is a ceramic (carbonated hydroxyapatite)-polymer(collagen) composite. The chemical constituencies of the skeletal system are protein (mainly type-I collagen), a mineral phase (carbonated hydroxyapatite, cHAP), and water - which are assembled into a complex and hierarchical structure. There are two types of bone (Figure 1): cortical (or compact) and cancellous (or trabecular, or porous) [1, 2].

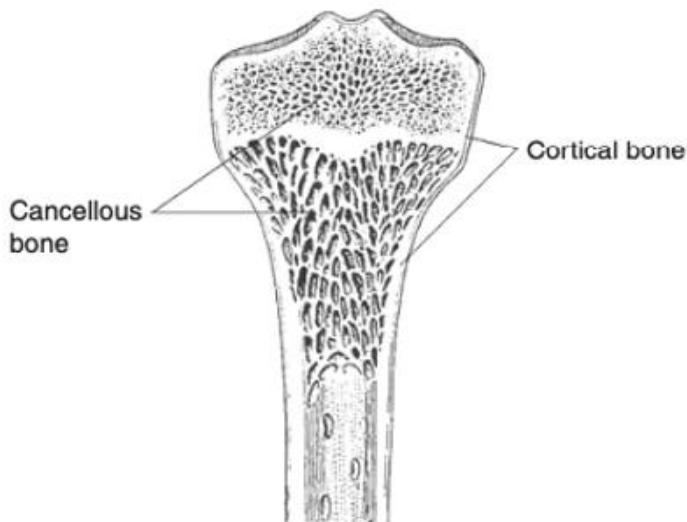


Figure 1. Longitudinal section of femur [1].

Although stoichiometric HAP never occurs in biological systems, it has been extensively used as a bone graft substitute or as a coating for orthopaedic devices (e.g. hip-joint prosthesis) and dental implants due to its chemical and structural similarity with natural bone mineral. Comparison of chemical

composition of human enamel and bone and pure HAP ceramic is shown in Table 1.

Table 1 Structural and chemical comparison of human enamel, bone, and pure HAP ceramic [2].

Constituents (wt%)	Enamel	Bone	HAP (stoichiometric)
Calcium	36.0	34.8	39.6
Phosphorus	17.7	15.1	18.5
Sodium	0.5	0.7	-
Potassium	0.08	0.03	-
Magnesium	0.44	0.55	-
Carbonate	3.2	5.8	-
Fluoride	0.01	0.02	-
Chloride	0.3	0.10	-
Ash (total inorganic)	97%	65%	100%
Ca/P molar ratio	1.62	1.71	1.67

The elastic modulus of cortical bone varies from 7 to 24 GPa. This is much lower than that of single-crystal hydroxyapatite (HAP), which has a Young's modulus of approximately 130 GPa and a strength of 100 MPa. Collagen is not linearly elastic, but tangent modulus is in the range of 1-1.5 GPa. The tensile strength of bone is dependent on the size of flaws and varies significantly, ranging from 20 MPa to 270 MPa [1]. Collagen has a relatively high tensile strength, on the order of 50 MPa. The strength of bone is optimized by nano-scale HAP crystals, and the bone nanocrystals have dimensions of 4 nm × 40 nm. The limiting value of bone crystal dimension for which the strength is no longer size dependent has been calculated to be 30 nm. Furthermore, both the strength of bone and its toughness are dependent on the degree of mineralization.

The porosity of cancellous bone is typically in the range 75-95% and the apparent density of cancel (mass per unit volume of solid trabeculae) of cancellous bone ranges from 0.2 to 0.8 g/cm³. The porosity reduces the strength of the bone, but also reduces its weight. The mechanical strength is determined by the porosity and the manner in which this porosity is structured, since the struts can align such that the strength is optimized in the directions in which the stresses are highest. The pores also perform other physiological functions and contain the marrow. The porosity of compact bone is typically 5-10% [1].

Cross-sectioned images extracted from cone beam computed tomography (CBCT) data, presented in Figure 2, show the maxillofacial regions of Patient X and common defects, i.e. absent teeth and bone. The material used as a bone scaffold must satisfy a number of requirements, including biocompatibility, biodegradation with negligible toxicity, appropriate porosity, and mechanical properties, and the ability to integrate with biological molecules or cells to regenerate tissue [3-8]. The complexity and multifunctionality of natural bone material imply that multidimensional approach to design new bioceramic materials is, therefore, important.

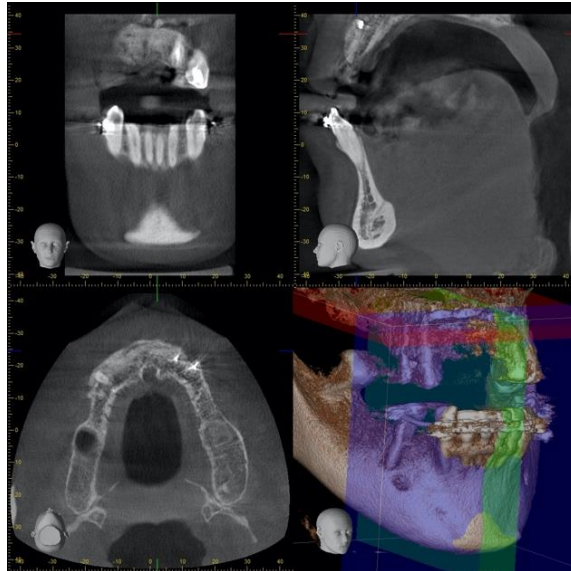


Figure 2. Cone beam computed tomography (CBCT) images of the maxillofacial bones of patient X showing various origins of bone defects (images are courtesy of RG Clinic, Vilnius, Lithuania).

1.2 Inorganic Biomaterials

The science of biomaterials developed over the last 60 years with the increasing limitations in the quantity of allografts, the morbidity resulting from during implantations, and the discovery of new materials that can be used as medical implants [9]. There were several attempts to define the word “biomaterial” over the years, but the first real definition came in 1987 by David F. Williams who stated: “A biomaterial is a nonviable material used in a medical device, intended to interact with biological systems.” Then, in 1999, he modified this definition of biomaterials to become: “A material intended to interface with biological systems to evaluate, treat, augment or replace any tissue, organ or function of the body.” Another significant definition of

biomaterials was made in 2003 by Miller-Keane and O'Toole who said that a biomaterial represents: "Any substance (other than a drug), synthetic or natural, that can be used as a system or part of a system that treats, augments, or replaces any tissue, organ, or function of the body; especially, material suitable for use in prostheses that will be in contact with living tissue" [10].

It has long been accepted that any foreign material, except for autografts (bones obtained from another anatomic site in the same subject), placed within a living body will not be completely compatible and will initiate reactions called host-tissue responses. These reactions occur at the biomaterial/tissue interface and result in time-dependent changes in the surface characteristics of both the implant and the surrounding tissue. Biomaterials can be classified as nearly bioinert and those that are bioactive (and biodegradable) materials [11]. A bioinert material has minimal interaction with the surrounding tissue once implanted in human body. Examples include stainless steel, titanium, alumina (aluminum oxide) and /or zirconia (zirconium oxide)-based biomaterials, and ultra-high molecular weight polyethylene (UHMWPE). Generally, the body interacts with bioinert material by producing a thin fibrous capsule around the implant to separate it from the host tissue, thus its biofunctionality relies on tissue integration through the implant. On the other hand, when a bone bioactive material implanted inside the body, it promotes the creation of a surface layer of biological apatite before interfacing directly with the tissue at the atomic level, leading to formation of direct chemical bonds to the bone tissue. Examples of bone bioactive materials are calcium phosphates (CaPs), bioactive glasses and glass-ceramics (composites, consisting of crystalline phase and a residual glassy phase).

The term "bioceramics" is applied to the ceramics used for the repair and reconstruction of diseased or damaged parts of the musculoskeletal system. Bioceramics are inorganic biomaterials that include crystalline ceramics, amorphous glasses, and glass-ceramics [11]. Bioceramics, either dense or porous, have been widely used in medical applications such as dental implants, coatings for orthopaedic and maxillofacial prosthetics, bone fillings, bone scaffolds and for alveolar ridge augmentation. Generally, they are hard, stiff and very biocompatible materials, but they are also brittle and weak in tension.

Over the last few decades, researchers tried to incorporate calcium phosphate based bioceramics to produce implants for clinical application. Synthetic bone graft substitutes comprise a spectrum of inorganic CaPs-based materials. CaPs present generally high biocompatibility because they are naturally present in the body both dissolved and in solid state. Different CaPs that are used for bone replacements are summarised in Table 2.

Table 2 Summary of calcium phosphate compounds with their corresponding Ca/P molar ratios, abbreviations and formulas [12-15]

Compounds	Typical abbreviations	Ca/P molar ratio	Solubility at 25 °C, -log Ks	Chemical formula
Monocalcium phosphate monohydrate	MCPM	0.5	1.14	Ca(H ₂ PO ₄) ₂ ·H ₂ O
Monocalcium phosphate anhydrous	MCPA or MCP	0.5	1.14	Ca(H ₂ PO ₄) ₂
Dicalcium phosphate dihydrate (brushite)	DCPD	1.0	6.59	CaHPO ₄ ·2H ₂ O
Dicalcium phosphate (montite)	DCPA or DCP	1.0	6.90	CaHPO ₄
Octacalcium phosphate	OCP	1.33	96.6	Ca ₈ (HPO ₄) ₂ (PO ₄) ₄ ·5H ₂ O
α-Tricalcium phosphate	α-TCP	1.5	25.5	α-Ca ₃ (PO ₄) ₂
β-Tricalcium phosphate	β-TCP	1.5	28.9	β-Ca ₃ (PO ₄) ₂
Calcium-deficient hydroxyapatite	CDHA or Ca-def HA	1.5– 1.67	~85	Ca _{10-x} (HPO ₄) _x (PO ₄) _{6-x} (OH) _{2-x} (0 < x < 1)
Hydroxyapatite	HA, HAp or OHAp	1.67	116.8	Ca ₁₀ (PO ₄) ₆ (OH) ₂
Fluorapatite	FA or FAp	1.67	120.0	Ca ₁₀ (PO ₄) ₆ F ₂
Oxyapatite	OA, OAp or OXA	1.67	~69	Ca ₁₀ (PO ₄) ₆ O
Tetracalcium phosphate, mineral hilgenstockite	TTCP or TetCP	2.0	38–44	Ca ₄ (PO ₄) ₂ O

The stoichiometric HAP (Ca/P ratio of 1.67) has the chemical formula Ca₅(PO₄)₃(OH) that is frequently written as Ca₁₀(PO₄)₆(OH)₂ to indicate that the hexagonal unit cell is composed of two molecules [16, 17]. The inorganic component of biological hydroxyapatite (Ca₁₀(PO₄)₆(OH)₂, HAP) contains a variety of trace ions in the crystal lattice, which have a relationship with the biological properties of HAP such as solubility and biocompatibility. As cHAP they form the mineral component of natural bones, teeth and tendons, and when the concentration of carbonate ions in the HAP lattice is in the range of 3-8 wt%. The biological forms of these materials are usually nanocrystals that are precipitated under physiological conditions. They dissolve into their ionic components Ca²⁺ and PO₄³⁻, which are naturally present in the body in concentrations ranging from 1 to 5 mM [1]. Carbonate ions can substitute a hydroxide (OH⁻) or phosphate (PO₄³⁻) group, leading to A- or B-type carbonated apatites, respectively [18]. The chemical formula for A-type carbonated apatites has been defined as Ca₁₀(PO₄)₆(OH)_{2-2y}(CO₃)_y, where 0 ≤ y ≤ 1, while for the B-type Ca_{10-x}(PO₄)_{6-x}(CO₃)(OH)_{2-x}, where 0 ≤ x ≤ 2 and sodium ions are located in the calcium sites, inducing a favourable electrical charge balance. In biological apatites carbonate ions replace the PO₄³⁻ group and OH⁻ group, and so can be considered as AB-carbonate substituted apatites with the chemical formula of Ca_{10-x}(PO₄)_{6-x}(CO₃)_x(OH)_{2-x-2y}(CO₃)_y [14, 19-21]. The crystal lattice of cHAP and substitution sites are presented in Figure 3 [22].

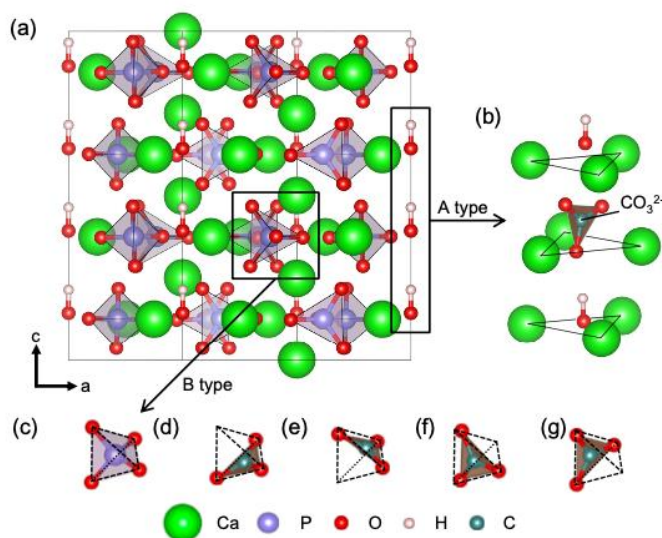


Figure 3. HAP crystal lattice showing A-, B-substitution [22].

The other frequently investigated synthetic CaPs are calcium-deficient hydroxyapatite (CDHA, $\text{Ca}_{10-x}(\text{HPO}_4)_x(\text{PO}_4)_{6-x}(\text{OH})_{2-x}$, where $0 < x < 1$), tricalcium phosphate (TCP, $\text{Ca}_3(\text{PO}_4)_2$) and biphasic calcium phosphate (BCP) – mixture of HAP and TCP [23-25]. The advantages and disadvantages of these bioceramics with high or low resorption or dissolution rates have been broadly discussed, these are also briefly reviewed in a following chapter.

TCP is a biodegradable bioceramic which has a Ca/P ratio of 1.5, and exists in three different polymorphs: β -TCP stable at low-temperature ($< \sim 1125^\circ\text{C}$), α -TCP occurring at high-temperature ($\sim 1125\text{--}1430^\circ\text{C}$) and α' -TCP stable at even higher temperature ($> \sim 1430^\circ\text{C}$). The latter is not of practical interest since it only exists at high temperatures and reverts almost instantaneously to α -TCP upon cooling below the transition temperature. In contrast, both α - and β -TCP have been widely used in several clinical applications in dentistry, maxillo-facial surgery and orthopaedics due to their stability at low temperatures. β -TCP is stable at room temperature but transforms at $\sim 1125^\circ\text{C}$ to α -TCP, which can be retained during cooling to room temperature [26-28]. Furthermore, some of these CaPs are able under certain conditions to transform from one to another [29]. For example, α -TCP is much more reactive than β -TCP in aqueous solutions and can easily be hydrolysed with the formation of CDHA, which is similar to HAP and resembles cHAP, the mineral component of natural bones and teeth [30].

Another bioceramic that received more attention in bone research is whitlockite (or magnesium whitlockite) having a molecular formula of

$\text{Ca}_{18}\text{Mg}_2(\text{HPO}_4)_2(\text{PO}_4)_{12}$. It is a calcium orthophosphate in which, in biological conditions, magnesium is partly substituted for calcium [31, 32]. It occurs in physiological or pathological conditions at extra or intratissular sites, mainly in tissues of non-epithelial origin [33]. Whereas the formation of both apatite and magnesium whitlockite appears to be caused by the binding of their constituting ions with proteolipids, magnesium inhibits apatite originating from amorphous calcium phosphate to the benefit of whitlockite formation.

Calcium sulfate (CaSO_4) as a bone substitute was reported in 1892. This material also is called “gypsum” or “plaster of Paris” and offers many advantages as it presents a structure similar to bone, it is osteoconductive, inexpensive, available in different forms (hard pellets and injectable fluids) and does not generate allergic reactions [34]. Furthermore, CaSO_4 resorbs rapidly (in 1-3 months) which creates porosity while stimulating bony ingrowth. As resorption of CaSO_4 is faster than the rate of new bone deposition, it is rather unsuitable as a material to support early functional rehabilitation. Other drawbacks are that it is neither osteoinductive nor osteogenic.

The first evidence of direct bone bonding to a silicate-based glass implant was observed by Hench et al. in 1970s. Bioactive glass is an amorphous material that has a random arrangement of atoms due to the rapid cooling of the molten ceramic. The composition of original bioglass, designated as 45S5 Bioglass, is 45% silica (SiO_2), 24.5% calcium oxide (CaO), 24.5% sodium oxide (Na_2O), and 6% phosphorous pentoxide (P_2O_5) in weight percentage. The main constituents of most bioactive glasses are SiO_2 , Na_2O , CaO and P_2O_5 . 45S5 Bioglass has shown both osteoconductive (able to support bone formation in osseous defect sites) and osteoinductive (stimulates bone growth by osteoprogenitor cell recruitment and activation) properties as it promotes new bone growth along the bone–implant interface as well as within the implant away from the bone–implant interface [5, 35, 36]. The specific composition of the bioactive glass determines its bioactivity, osteoconductivity and biodegradability.

The variety of relevant bioactive glasses (amorphous, Ca- and possibly P-containing silica based materials) and glass-ceramics had been proved to have bone-bonding capability [14, 37-39]. For instance, Hench et al. noticed that for their particular formulation of bioactive glass (45S5 Bioglass), rapid bonding to bone occurred when the silica level was in the range 42–53%, whereas glasses with 54 to 60% of silica required 2–4 weeks for bonding, and with glasses containing more than 60% of silica, there was no direct bonding between the bioactive glasses and bone [21]. A variety of bioactive glasses developed over the years, including silicate-based, phosphate-based and

borate-based ones, have been used in bone scaffolds, middle ear replacements and tooth root replacement. However, many of these materials have relatively limited use in load-bearing applications due to their amorphous structure which decreases their mechanical strength and lowers their fracture toughness. Bioactive glasses bond to living bone tissue through a sequence of reactions on the material surface followed by cellular reactions. Briefly, ion leaching/exchange occurs at the surface of the implant which leads to dissolution of the glass network and precipitation and growth of a calcium deficient carbonated apatite surface. These reactions results in biochemical adsorption of growth factors, the presence of osteogenic precursors then favors the formation of osteoblasts, and the sequences of cellular events lead to rapid new bone formation [14, 38, 39]. To overcome the limitations (i.e. high dissolution rates) of the bioactive glasses, glass-ceramic materials have been developed.

Glass-ceramics are crystallised glasses, consisting of a composite of a crystalline phase (crystal sizes ranging from 0.1 to 10 μm) and a residual glassy phase. The production process of glass-ceramics involves the heat treatment of a base glass to induce controlled crystallisation and to convert it into a glass-crystal mixture. The heat treatment promotes the nucleation and growth of various kinds of crystalline phases with fine grain sizes. Thus the crystallisation and formation of the crystal phases can be modulated to achieve a combination of special properties, such as bioactivity, machinability and improved mechanical properties. For example, apatite-wollastonite (A-W) glass-ceramic was first introduced by Kokubo and his colleagues in 1982 and became one of the most extensively studied glass ceramics for use as a bone substitute. A-W glass-ceramic is composed of glassy matrix [MgO-CaO-SiO_2] reinforced by crystalline apatite [$\text{Ca}_{10}(\text{PO}_4)_6(\text{O},\text{F}_2)$] and wollastonite [$\text{CaO}\cdot\text{SiO}_2$]. Thus, it exhibits not only bioactivity, but also fairly high mechanical strength. Also, its bending strength, fracture toughness and Young's modulus are the highest among bioactive glasses and glass-ceramics, enabling it to be used in some compression load bearing applications such as vertebral prostheses and iliac crest replacement [14, 21, 40, 41]. Concisely, bioactive ceramics, i.e. calcium phosphates, bioactive glasses, and glass-ceramics, are capable of promoting the formation of bone-like hydroxyapatite layers at their surface and of creating an interface which contributes to the functional longevity of the tissue.

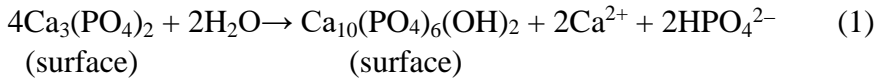
1.2.1 Physico-Chemical Properties of Calcium Phosphates and Glass-Ceramic Materials

There are a number of important factors for a material in order to be used in human body, such as appropriate mechanical properties, biocompatibility, which was also defined by Williams in 1987 as: “ the ability of a material to perform with an appropriate host response in a specific application” [42], and biodegradability which means that the material should degrade in the body due to enzymatic or body fluids reactions or be resorbed harmlessly over time by cellular actions [43].

Based on the tissue response to bioceramic, biomaterials can be classified as biologically inactive (nearly inert, or bioinert), biologically active (bioactive), resorbable and toxic [11, 14, 44]. Bioinert ceramics possess a high chemical stability in vivo as well as high mechanical strength. When they implanted in living bone, they incorporated into the bone tissue in accordance with the pattern of "contact osteogenesis", thus the new tissue is formed on the implant surface, surrounded by non-adhesive connective tissue capsule, without chemically interacting with the implant [45]. They are also hard to break, and have good resistance to corrosion. Zirconia is commonly used in the femoral heads of total hip joints because of its high fracture toughness, while alumina is used for dental implants and in hip prostheses for its good biocompatibility, strength and high wear and corrosion resistance. Finally, pyrolytic carbon is known for its good durability and biocompatibility, but its brittleness and low tensile strength limit its usage in high loads medical applications [46]. These type of ceramics are out of scope and therefore are just briefly mentioned herein. Biodegradable materials offer advantages in temporary biomedical applications and tissue engineering because of their natural clearance from the body, which will enable the ingrowth of the surrounding tissue over time to restore its normal function after having benefited from the implant [47]. In addition, biodegradable implants can sometimes prevent or reduce long-term safety problems, such as implant-tissue interface, long-term immune rejection, as well as failure of the device [48].

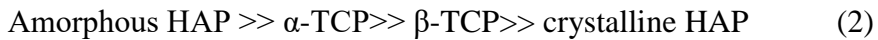
Two major calcium phosphates that have been used extensively for synthetic bone scaffolds are TCP and HAP. However, the mechanism of osteoinductivity remains unknown. It has been studied in relation with physicochemical parameters of the bioceramic such as composition, microporosity, the specific surface area, in addition to the surface topography, geometry, and charge [12, 37, 49, 50]. It is believed that the bioactivity of CaPs and new bone deposition on their surface is directly linked to their partial

dissolution and the release of their ionic products in vivo. The partial dissolution of CaPs results in an increase in the local concentration of calcium and phosphate ions, thus increasing the degree of saturation in their microenvironment, leading to the precipitation of biological apatite microcrystals on the surface of the implant which link between the host tissue and the bioceramic. Consequently, the apatite microcrystals incorporate other ions such carbonate and magnesium in addition to organic macromolecules from biological fluids. The precipitated apatite may also incorporate various proteins and growth factors exist in the microenvironment, which subsequently can promote cell attachment and function [12, 17]. However, the dissolution rate of CaPs is mainly associated with their chemical composition. In general, the Ca/P ratio of CaPs is considered as an indicator for the stability of the ceramic in the body, thus compounds with a Ca/P ratio of less than one are not favourable for biological implantation due to their high solubility. The dissolution rate of CaPs is also influenced several other parameter such as basicity/acidity and solubility of CaPs, the porosity in the calcium phosphate (CaP) material and its particle size, local acidity, fluid convection and the temperature and pH of media. Porosity of CaPs does not only affect the resorbability of the bioceramic, but it is also important to its mechanical properties and the ingrowth of bone. Porous CaP permits cell colonisation and vascularisation. Therefore, calcium phosphates with macro- ($>100\ \mu\text{m}$), micro- ($<10\ \mu\text{m}$) and nano- ($<100\ \text{nm}$) porosities have been developed to improve cell adhesion, proliferation and differentiation. In addition, studies have demonstrated that increasing the specific surface area and pore volume of CaPs can greatly accelerate the kinetic process of biological apatite deposition and therefore enhance the bone formation. In vivo biodegradation CaPs can also occur due to active resorption, mediated by cellular activity of macrophages and osteoclasts or by phagocytosis, which also known as “cell-eating”. Furthermore, despite having the same chemical composition, α -TCP and β -TCP differ in their solubility. α -TCP shows higher solubility (2.5 mg/L) than β -TCP (0.5 mg/L) at 25 °C due to its crystal structure and higher specific energy, therefore it is considered unsuitable for surgical implants and usually employed as component for bone cements [17, 28]. Both α - and β -TCP are not found in biological systems, Mg-stabilised β -TCP (whitlockite) has been detected during pathological calcification, such as dental calculus formation and in renal stones, as well as in arthritic cartilage. However, pure β -TCP has not been observed in enamel, dentin, or bone [17]. When implanted in living tissue, TCP interacts with body fluids and creates HAP on exposed surfaces in accordance with equation 1 [51]):



Mineralization of CaPs in bone has been proposed to proceed via an initial amorphous precursor phase which later transforms into nanocrystalline phase. For example, Karashima et al. demonstrated low-crystallinity HAP preparation, and its composition induces excellent tissue response and good osteoconductivity, because interconnected pores within low-crystallinity HAP foam provide the space for cell growth and tissue penetration [52]. Studies also showed that the crystallite size, especially when it is at the nanoscale, affects the dissolution of soluble minerals [53]. Dissolution mechanism of calcium apatites in acids appear to be of the paramount importance for our species. Literature reported several dissolution models as well as the importance of factors associated with solution (pH, composition, saturation and hydrodynamics), bulk solid (chemical composition, solubility, particle size) and surface (defects, adsorbed ions, “history”, phase transformation) on the apatite crystals [54, 55] – these studies made a significant impact on understanding of the medical aspects of dental caries and osteoporosis. The dissolution of materials can be altered by fabricating composites. For example, Belluci et al. fabricated HAP/bioglass composites and demonstrated different in vitro bioactivity as well as stability of composites after submersion in simulated body fluids (SBF) [56].

The dissolution rate of HAP in vitro depends on the type and concentration of buffered or unbuffered media, pH of the solution, the crystallinity of HAP and the amount of non-HAP phases, the degree of micro- and macroporosity, and solid/solution ratio. The degree of dissolution decreases in the following order [20, 57]:



Similar to other calcium phosphates, the formation of apatite microcrystals on HAP-based implants is believed to be a dissolution-precipitation process. However, the partial dissolution of HAP arises from the cellular activity, causing the release of Ca^{2+} , HPO_4^{2-} , and PO_4^{3-} and increase the supersaturation of the microenvironment, and subsequently results in apatite formation [20].

Surface structure is important factor affecting the apatitic phase response where scaffolds and body fluids interact. It was demonstrated improvement of osteoblastic function on nanophase ceramics [58]. Surface modification is another way to alter surface properties. It has been shown that surface

hydrophilicity decreases in a significant extend in relation to the presence of citrates, and this was attributed to the presence of $-\text{CH}_2$ functional groups after the surface modification [59].

The incorporation of foreign ions in the CaP matrix has been shown has beneficial effect on the scaffold integration within bone matrix [60, 61]. For example, it is reported that magnesium ions (Mg^{2+}) readily enhance bone regeneration by promoting the proliferation and differentiation of osteogenic (stem) cells via osteogenesis signalling pathways in vitro [62, 63]. Magnesium (Mg), the fourth most abundant intracellular element in the body, has a stimulating effect on new bone formation. The depletion of Mg results in bone resorption, loss of bone structure and eventually osteoporosis [64]. An attempt to model the mechanical properties of bone-substitute materials has been made. Mechanical properties were enhanced of composites CaP and glass-ceramics [65]. Dopping wollastonite with Mg ions leads to improved mechanical and dissolution properties of bioceramic [66]. Bioceramic material can be rationally tuned in phase (α -TCP or β -TCP), mechanical strength (in compression and bending modes), and fracture toughness ($> 43.2 \text{ MPa m}^{1/2}$) through the use of Mg doping at a precisely defined dilute content. Xie et al. have also showed enhanced mechanical response from magnesium-doped porous wollatonite scaffolds compere to pure CSi and β -TCP porous ceramics [67]. Thus, based on the variability of material physicochemical properties, in this work, we place emphasis on the bioinert ceramic hydroxyapatite and bioactive glass-based material, their mechanical and dissolution properties, as well as their synergism with organic materials.

1.2.2 Synthesis Methods of Inorganic Biomaterials

CaP and glass-ceramic materials are available in different forms. Depending on the application, they can be produced in the form of powders, granules, foams, cements, pastes, scaffolds or coatings [12-14, 68-70]. Powders and granules are the most frequently used materials due to their broad availability, relatively low cost, and good biological properties. In this part we review the synthesis of bioceramics with an emphasis on the nanocrystalline powdered (or bulk) cHAP and low-crystallinity glass ceramics.

HAP is the most stable and least soluble calcium phosphate phase in aqueous solutions at pH value higher than 4.2 [71]. As mentioned previously, stoichiometric HAP never occurs in biological systems, but it has been extensively used as a bone graft substitute due to its chemical and structural similarity with natural bone mineral. The crystal structure of HAP can accommodate a variety of cationic and anionic substitutions by various other

ions for the Ca^{2+} , PO_4^{3-} and OH^- groups. These ionic substitutions can have a significant effect on the lattice parameters (i.e. physical dimension of unit cell), crystal morphology, crystallinity, solubility and thermal stability of HAP. It can also affect the osteoclastic and osteoblastic response in vitro and degradation and bone regeneration in vivo [21, 72, 73].

CaPs can be synthesised using different techniques such as dry methods (solid-state reactions), wet methods (precipitation, hydrolysis, sol-gel, emulsion and hydrothermal synthesis) with frequently followed subsequent annealing (combustion), and alternate energy input methods (microwave (MW)-assisted, ball-milling and sonochemical methods) [70]. Depending on the preparation technique, CaPs with various morphology (blades, needles, rods, or equiaxed particles), particle size (micro or nanoscale), stoichiometry and level of crystallinity can be obtained. Among those techniques, the precipitation method is the most straightforward and commonly used, and it comprises a reacting source of PO_4^{3-} ligand with a source of calcium in the presence of other additives such as base or acid. For example, Merry et. al have reported the synthesis of cHAP at 20 °C and $\text{pH} \geq 11$ by precipitation method and subsequent annealing at temperatures up to 1100 °C [74]. Results showed that mechanical properties are influenced by carbonate content and mode of the substitution. In another study, nanocrystalline and nanometric (15-20 nm by 3-5 nm) cHAP was obtained by precipitation method (synthesis temperature of 37 °C). Subsequent aging or freeze-drying led to the homogenous with a very high specific surface area (300 m^2/g) powders. An amorphous CaP powders were also produced by sol-gel method; following calcination at 500-1300 °C powders crystallized to a HAP phase [75]. One shall note that post-treatment (calcination) may lead to aggregation of particles and formation of larger sintered grains. Therefore, the post-treatment parameters (temperature, time) have to be considered carefully. To produce CaPs with desirable particle sizes, shape and surface area the polymers or surfactant-mediated approach can be used. For example, Alinauskas *et al.* produced cHAP using three different polymeric matrices, i.e. PEG, PVA and mixture of TEA with PEG [76]. It was shown that using PEG the phase pure and having smallest nanocrystallite sizes cHAP was obtained. Uota et al. used nonaoxyethylene dodecyl ether (C_{12}EO_9) and polyoxyethylene (20) sorbitan monostearate (Tween 60) to produce differently-shaped HAP crystals [77]. Solid state reactions are also widely used for HAP synthesis and usually yield a stoichiometric and well-crystallised product. However they require relatively high temperatures and long heat-treatment times [20, 78, 79].

The stoichiometry of HAP ($\text{Ca/P}=1.67$) is highly important where thermal processing of the material is needed. A slight decrease in the stoichiometric ratio of calcium and phosphorus in HAP can cause the formation of either α - or β -tricalcium phosphate upon sintering. Existence of TCP phases was shown to improve the mechanical behaviour of HAP and increase its biodegradability. In contrast, if the Ca/P ratio of the HAP exceeds the value of 1.67, CaO forms during sintering. The presence of CaO is reported to decrease strength of the material and may even lead to decohesion of the whole material because of the build-up of stresses arising from formation of Ca(OH)_2 which eventually transforms into CaCO_3 , and related volume changes [17, 79-81]. As discussed earlier, CaPs are generally brittle and have low tensile strength, thus they provide limited biomechanical support. While TCPs are less brittle compared with HAP, their faster degradation rate results in quicker loss of mechanical strength over time [37].

HAP can also be extracted from natural resources such as fish bones, seashells, eggshells, bovine bones and shrimp shells. It can be produced in dense or macroporous form [15]. Dense HAP possesses a porosity of less than 5% and can also be described as microporous. The powder is compressed into a mold at a pressure of 60-80 MPa, with or without a binder (e.g. 1 wt% cornstarch and water, stearic acid in alcohol, or hydrocarbons of low molecular weight). Then, the compressed material can be sintered at the high temperature, usually 950-1300 °C, at fixed heating rate (~100 °C per hour) and held at this temperature for several hours before cooling at the same rate as the heating rate. Another method for producing dense HAP is the hot pressing technique where heat and pressure are applied at the same time in a continuous manner, which allows the densification of HAP to occur at a much lower temperature than in conventional sintering, thus producing HAP with higher purity and lower grain size. Dense HAP materials are usually used in unloaded tooth root substitutes due to their poor mechanical properties. On the other hand, porous HAP has been widely applied as bone substitute due to its strong bonding to the bone. In addition, the pores provide a mechanical interlock which results in a firmer fixation of the material. Porous HAP with pores <10 μm in diameter is required for circulation of body fluids and those >100 μm are required for colonisation of target cells. However, such large pores decrease strength of the implant significantly. Therefore, porous HAP implants cannot be heavily loaded and are used to fill only small bone defects. Other applications of porous HAP include drug delivery systems, alveolar ridge augmentation and orthognatic reconstruction [15, 20, 82].

With regard to the glass-ceramics sol-gel synthesis method is the most popular. Sol-gel derived bioactive glass has advantages over the dense

bioactive glass produced by conventional solid melt method, because it possess nanoporosity and larger surface area that courses more rapid dissolution rate and subsequently enhances faster new bone formation [83]. However, one of the biggest challenges for utilization of bioactive glasses is its brittleness [36, 84].

1.2.3 Mechanical Properties of Biomaterials

Biomaterials that are currently available to manufacture orthopaedic and dental implants can be divided into metals and alloys, ceramics, polymers and composites. Mechanical properties are one the most important properties when considering processing bioceramics. CaPs are brittle in nature, which is attributed to their primary ionic bonds, and have low impact resistance. However, their compressive strength is fairly good, being higher than that of normal bone. Due to their high brittleness, they have been used either as non-load-bearing implants such as middle ear surgery, filling of bone defects in the oral cavity and skeleton, or as coatings on dental and orthopaedic metallic implants. The mechanical properties of calcium phosphate ceramics are strongly dependent on their chemical composition, crystallinity, grain size/shape and porosity. Generally, their mechanical properties decrease with increasing amorphous phase, microporosity and grain size, while compounds with high crystallinity, low porosity and small grain size exhibit higher stiffness, compressive and tensile strength as well as higher fracture toughness [12, 17, 37, 38, 41, 85].

Sol-gel derived bioactive glass has advantages over the dense bioactive glass produced by conventional solid melt method, because it possess nanoporosity and larger surface area that courses more rapid dissolution rate and subsequently enhance faster new bone formation [83]. However, one of the biggest challenges for utilization of bioactive glasses is its brittleness [36, 84]. The mechanical properties of the common ceramic biomaterials (from [46, 86]) are listed in Table 3.

Table 3. Mechanical properties of bioceramics.

Material	Young's modulus (GPa)	Compressive strength (MPa)	Tensile strength (MPa)
Alumina	380	4500	350
Zirconia	150-200	2000	200-500
Pyrolytic carbon	18-28	517	280-560
Bioglass-ceramics	22	500	56-83
Calcium phosphates	40-117	510-896	69-193

The mechanical properties of HAP depends mainly on the structure (dense or porous), particle size, sintering condition and the presence of non-HAP

phases. Table 4 summarises the mechanical properties of HAP ceramic [17, 79].

Table 4. Mechanical properties of HAP bioceramics.

Property	Value	Comments
Tensile strength	38–300 Mpa/~3 MPa	Dense HA/Porous HA
Compressive strength	120–900 Mpa/2–100 MPa	Dense HA/Porous HA
Bending strength	38–250 Mpa/2–11 MPa	Dense HA/Porous HA
Young’s modulus	35–120 GPa	Dense HA
Fracture toughness	0.7–1.2 MPa√m	Decreases almost linearly with porosity
Vickers hardness	3–7 GPa	Dense HA
Poisson’s ratio	0.27	Synthetic HA (bones ~0.3)

Metals and alloys have been extensively used for load bearing applications such as total joint prostheses (artificial joints) for hips, knees, shoulders and ankles, as well as using them in fracture fixation as plates, pins, and screws. Metallic implants have also been used in maxillofacial surgery, cardiovascular surgery and as dental materials. Metals have strong inter atomic bonds which gives them good tensile strength and fatigue resistance in addition to high ductility, thus they deform under high loads without breaking. However, their corrosion resistance under largely variable physiological and mechanical properties of living tissues might be an issue. With the exception of commercially pure titanium, alloys are more frequently used than pure metals due to their enhanced material properties such as strength and corrosion resistance. Typical examples of metallic orthopaedic materials are: titanium and titanium alloys, 316 and 316L stainless steel, and cobalt-chromium alloys [9, 46]. Table 5 lists the mechanical properties of some of metallic biomaterials compared to human cortical bone.

Table 5. Mechanical properties of metallic implants [46, 87].

Material	Modulus of elasticity (GPa)	Yield strength (MPa)	Tensile strength (MPa)
Cortical bone	15-30	30-70	70–150
Stainless steel	190	221–1213	586–1351
Co-Cr alloy	210-253	448–1606	655-1896
Titanium (Ti)	110	485	760
Ti alloy	116	896–1034	965-1103

1.3 Biocompatible Polymers

Both natural and synthetic polymers have been used as tissue engineering scaffolds. Natural polymers such as collagen, gelatin (denatured collagen) and fibrin are part of the natural extracellular matrix (ECM) or secreted during the

wound healing process. While natural materials such as collagen and fibrin are in clinical use, their batch-to-batch variability in isolation/purification, weak mechanical properties, poorly controlled degradation, cost, processing difficulties, and immunogenicity present challenges [88]. Synthetic polymers, if properly designed, can be fabricated reproducibly in large scales, exhibit improved mechanical properties and predictable degradation behaviors, and are amenable to a variety of chemical functionalization or physical modifications to introduce bioactivity. Chemical structures of commonly used synthetic polymers in tissue engineering is shown in Figure 4.

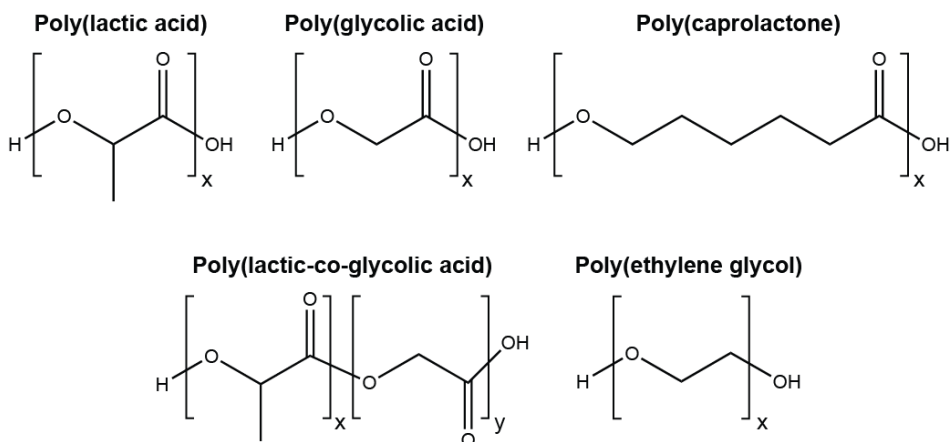


Figure 4. Commonly used synthetic polymers in tissue engineering.

1.3.1 Physico-Chemical Properties of Biocompatible Polymers

Biocompatible polymers with biodegradable properties the most widely used in tissue engineering are the hydrophobic polyesters poly(lactic acid) (PLA), poly(glycolic acid) (PGA), poly(lactic-co-glycolic acid) (PLGA), or poly(ϵ -caprolactone) (PCL). These materials are most commonly found in surgical products such as resorbable sutures, meshes, or orthopedic fixation devices [89]. PLA is composed of chiral lactide building blocks that can be polymerized in an enantiomerically pure L form (PLLA) or a racemic D/L form (PDLLA) [90]. PLLA is semi-crystalline and PDLLA is amorphous, resulting in vastly different mechanical properties and degradation rates. PLLA is a rigid polymer with a glass transition temperature (T_g) of 60-65 °C, melting point (T_m) of ~175 °C, and a tensile modulus of 2.7 GPa [91]. PDLLA is a weaker material (1.9 GPa tensile modulus) and has a T_g of 55-60 °C [92]. PLLA and PDLLA are thermoplastics that can be fabricated into scaffolds with a variety of architectures including dense and nanoporous films by solvent-casting and electrospinning, respectively, as well as dense filaments

and macroporous 3-D scaffolds by extrusion and fused deposition modeling techniques. However, relatively high temperatures are required to melt and process PLLA ($> 175\text{ }^{\circ}\text{C}$) and PDLLA ($\sim 130\text{ }^{\circ}\text{C}$).

PLA degrades by hydrolysis of the ester bonds into lactic acid, which is a natural metabolic byproduct and may be cleared by the body as carbon dioxide and water [89]. The accumulation of lactic acid released from degrading PLA and the resulting pH drop in the vicinity of the implant can cause an inflammatory immune response and bone resorption. PLLA takes over 2 years to degrade, and full degradation of PLLA crystallites can take over 5 years, while PDLLA degrades in $\sim 1\text{ yr}$ [89]. PGA is a highly crystalline polymer, resulting in its insolubility in most organic solvents and high stiffness (12.8 GPa tensile modulus) [92]. It has a high melting point ($225\text{ }^{\circ}\text{C}$) and is typically processed by injection molding/extrusion. PGA degrades by hydrolysis in 6-12 months, depending on its molecular weight, into glycolic acid which can be cleared by the body. The degradation behavior and high-strength fiber forming ability of PGA led to its use as the first biodegradable synthetic suture material (Dexon®). However its use has been relatively limited in tissue engineering due to its low solubility, limited high-temperature processing options, and high stiffness. Co-polymers of PLA and PGA, called PLGA, overcome the processing difficulties (solubility) and excessive stiffness of PGA. By varying the ratio of PLA to PGA, the degradation rate can vary from 1-2 months (50/50 ratio) to 6 months (85/15 ratio) [89]. The tunable degradation rates, ease of processing, and established medical uses of PLA and PLGA have led to their wide incorporation in tissue engineering scaffolds.

The use of PCL has generally been restricted to slow degrading drug delivery devices and sutures, but more recently its application has been extended to tissue engineering applications, as reviewed by Woodruff and Huttmacher [93]. PCL is a semi-crystalline polymer that is generally weaker than PLA (400 MPa tensile modulus) and degrades by hydrolysis into caproic acid [91]. It has a Tg of $\sim -60\text{ }^{\circ}\text{C}$ and a Tm of $\sim 60\text{ }^{\circ}\text{C}$. The thermoplastic nature and relatively low melting point of PCL enables its facile processing into a variety of scaffold architectures by techniques such as electrospinning and rapid prototyping. PCL can be degraded by bacterial enzymes but its in vivo degradation modality in humans and animals is limited to hydrolysis [93]. Since PCL is more hydrophobic than PLA, [94] it has a slower degradation rate, with minimal degradation reported even after 2 years in vivo (initial Mw = 66,000 Da) [93, 95].

Poly(ethylene glycol) (PEG) is a hydrophilic polyether that is clinically used in formulating pharmaceuticals, such as for increasing the circulation time of protein therapeutics [96]. This increased circulation time is a result of

the low-fouling nature of PEG as it is known to resist protein adhesion through the entropic penalty of releasing bound water from the hydrophilic PEG surface by approaching proteins [97, 98]. While PEG is non-degradable, PEG chains shorter than 30-50 kDa are readily cleared through the kidneys [96, 99]. Unmodified PEG is not suitable for tissue engineering applications requiring tissue integration because it is non-cell adhesive, non-degradable, and water-soluble. With the addition of bioactive molecules or fillers, however, cross-linked PEG hydrogels have been widely studied for tissue engineering [100]. PEG can also be copolymerized with water-stable and degradable hydrophobic blocks, such as PLA or PCL. Low molecular weight amphiphilic polymers composed of biodegradable hydrophobic blocks and PEG can form nanoparticles that have been used to encapsulate hydrophobic drugs or proteins with extended circulation time [101-103]. High molecular weight (>100 kD) amphiphilic PEG-based polymers can form membranes or gels that are stable in aqueous environments and have been used as degradable anti-adhesion tissue barriers for surgery [104-108]. PEG-based copolymers have also been used for tissue engineering scaffolds as reviewed by Tessmar and Göpferich [109].

1.4 Hybrid Biomaterials for Bone Scaffold Engineering

Biomaterials guide the shape and structure of developing tissue and provide mechanical stability and, therefore, the selection of appropriate biomaterial can have a profound impact on the quality of newly formed tissue. Studies show numerous attempts to develop hybrid or composite biomaterials to combine the beneficial properties of multiple materials. As mentioned previously, current standard methods of treatment for bone defects include autographs and allografts, but associated limitations have driven to the investigations of hybrid materials composed of synthetic osseosupportive biomaterials such as ceramics (HAP, TCP) and polymers (PLLA, PCL, PLGA). For example, *in vivo* studies of HAP-PLLA composite, as a substitute for bone powders, revealed similar biocompatibility characteristics as of HAP and PLLA materials when they were used alone [110]. Osteoconductivity studies of nano-sized β -TCP and PLA composites, that were prepared by freeze-drying method, showed that scaffolds containing 30% of nano-sized TCP had better mechanical properties than the scaffolds containing 50% of the same TCP [111]. Scaffolds made of PCL and 20% of HAP or bioglass also showed high interconnected porosity apt for cellular colonization and acceptable mechanical properties for its use as bone substitute [112]. In another study it was demonstrated that scaffolds of PCL coated with CaP had a negligible effect

on the scaffold porosity and compressive Young's modulus [113]. Composites formed of PLGA and β -TCP were also studied; results showed that coating PLGA with β -TCP enhance mechanical strength and so indicating such composite potential for load-bearing bone tissue regeneration [114]. Similarly, enhanced mechanical response was obtained when HAP-PLGA) composites were compared to the reference neat PLGA [115]. Studies of a composite scaffolds of PLGA and HAP fabricated by solvent casting and particulate-leaching method revealed that HAP-PLGA scaffolds, seeded with autologous bone marrow mesenchymal stem cells, had a better interface of tissue response and higher mineralization than PLGA [116]. This study also showed that typical bone synostosis between the implant and bone tissue was found in HAP-PLGA, while only fibrous tissue formed in PLGA.

Natural polymers consisting of proteins (collagen, fibrin gels, silk) or polysaccharides (chitin/chitosan, alginate, hyaluronic acid derivatives) also were studied as potential materials for intercalating bioceramic into the organic matrix [117-122]. However, these polymers, compare to the synthetic, often show limited mechanical properties, immunogenic potential, or insufficient supply [123, 124]. On the other hand, most synthetic polymers are highly hydrophobic and the incorporation of a biological polymer, such as collagen, gelatin or hyaluronic acid is a popular method to alter the physicochemical properties of the matrix and promote biological response [8, 119, 122, 125, 126]. Gelatin, derived from collagen, is a particularly attractive biomolecule for bone-scaffold engineering because of its lower cost, commercial availability, and well-defined physicochemical properties [127]. Different applications in bone and improved functionalities of scaffolds have been demonstrated. Kumar Teolia *et al.* have shown, for example, that the incorporation of gelatin into bone cement material enhances its osteoconductive properties [128]. It has also been shown that 3D printed scaffolds containing nano-apatite and alginate/gelatin polymers can promote the positive proliferation and osteogenic differentiation of stem cells [129].

With regard to the PMMA polymer, several PMMA-bioceramic composites have been studied as alternatives to PMMA with objective to improve bioactivity and accelerate bone restoration. For instance, to improve the filler/cement interface the β -tricalcium phosphate (β -TCP) has been encapsulated with poly(ethylene glycol) (PEG) and later incorporated to a poly(methyl methacrylate) bone cement [130]. In another study, the preparation of nanocomposite composed of HAP and carbon-nanotube reinforced PMMA has been reported [131]. Furthermore, Chen *et al.* demonstrated enhanced bioactivity of silicate bioceramic-PMMA composite

compare to that of neat PMMA [132], while results obtained by Ravarian *et al.* showed that PMMA-bioactive glass composite support osteoblast growth and differentiation [133]. This brief literature overview shows that there is still a need for bone tissue engineering strategies and producing the scaffolds that broaden their application potential.

1.5 Porous Scaffolds (Polymer-Matrix Composites)

The ideal engineered scaffold is a porous interconnected structure that allows cells to migrate and function within its confines (osteoconductive), provides factors that stimulate the proliferation and differentiation of progenitor or osteogenic cells (osteoinductive), and is capable of assimilating into surrounding tissue (osseointegrative), eliminating potential for infection [123, 134]. Therefore, a current research trend is to fabricate three-dimensional (3D) scaffolds with architectures mimicking the 3D interconnected porosity of a natural bone, and having an ability to guide cellular attachment and promote a bone growth [135, 136]. The properties of such multifunctional materials depend on characteristic properties of constituencies, *i.e.* particle size, shape, crystallinity, specific surface area, pore diameter and chemical stability [53]. The polymeric phase of the composite material, as outlined earlier, can additionally serve as porosity, toughness or hydrophilicity enhancing agent, as well as a carrier for growth factors and therapeutic drugs [137-139]. For example, porous β -TCP scaffolds coated with a PLLA network structure were fabricated by changing the concentration of PLLA and dichloromethane (DCM) solution [140], and presented results indicate that structure of the PLLA membrane, such as pore size and thickness of the membrane, could be changed by manipulating the concentration of PLLA. The PLGA/HAP and collagen composites were also prepared with potential for biological applications [141], where porosity and tensile strength were studied.

To create 3D composite scaffolds with different porosities, a variety of techniques have been used, of which gas-foaming [142, 143], porogen leaching [144], microsphere sintering [145] and phase separation/freeze-casting [146-148] can be mentioned. 3D printing technology makes it possible to produce scaffolds with a high degree of complexity and precision at a micron level [129, 149, 150], and a selective laser sintering (SLS) method has also been used to produce 3D structures with well-defined interconnected pores [151]. Studies show that even though variety of materials, and porosity inducing methods were adopted and different porous scaffolds with many desirable features were produced, there are various areas in which further

research can be conducted to improve viability of porous 3D scaffolds for bone regenerative medicine and clinical use.

1.6 Biomaterial Studies Using Computed Tomography

The development of new bone-replacement materials and biofunctionalization strategies thus requires an accurate assessment of the scaffold structure. Radiology is important in the diagnostic assessment of the bone tissue, especially in dental and maxillofacial diseases [152]. An established technique that provides three-dimensional information is computed tomography (CT) [153-155], which is non-destructive and is used for imaging of internal structures based on the density distribution in the materials microstructure. CT can provide a fast quantification of scaffold density which is highly correlated to properties such as strength, stiffness, and toughness [156, 157], CT has been used extensively to quantify the 3D geometry of bone, to determine the bone mineral density and to measure the mean degree of mineralization [128, 153, 158].

The working principle of the medical X-ray CT scanner (Figure 5(a)) is that X-rays, generated in the X-ray tube, interact with a material and the intensity of X-ray photons that reach the detector is quantified. X-ray tube is in a fixed position in relation to the detectors, which in medical CT scanners rotate around the scanned object (Figure 5(b)). The other CT scanners possess system when scanned object rotates while the X-ray tube and detectors remain stationary.

(a)



(b)

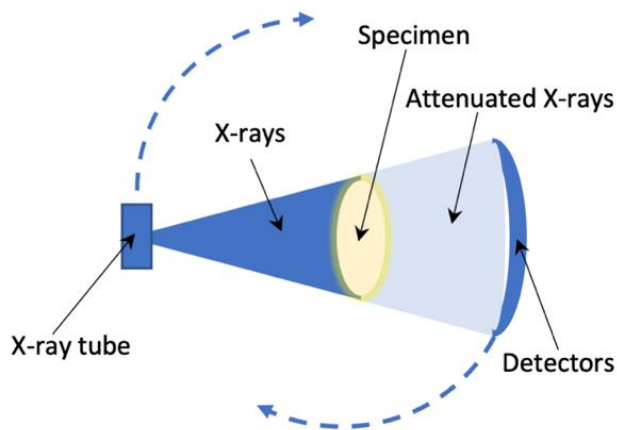


Figure 5. (a) A medical X-ray computed tomography (CT) scanner used to evaluate structure of fabricated composite scaffolds (Department of Engineering Sciences and Mathematics, Shellefteå, Sweden), and (b) schemaitic representation of the working principle of medical CT scanner when X-ray beam interacts with specimen.

The availability for usage of cone-beam computed tomography (CBCT) provides opportunities to request multiplanar imaging. Most X-ray practitioners are familiar with the thin-slice images produced in the axial plane by conventional helical fan-beam CT. CBCT allows the creation in “real time” of images not only in the axial plane but also 2-dimensional (2D) images in the coronal, sagittal and even oblique or curved image planes — a process referred to as multiplanar reformation (MPR). In addition, CBCT data are

amenable to reformation in a volume, rather than a slice, providing 3-dimensional (3D) information. Computed tomography can be divided into 2 categories based on acquisition x-ray beam geometry; namely: fan beam and cone beam (Figure 6).

Fan-Beam CT Technology. In fan-beam scanners, an x-ray source and solid-state detector are mounted on a rotating platform (Figure 6 top picture). Data are acquired using a narrow fan-shaped x-ray beam transmitted through the patient. The patient is imaged slice-by-slice, usually in the axial plane, and interpretation of the images is achieved by stacking the slices to obtain multiple 2D representations. The linear array of detector elements used in conventional helical fanbeam CT scanners is actually a multidetector array. This configuration allows multi-detector CT (MDCT) scanners to acquire up to 64 slices simultaneously, considerably reducing the scanning time compared with single slice systems and allowing generation of 3D images at substantially lower doses of radiation than single detector fan beam CT arrays [159].

Cone-Beam CT Technology. CBCT scanners are based on volumetric tomography, using a 2D extended digital array providing an area detector. This is combined with a 3D x-ray beam (Figure 6 bottom picture). The cone-beam technique involves a single 360° scan in which the x-ray source and a reciprocating area detector synchronously move around the sample. At certain degree intervals, single projection images, known as “basis” images, are acquired. These are similar to lateral cephalometric radiographic images, each slightly offset from one another. This series of basis projection images is referred to as the projection data. Software programs incorporating sophisticated algorithms including back-filtered projection are applied to these image data to generate a 3D volumetric data set, which can be used to provide primary reconstruction images in 3 orthogonal planes (axial, sagittal and coronal) [160-162]. This imaging modality is capable of providing sub-millimeter resolution (2 line pair/mm) images of higher diagnostic quality, with shorter scanning times (~60 s). Radiation exposure dose from CBCT is 10 times less than from conventional CT scans (during maxillofacial exposure (68 μ Sv compared with 600 μ Sv of conventional CT) [163].

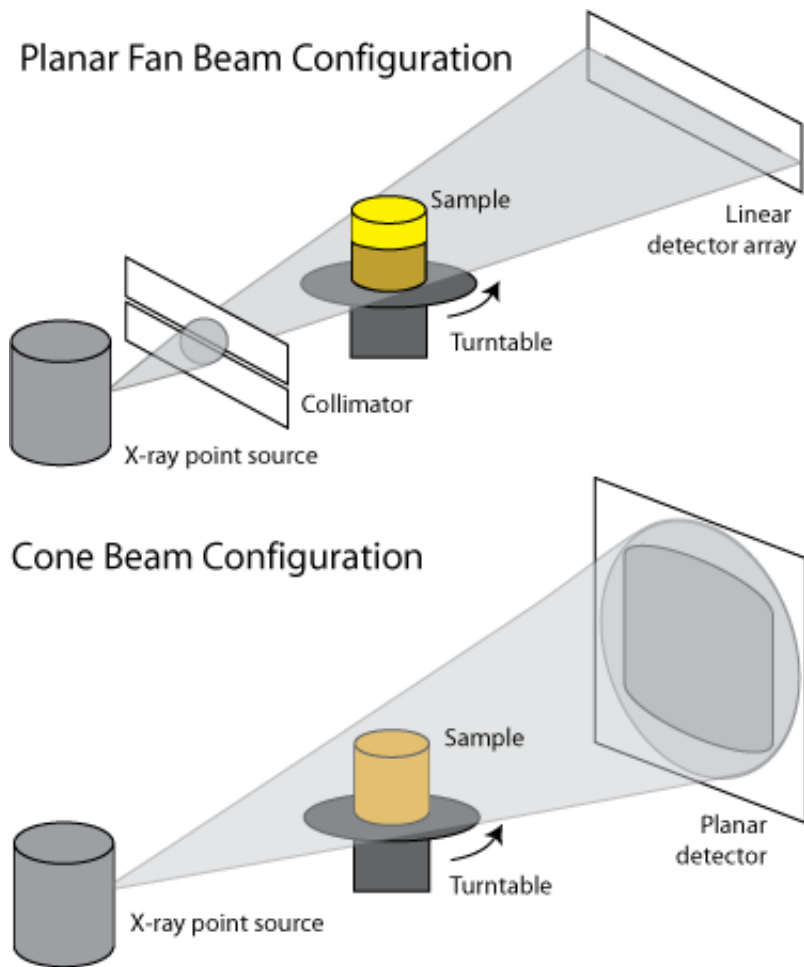


Figure 6. Schematic diagrams of CT data acquisition modes showing of different beam configurations.

2. EXPERIMENTAL PART

2.1. Chemicals and Reagents

In this work the following materials were used:

1. Calcium nitrate tetrahydrate ($\text{Ca}(\text{NO}_3)_2 \cdot 4\text{H}_2\text{O}$, $\geq 98\%$, Fluka),
2. Sodium nitrate (NaNO_3 , 99.5%, Chempur),
3. Tetraethyl orthosilicate ($\text{Si}(\text{OC}_2\text{H}_5)_4$, TEOS, 98 %, Aldrich),
4. Triethyl phosphate ($\text{PO}(\text{C}_2\text{H}_5)_3$, TEP, $\geq 98\%$, Aldrich),
5. Citric acid ($\text{C}_6\text{H}_8\text{O}_7$), CA, $\geq 99.5\%$, Sigma-Aldrich),
6. Methyl 2-methylprop-2-enoate (methylmethacrylate, MMA, $\text{C}_5\text{H}_8\text{O}_2$, Evonik-Degussa GmbH),
7. (Diphenylphosphinyl)-(2,4,6-trimethylphenyl)methanone) (Genocure TPO (defined as TPO), $\text{C}_{22}\text{H}_{21}\text{O}_2\text{P}$, Rahn USA Corp.),
8. (2-Benzyl-2-(dimethylamino)-4'-morpholinobutyrophenone) (Irgacure 396 (defined as BDMP), $\text{C}_{23}\text{H}_{30}\text{N}_2\text{O}_2$, BASF Corp.),
9. Sodium chloride (NaCl , $\geq 99\%$, Aldrich),
10. Sodium hydrogen carbonate (NaHCO_3 , premium, Sigma),
11. Potassium chloride (KCl , $\geq 99.0\%$, Sigma),
12. Potassium phosphate dibasic trihydrate ($\text{K}_2\text{HPO}_4 \cdot 3\text{H}_2\text{O}$, $\geq 99.0\%$, Sigma-Aldrich),
13. Magnesium chloride hexahydrate ($\text{MgCl}_2 \cdot 6\text{H}_2\text{O}$, BioXtra $\geq 99.0\%$, Sigma-Aldrich),
14. Calcium chloride (CaCl_2 , anhydrous, BioReagent, $\geq 96.0\%$, Sigma),
15. Sodium sulfate (Na_2SO_4 , BioXtra, $\geq 99.0\%$, Sigma-Aldrich),
16. Tris(hydroxymethyl)aminomethane ($(\text{CH}_2\text{OH})_3\text{CNH}_2$, ACS Reagent, $\geq 99.8\%$, Sigma-Aldrich),
17. Hydrochloric acid (HCl , ACS, 36.6-38%, Alfa Aesar) solution,
18. Calcium acetate hydrate ($\text{Ca}(\text{CH}_3\text{COO})_2 \cdot \text{H}_2\text{O}$, $\geq 99\%$, Roth),
19. Diammonium hydrogen phosphate ($(\text{NH}_4)_2\text{HPO}_4$, 99.9%, Alfa Aesar),
20. Polyethylene glycol ($\text{H}(\text{OCH}_2\text{-CH}_2)_n\text{OH}$, PEG, 4600, Aldrich),
21. Aqueous ammonia (NH_3 (aq.), 32% aq. sol., Merck),
22. Dipentaerythritol hexa-acrylate (DPHA, Miramer (M600), $\text{C}_{25}\text{H}_{32}\text{O}_{12}$, Rahn USA corp.),
23. Ethylene glycol dimethacrylate (EGDMA, crosslinker, $\text{C}_{10}\text{H}_{14}\text{O}_4$, Merck),
24. Gelatin powder (food grade, locally purchased),
25. Azodicarbonamide (ADCA, $\text{C}_2\text{H}_4\text{N}_4\text{O}_2$, foaming agent, A.F.Supercell Co., Ltd),

26. Polyethylene glycol diacrylate (Miramer M280, PEG400DA, Miwon Commercial Co., Ltd.),

27. (2,4,6 Trimethylbenzoyldiphenylphosphine oxide /dimethylhydroxyacetophenone, 1:1 (Genocure LTD, photoinitiators, RAHN).

28. Dimethyl sulfoxide (DMSO, $(\text{CH}_3)_2\text{SO}$, Gaylord).

2.2. Synthesis and Processing

Sol-gel synthesis of glass-ceramic (GC) powders (*included in Paper 1*): To synthesize GC powders a modified synthesis procedure published elsewhere [164] was used. Firstly, aqueous 5 mM $\text{C}_6\text{H}_8\text{O}_{17}$ solution was prepared. To 26 mL of this solution was added 1 mL of TEP and 11.6 mL of TEOS. The mixture was stirred for 1 h at 65-70 °C until clear sol was obtained. In the following step, $\text{Ca}(\text{NO}_3)_2 \cdot 4\text{H}_2\text{O}$ (7.15 g, 0.03 mol) and NaNO_3 (4.66 g, 0.05 mol) salts were added and mixture was further stirred for 60 min at 70 °C until sol turned into clear and transparent gel (the molar ratios of Ca : P : Na : Si was 0.4 : 0.1 : 0.6 : 1). This Si-Ca-Na-P-O gel was then dried in the oven at 100 °C for 24 h and turned into fine powders. Prepared powders were then calcined at 600, 700 and 1000 °C (heating rate 1 °C/min) for 5 h in air with intermediate grinding in agate mortar. Obtained GC material calcined at 600 °C was further used to prepare GC-PMMA composites.

Preparation of GC-PMMA composite pellets (*included in Paper 1*): First, the starting components MMA (5.00 g, 0.05 mol), TPO (1 g, 0.003 mol) and BDMP (1g, 0.003 mol) were mechanically mixed in a beaker. MMA to TPO to BDMP weight ratio was 71.4 : 14.3 : 14.3. Photoinitiators TPO and BDMP were used for the bulk and surface cure, respectively. The GC powders calcined at 600 °C were then added to the prepared MMA-TPO-BDMP mixture (GC to MMA-TPO-BDMP weight ratio was 75 : 25) and further mixed until the homogeneous GC-PMMA composite precursor was obtained. In the following step, 0.5 g of composite powders were pressed mechanically to cylindrical-shaped specimens of 8 mm in diameter and 5.1 mm in height (average value reported) using VLP hydraulic press (Enerpac) (10 kN) and left under natural light conditions at room temperature for 5 days to enable photopolymerization of the photoactive compounds.

Pellets of neat PMMA and GC-PMMA composites with fractional GC content of 85, 90 and 95% were additionally fabricated using a procedure described above. It is noteworthy that at the concentrations of MMA-TPO-BDMP mixture above 25% the preparation of pellets was constricted due to the liquidised form of the MMA-TPO-BDMP-GC mixture.

Preparation of a simulated body fluid (SBF) solution and composite dissolution (included in Paper 1): 1 L of the SBF electrolyte solution was prepared by dissolving NaCl (7.996 g, 0.138 mol), NaHCO₃ (0.350 g, 0.004 mol), KCl (0.224 g, 0.003 mol), K₂HPO₄·3H₂O (0.228 g, 0.001 mol), MgCl₂·6H₂O (0.305 g, 0.001 mol), CaCl₂ (0.244 g, 0.002 mol) and Na₂SO₄ (0.071 g, 0.005 mol) into the distilled water. Prepared solution was buffered at pH of 7.25 with 50 mmol/L of (6.057 g, 0.050 mol) (CH₂OH)₃CNH₂ and 40 mL of 1 kmol/L HCl solution. The SBF solution (ion concentrations are shown in Table 6) was prepared according to Kokubo *et al.* [165].

Table 6. The concentrations (mmol/L) of ions in the SBF.

Ion	Na ⁺	K ⁺	Mg ²⁺	Ca ²⁺	Cl ⁻	HCO ₃ ⁻	HPO ₄ ²⁻	SO ₄ ²⁻
Concentration, mmol/L	142.0	5.0	1.5	2.2	147.8	4.2	1.0	0.5

GC(85%)-PMMA(15%), GC(90%)-PMMA(10%) and GC(95%)-PMMA(5%) pellets were soaked in 20 mL of SBF solution and kept in closed fluoroplastic PFA (Roth) tins (placing one sample into each tin) at a starting pH of 7.25 at 37 °C for 1, 2 and 3 weeks.

Carbonated-HAP synthesis (included in Paper 2): Carbonated hydroxyapatite was synthesized as previously reported [76]. (Ca(CH₃COO)₂·H₂O (5.285 g, 0.03 mol) and (NH₄)₂HPO₄, (2.377 g, 0.018 mol) were first dissolved in separate beakers, each in 25 mL of distilled water. To each of these solutions, 25 mL of 6% PEG aqueous solution was then added as a crosslinking agent and the mixtures were stirred for 30 min at 55–60 °C. In the following, NH₃ (aq.) was added to pH 11. These mixtures were then stirred for 20 min at 65–80 °C and finally mixed together (Ca : P ratio of 1.67). The white Ca–P–O precipitate was then stirred for 30 min in a beaker covered with a watch glass and latex cover to prevent evaporation of ammonia, after which the suspension was evaporated at 80–100 °C leaving a Ca–P–O gel. The gel was dried at 150 °C for 24 h, and samples were calcined at 400, 600, 680 and 800 °C for 5 h in air (with the temperature increasing at a rate of 1 °C min⁻¹ from 25 °C) with intermediate grinding between each calcination procedure.

Preparation of multi-composite scaffolds (included in Paper 2): The monomers DPHA and EGDMA were first mechanically mixed in a beaker (weight ratio of DPHA : EGDMA 4 : 1). Gelatin, a biopolymer used as a porosity agent, was then added to the mixture and further mixed until a homogeneous composite mixture was obtained. The weight ratios of DPHA-EGDMA : gelatin were 50 : 50 (10 g : 10 g), 75 : 25 (15 g : 5 g) and 95 : 5

(19 g : 1 g) and these are designated as Mix-1, Mix-2 and Mix-3, respectively. cHAP powders heated at 800 °C were then introduced into the mixtures as a filler. The Mix-1 mixture exhibited a low viscosity and a larger amount of cHAP therefore was added (weight ratios of Mix-1 : cHAP, and of Mix-2 : cHAP and Mix-3 : cHAP were 2.1 g : 1 g, and 1.5 g : 1 g, respectively). Subsequently, 0.02 g of the photoinitiator TPO was added to all three systems and the resultant mixtures were vigorously mixed for 5 min using a Heidolph silent crusher M homogenizer. Finally, the mixtures were weighed in 0.5 g portions and the pellets of ca. 0.5 cm in diameter and 0.1-0.2 cm in thickness were placed on the silicon plate and illuminated with a dental lamp (UV irradiation at a wavelength of 365 nm) at room temperature for 5 min to achieve photopolymerization. The polymerized material was then further cured at 40 °C for 24 h. The composites were designated according to the acrylate and gelatin ratio within the initial organic matrix, i.e. acrylate(50%)-gelatin(50%)-cHAP, acrylate(75%)-gelatin(25%)-cHAP, acrylate(95%)-gelatin(5%)-cHAP.

Low crystallinity carbonated-HAP synthesis

Low crystallinity carbonated hydroxyapatite (lc-cHAP) was synthesized as reported in the previous paragraph. $\text{Ca}(\text{CH}_3\text{COO})_2 \cdot \text{H}_2\text{O}$, $(\text{NH}_4)_2\text{HPO}_4$, 6% PEG aqueous solution and, NH_3 (aq.) were used to prepare the white Ca-P-O precipitate (Ca : P ratio of 1.67). This Ca-P-O precipitated material was then stirred for 30 min in a beaker covered with a watch glass and latex cover to prevent evaporation of ammonia, after which the suspension was evaporated at 80–100 °C leaving a Ca-P-O gel. The gel was dried at 150 °C for 24 h, and samples were calcined at 400, 600, 650 °C for 5 h in air (with the temperature increasing at a rate of 1 °C min⁻¹ from 25 °C) with intermediate grinding between each calcination procedure.

Preparation of porous hybrid inorganic-organic (lc-cHAP-polyethylene glycol diacrylate (PEGDA)) composite. Porous composite consisting of lc-cHAP and polymerized-PEGDA was prepared by free radical copolymer crosslinking reactions. The processing steps are as follows: azodicarbonamide (ADCA), used as foaming agent, was dissolved in DMSO and mixture of PEGDA and ethylene glycol dimethacrylate (EGDMA), used as crosslinker, was added. Powders of synthesised lc-cHAP calcined at 650 °C, and photoinitiators Genocure then was incorporated to the viscous liquid phase. All components were mixed in a proportions (wt%) as shown in a Table 7 below:

Table 7. Materials and their amounts used to prepare porous HAP-EGDMA composites.

Compound	CAS	Weight, g	Wt _m %
Lc-cHAP	-	0.5	37.2
ADCA (azodicarbonamide)	123-77-3	0.02	1.5
PEGDA (polyethylene glycol diacrylate (Miramer M280))	36570-48-9	0.25	18.6
EGDMA (ethylene glycol dimethacrylate – crosslinker)	97-90-50	0.025	1.8
Genocure LTD (2,4,6 Trimethylbenzoyldiphenylphosphine /oxide dimethylhydroxyacetophenone, 1:1)	-	0.05	3.7
DMSO (dimethyl sulfoxide)	67-68-5	0.5	37.2
	TOTAL:	1.345 g	100%

Obtained viscous mixture was further processed to form porous composites via self build unit (Figures, 7 and 8). This mixture was pushed through the needle (variable diameter, depends on needed sample size) placed in a heating element. Temperature value is set up in accordance with decomposition temperature of blowing agent ADC and varies in a range 180-200°C. UV curing was carried out using Demetron OPTILUX 150 dental curing light system.

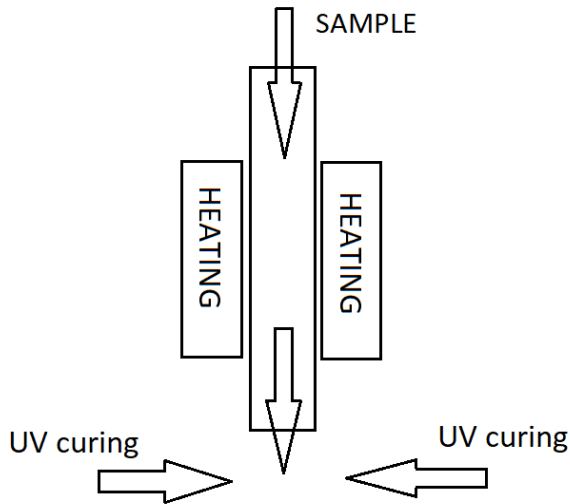


Figure 7. Schematic representation of the build devise used to form hybrid HAP-EGDMA composites.

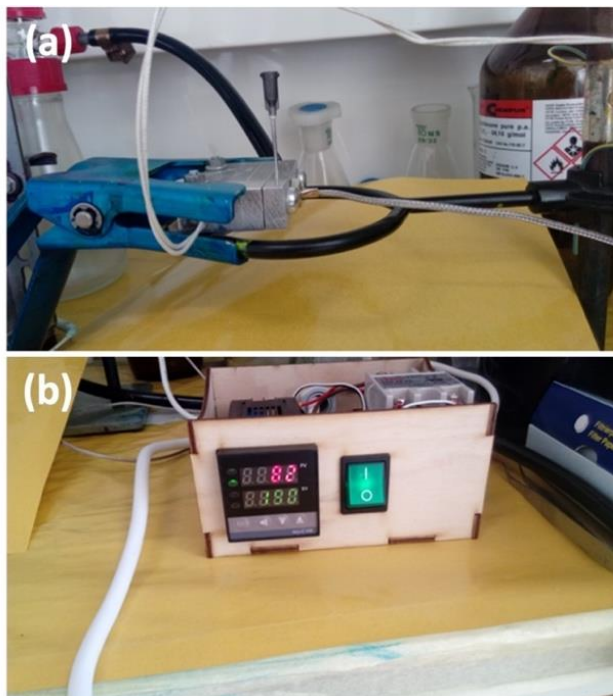


Figure 8. (a) Heating unit and needle for sample formation and (b) Temperature control unit for heating element.

2.3 Characterization Techniques

Thermogravimetric analysis (TG) and differential scanning calorimetry (DSC) of the Si–Ca–Na–P–O and Mg–Ca–P–O gels were performed using Perkin Elmer STA 6000 Simultaneous Thermal Analyzer. Dried samples of 5–10 mg were heated from 25 to 900 °C at a heating rate of 10 °C/min (in a dry flowing air (20 mL/min).

The phase composition of annealed GC and cHAP powders was studied by X-ray diffraction (XRD, Rigaku, MiniFlex II, Cu-K α radiation, $\lambda = 0.1542$ nm, 40 kV, 100 mA, $2\theta = 10\text{--}60^\circ$) with a step of 0.02° and scanning speed of $2^\circ/\text{min.}$) analysis. Identification of crystalline phases was achieved by comparing the experimentally obtained XRD patterns to the database provided by JCPDS (Joint Committee on Powder Diffraction Standards). The average crystallite size of cHAP was estimated by the Scherrer equation, $d_{\text{XRD}} = K\lambda/\beta \cos \theta$, using the full-width at half maximum (FWHM) of the (002), (222) and (004) Bragg reflections. Rietveld analysis for XRD pattern ($2\theta = 10\text{--}70^\circ$) with a step of 0.02° and scanning speed of $2^\circ/\text{min.}$) of cHAP was performed using Match! and FullProff software.

Morphological features of the samples and elemental distribution were evaluated using field emission scanning electron microscopy (FE-SEM, SU70, Hitachi) equipped with the energy dispersive X-ray spectrometer (EDS) and using INCA software (Oxford Instruments). The samples were examined using secondary electron (SE) imaging mode. The electron beam acceleration voltage was 5 kV and 20 kV for SEM and EDS analysis, respectively. X-ray acquisition time of 60 seconds was used to obtain the EDS spectra (9 spectra were obtained over different regions for each sample). Morphological features and elemental distribution of acrylate-gelatin-chAP composites were evaluated using a table-top scanning electron microscope (SEM, TM3000, Hitachi, 15.0 kV acc. voltage) equipped with an energy dispersive X-ray spectrometer (EDS) using INCA software (Oxford Instruments).

Infrared spectra of the ceramic glass and composite powder samples were recorded using Fourier transform infrared (FT-IR) spectrometry (Frontier FT-IR), Perkin Elmer, BaF₂ plate (ZnSe ATR crystal, liquid-nitrogen-cooled mercury cadmium telluride (MCT) detector), 4000-600 cm⁻¹. IR absorbance spectra the surface of composite pellets before and after the dissolution were recorded in reflectance geometry using Thermo scientific Nicolet iZ10 spectrometer. Infrared spectra of the ground composite powders were recorded with a Fourier transform infrared (FTIR) spectrometry (Frontier FTIR, PerkinElmer, ZnSe/Diamond ATR crystal, DTGS detector, 4000-600 cm⁻¹, 4 scans). Raman spectra were recorded at room temperature using combined Raman and scanning near field optical microscope (SNOM) WiTec Alpha 300 R equipped with 532 nm excitation laser source. Chromatographic analysis was performed with Thermo Scientific TRACE GC Ultra GAS CHROMATOGRAPH with flame ionization detector. Optical images were taken with LOMO Biolam M microscope.

The optical contact angle measurements were performed using DataPhysics OCA 15EC system (n = 4 for each multi-composite scaffold).

Dissolution of fabricated composite pellets was monitored by measuring the concentrations of Si, Ca and P in soaking solutions. Quantitative determination of the elements was performed using Perkin Elmer Optima 7000 DV inductively coupled plasma optical emission spectrometer (ICP-OES).

The compressive strength tests were performed with a universal testing machine “Haunsfield H10KS” (Hounsfield Test Equipment Ltd, Redhill, UK) and software “Qmat Professional”. The cell load was of 10 kN with a resolution of 0.1 N (load measurement accuracy: 0.5% of indicated load from 2% to 100% capacity). Load speed was of 20 mm/min (position measurement accuracy: 0.001 mm, speed accuracy: 0.005% of set speed). To calculate

density (ρ), the weight, height and diameter of prepared specimens were estimated using precision balance Mettler toledo MS1003S ($e = 0.01$ g, $d = 0.001$ g) and DIGIMET indicator ($e = 0.01$ mm, $d = 0.001$ mm) from Helios Preisser. To eliminate the impact of varying densities of specimens (which forms during its preparation) on compressive strength, the estimated strength σ_{estm} , corresponding to mean density of specimens, was calculated according to eqn (1):

$$\sigma_{estm} = \sigma_i \frac{\rho_{meas}}{\rho_i} \quad (3)$$

where σ_i is the actual strength of sample, ρ_{mean} – mean density of tested samples (1905 kg/m³) and ρ_i – density of the tested sample.

Computed tomography (CT) and conventional radiography. A medical CT-scanner Siemens Somatom Emotion Duo with a field of view of 500 × 500 mm² represented in a grayscale 512 × 512 pixel image, which gave a resolution of 0.98 mm, was used to evaluate the density of the cHAP-acrylate-gelatin composites. In a CT, one pixel represents a three-dimensional entity (voxel) of the material scanned with the dimensions of the pixel and the thickness of the scanning beam (the beam depth). In order to evaluate average density of the composites from the CT-image, the images were converted into a binary image by using the image processing method thresholding. This method replaces each pixel in the image with a black pixel if it's intensity is less than a fixed constant, or with a white pixel if it's intensity is greater than that constant. A black pixel is represented by the value 0, and white pixel is represented by the value 1. In this analysis, the fixed constant was set to 100 kg/m³. When the composite is isolated by the thresholding method, every index of nonzero elements is found in the binary image. These indices are then used to obtain the corresponding pixels in the original CT image to calculate the average density (kg m⁻³) by following equation:

$$\bar{\rho} = \frac{1}{n} \sum_{i=1}^n \rho_i \quad (4)$$

where n is the number of pixels and ρ_i is the density value in the specific pixel (voxel). A beam energy level of 80 kV and 110 kV was used to scan the specimens (a total of 24 scans with a resolution of 1 mm over a total length of 2 cm). Matlab software was used to process 2D images of the composite pellets.

Cone beam computed tomography (CBCT) was performed using Morita veraview R100 (Japan) system with a loading factor of 90 kV and 5 mA.

Satelec X-Mind DC (Acteon, UK) intra-oral X-ray unit (X-ray tube: New Toshiba DG 073B DC tube, voltage: 60-70 kV, anode current: 4-8 mA, focal

spot: 0.7 mm, total filtration: equivalent to 2 mm Al at 70 kV, tube inherent filtration: equivalent to 0.8 mm Al at 70 kV, long cone: focus to cylinder tip distance = 31 cm, exposure time of 0.02-3.2 s) was used to take radiographic images of the scaffolds.

3. RESULTS AND DISCUSSIONS

3.1 Glass-Ceramic (GC)-Polymethyl Methacrylate (PMMA) Composite

In this part the processing and dissolution in the simulated body fluid (SBF) of hybrid inorganic-organic composites is described. The mechanical property, i.e. compressive strength, is also presented and discussed.

3.1.1 Sol-Gel Synthesis of Na-Ca-Si-P-O Glass-Ceramics

TGA was performed to evaluate thermal behaviour of GC and determine the calcination temperature of the Si-Ca-Na-P-O gel powders. TG/DTG and DSC curves of representative Ca-P-Na-Si-O gel powders are shown in Figure 9.

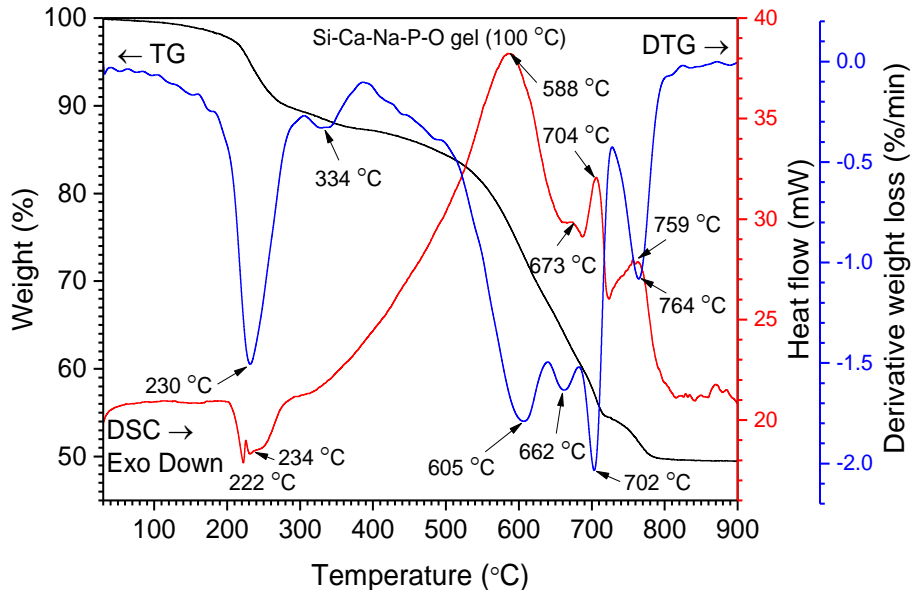


Figure 9. TG/DTG and DSC curves of Si-Ca-Na-P-O gel dried at 100 °C.

Six main steps of mass loss are clearly seen in DTG curve. The first very small weight loss of ~ 3% without significant events in the DTG curve was observed at temperatures up to 200 °C and assigned to the removal of adsorbed water. The second step of weight loss of 6% observed in the range of 220-270 °C and is assigned to the decomposition of precursor gel and evolution of NO_x gasses and organic fragments. This is also evident from the exothermic signals in the DSC curve (maxima at 222 °C and 234 °C). The next small weight loss of about 2% observed at 334 °C (DTG curve) was further assigned to the decomposition of organics and evolution of absorbed water. Then, the

significant weight loss at around 580-710 °C and simultaneous broad endothermic peak (DSC curve) with three maxima at 605, 662 and 702 °C (DTG curve) takes places. This step is related to the nucleation of primary crystals and crystallization processes of glass ceramic. Similar results were reported by Boccaccini et al. where sintering and crystallization behaviour of bioglass powders was investigated [166]. One shall note that in the thermal treatment of Ca-P-Na-Si-O gel powders more than one crystalline phase may form depending on the temperature [167, 168]. The last thermal effect with a weight loss of ~ 5% is observed at 764 °C (DTG curve) followed by endothermic reaction (DSC curve, maxima at 759 °C) and can be further assigned to the increased crystallization of glass-ceramic powders as well as decomposition of nitrate into nitrite [169] and evolution of gasses.

3.1.2 Structural Characterization of Na-Ca-Si-P-O Glass-Ceramics

XRD pattern of Ca-P-Na-Si-O gel powders annealed at 600 and 1000 °C are presented in Figure 10.

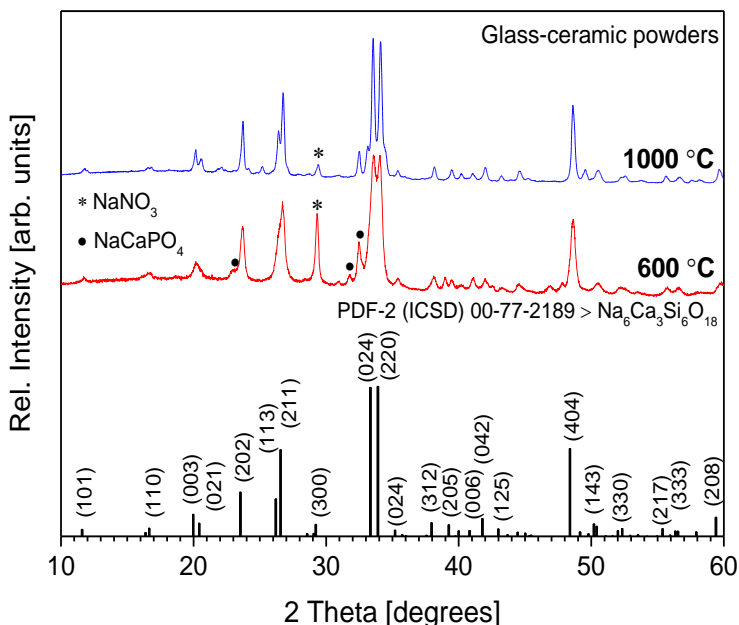


Figure 10. X-ray diffraction patterns of glass-ceramic powders annealed at 600 and 1000 °C.

Significant reflections in the XRD pattern were observed at $2\theta = 11.68^\circ$, 16.73° , 20.13° , 23.64° , 26.65° , 33.56° , 34.07° , 35.33° , 38.03° , 39.46° , 41.04° ,

41.95°, 43.18°, 48.60°, 50.48°, 52.18°, 55.69°, 56.50° and 59.69° confirming crystalline solid formation at around 600 °C. These reflections were assigned to the (101), (110), (033), (202), (211), (024), (220), (024), (312), (205), (006), (042), (125), (404), (143), (330), (217), (333) and (208) diffraction peaks of sodium calcium silicate ($\text{Na}_6\text{Ca}_3\text{Si}_6\text{O}_{18}$) [JCPDS no. 77-2189] phase. The formation of other sodium calcium silicates such as $\text{Na}_2\text{Ca}_2\text{Si}_3\text{O}_9$ [JCPDS no. 22-1455] and $\text{Na}_4\text{Ca}_4\text{Si}_6\text{O}_{18}$ [JCPDS no. 79-1089] phase might also be observed, since different sodium calcium silicates exhibit very similar reference patterns and often consist of a solid solution [164, 170, 171]. The reflections observed at $2\theta = 23.12^\circ$, 31.04° , 31.75° and 32.50° were assigned to the buchwaldite (NaCaPO_4) [JCPDS no. 29-1193] phase, while the intensive reflection at $2\theta = 29.37^\circ$ was assigned to the sodium nitrate (NaNO_3 phase [JCPDS no. 36-1474]). Similar results were reported by Pirayesh and Nychka where NaNO_3 phase was observed at temperatures up to 600 °C [172]. Further annealing at 700 °C (data not presented) and 1000 °C increased crystallinity, whereas the sharp peak of NaNO_3 phase in the XRD pattern slightly diminished. This decrease in the intensity is probably due to the change of material phase, considering that the nitrates at higher temperatures turn into their respective nitrites and oxygen (designated NaNO_2 [JCPDS no. 83-2254] phase) [169].

3.1.3 Structural and Morphological Evaluation of GC-PMMA Composites

To see distribution of glass-ceramic within the PMMA matrix the morphological examination was performed. The surface morphology FE-SEM micrographs of GC powders annealed at 600 °C and selected pellets of GC-PMMA (wt ratios of 75/25 and 95/5) composite are presented in Figure 11.

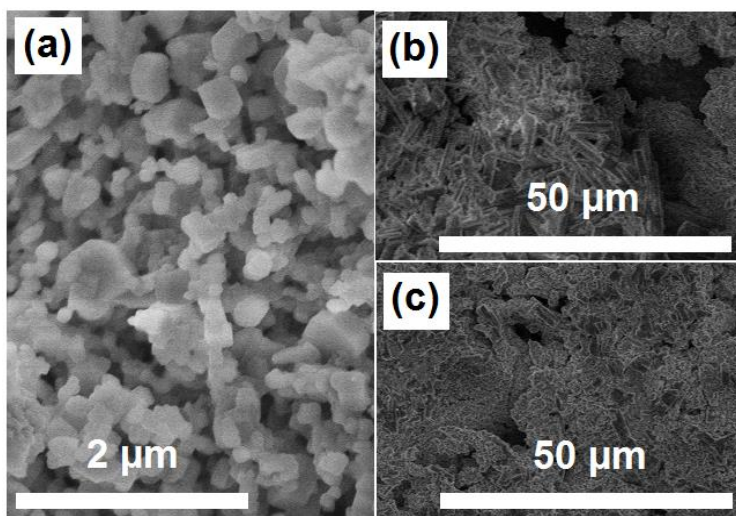


Figure 11. FE-SEM micrographs showing surface morphology of (a) GC powders synthesised at 600 °C, and (b) GC(75%)-PMMA(25%) and (c) GC(95%)-PMMA(5%) composites.

Irregular micro-voids within some areas of composite surface were also observed, while samples of neat PMMA appeared to be dense. The content and distribution of voids varies within different surface regions examined and increases with an increase of PMMA content. This can be attributed to the inorganic-organic composite preparation procedure and non-uniform distribution of glass ceramic material within polymer matrix. The size of the irregular voids was estimated to be in the range of $20 \times 10 \pm 5 \mu\text{m}$ and $1 \times 0.5 \pm 0.25 \mu\text{m}$ for the GC(75%)-PMMA(25%) and GC(95%)-PMMA(5%) composites, respectively (FE-SEM micrographs). One might find that the formed voids can lead to some porosity which is one of the most important characteristics for scaffolding materials, since it allow migration and proliferation of osteoblasts and mesenchymal cells, effective vascularisation, bone ingrowth as well as improves mechanical interlocking between artificial implant biomaterial and surrounding natural bone providing mechanical stability at the interface [37].

Furthermore, the FTIR spectroscopy was performed to evaluate chemical composition of composites. Absorption FTIR spectra of PMMA and GC(75%)-PMMA(25%) composite are presented in Figure 12.

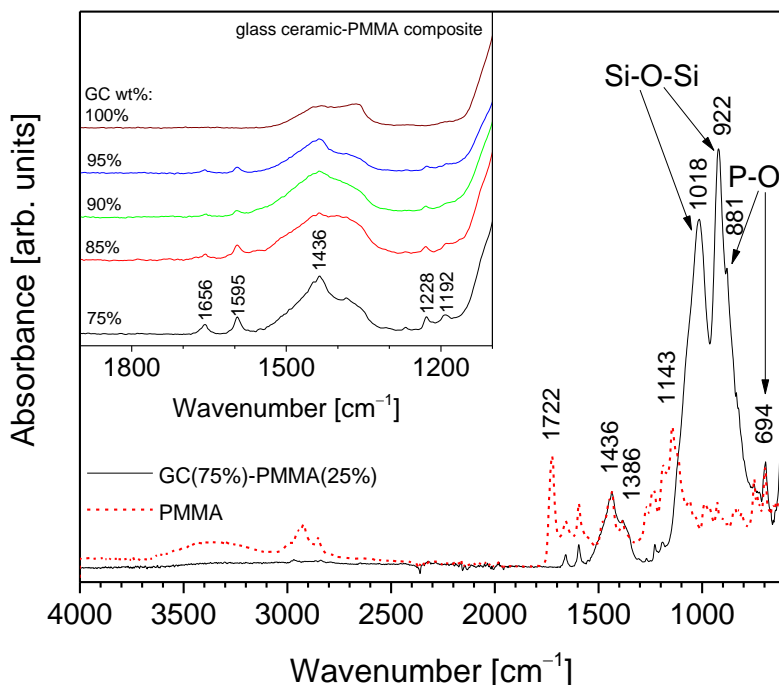


Figure 12. Absorption FTIR spectra of GC(75%)-PMMA(25%) composite and PMMA (Inset: absorption FTIR spectra of GC (synthesised at 600 °C) and GC-PMMA composites in the range of 1100-1900 cm^{-1}).

FTIR spectrum of neat PMMA in the region of 1700-1100 cm^{-1} exhibits characteristic bands located at 1722, 1656, 1595, 1436, 1386, 1228, 1192 and 1143 cm^{-1} . Similar absorption spectrum of PMMA was presented by Gonzalez-Benito and Gonzalez-Gaitano [173]. FTIR spectrum of GC(75%)-PMMA(25%) composite showed broad and distinctive bands in the region of 1100-850 cm^{-1} . Bands centered at 1018 and 922 cm^{-1} were assigned to the Si-O-Si vibrational modes of orthosilicate (SiO_4^{4-}) tetrahedral group, whereas the phosphate vibrations are not very well resolved [174, 175]. The shoulder at 881 cm^{-1} and a couple bands in the 600-550 cm^{-1} region were related to the P-O vibrations which overlap with mixed stretching and bending vibrations of Si-O-Si bond [174, 175]. In the 1500-1350 cm^{-1} region broad bands were obtained and assigned to the PMMA matrix overlapping with C-O vibrations of carbonate group. The enlarged FTIR spectra of glass ceramic powders and GC-PMMA composites in the 1900-1100 cm^{-1} region are presented in Figure 12 inset. The results clearly point out that with increase of PMMA content the intensity of vibrational modes of PMMA (bands located at 1656, 1595, 1228 and 1192 cm^{-1}) also increases. Furthermore, the intense PMMA band centered

at 1722 cm^{-1} assigned to the C=O stretching vibrations [176, 177] disappears in the spectra of GC-PMMA composites.

3.1.4 Mechanical Properties of GC-PMMA Composites

The mechanical properties of GC-PMMA composites were investigated by the uniaxial compressive strength test (Figure 13). In this system, the compressive strength of composites (σ_i) was in the range of 42-50 MPa (the compressive strength of neat PMMA pellets was measured to be 126 MPa) and decreased with the increase of glass ceramic-polymer ratio. Composites containing 75, 85 and 90% of glass ceramic exhibited very similar compressive strength values. The compressive strength of bioactive glass scaffolds spans from 0.2 to 150 MPa and is composition, microstructure and/or fabrication method dependent [36, 178, 179], although macroporous bioactive glass scaffolds can display compressive strength values even below 0.2 MPa [180]. Material crystallinity also plays an important role in mechanical strength and generally increases when the crystalline phase is increased. For example, Daguano *et al.* reported that the amount of crystal phase formed in the bioactive glass improves hardness, fracture toughness, bending strength and elastic modulus of the material depending on the heat treatment temperature [181]. Similar results were obtained in the work presented by Sabree *et al.* showing that ceramic scaffolds made of amorphous material exhibit brittleness compared to those produced of purely crystalline material [182]. The compressive or diametral tensile strength of the PMMA can also be altered by incorporating different additives into the bone cement. [132, 183-185] The density (ρ) values (Figure 13) showed that composites containing 90% and 95% of GC exhibit slightly lower density in comparison to those containing 75% and 85%, while calculated compressive strength at $\rho = 1900\text{ kg/m}^3$ shows that the highest value was obtained of composite containing 90% of GC. One can also observe that composite containing 95% of GC decreased in compressive strength by 11.4% and this is attributed mostly to the small amount of supporting PMMA matrix as well as decreased material density. The results imply that GC(90%)-PMMA(10%) composite yields the highest strength and lowest density compared to all fabricated materials.

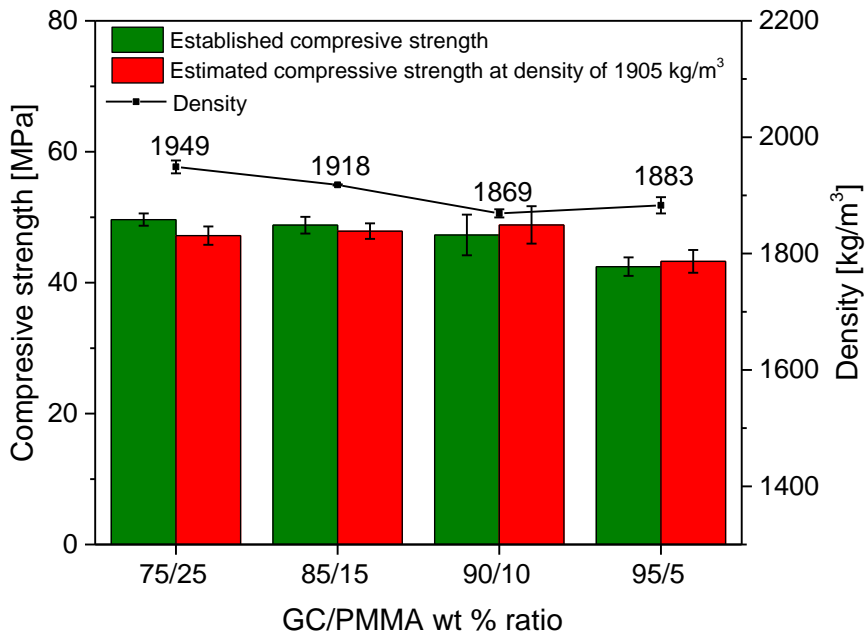


Figure 13. Density of samples, measured compressive strength, and estimated compressive strength at density of 1905 kg/m³ of GC-PMMA composite materials.

The results presented herein demonstrate that fabricated composites overall might be potential material in bone tissue engineering when extreme strength is not required.

3.1.5 GC-PMMA Composite Dissolution in SBF

Figure 14 shows dependence of the concentrations of Si, P and Ca in a soaking solutions as a function of dissolution time for GC(85%)-PMMA(15%), GC(90%)-PMMA(10%) and GC(95%)-PMAA(5%) composite materials.

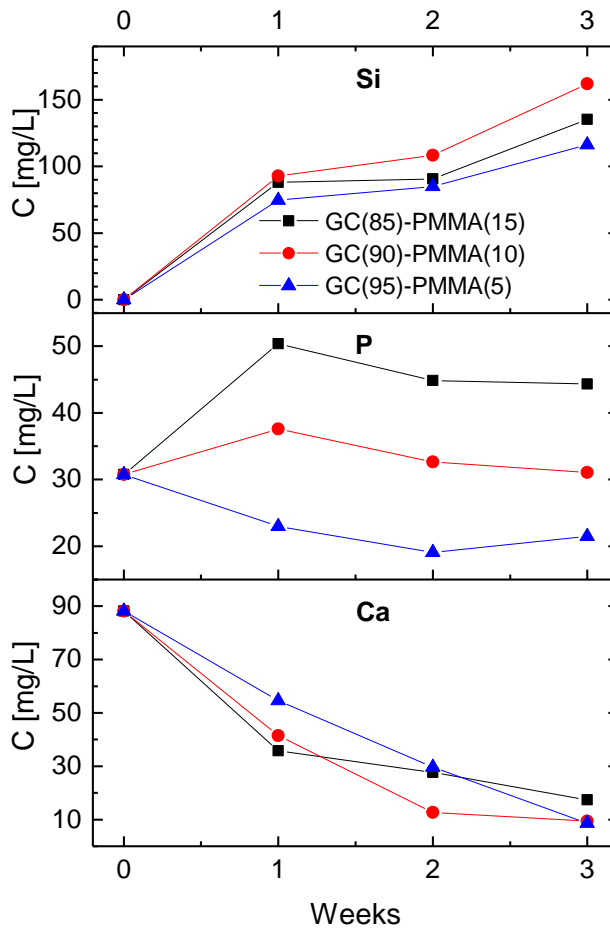


Figure 14. Concentrations of Ca, P and Si in the soaking solution as a function of immersion time.

The concentration of Si in dissolution medium gradually increased over the immersion time and after 3 weeks reached 115 ppm, 135 ppm and 165 ppm for the GC(95%)-PMAA(5%), GC(85%)-PMMA(15%) and GC(90%)-PMMA(10%) composites, respectively, with most significant alteration obtained after the first week (70-90 ppm). This sudden increase in Si concentration shows and indicates the fast dissolution rate of the glass in the SBF. The highest concentrations of the Si were obtained for GC(90%)-PMMA(10%) material and this could be attributed to the higher porosity of composite and faster surface chemistry. Calcium concentration in the dissolution medium, on the contrary, falls gradually (it ranges from 90 ppm to 10-20 ppm). However, different variation in the content of phosphorus was obtained. An increase in P concentration was observed first week after the dissolution for the GC(85%)-PMMA(15%) and GC(90%)-PMMA(10%)

composites, following with small decrease after the second and third week of dissolution. The concentrations of P for the GC(95%)-PMMA(5%) composite initially decreases and for the last week of dissolution slightly increase. Generally, these processes are due to the dissolution-precipitation reactions that occur at glass ceramic surface in contact with SBF. A rapid ion exchange between glass ceramic surface and dissolution medium induces the formation of hydrated silica-rich layer. Subsequently Ca^{2+} and HPO_4^{2-} ions diffuse towards the composite surface and as a result a calcium phosphate ceramic is formed via heterogeneous nucleation. The mechanism and sequence of reactions taking place on the bioactive glass surface when in contact with physiological fluids and involved in a apatite layer formation were reported elsewhere [44, 135, 186]. The dissolution of glass ceramic is important since it relates to bioactivity. Nevertheless, it is solution parameters, glass composition, sintering temperature and topography dependent [83, 186].

3.1.6 Morphological and Structural Characterization of GC-PMMA Composites after the Dissolution in SBF

Figure 15 depicts FE-SEM micrographs of the different morphological structures formed on the surface of GC-PMMA composite materials soaked in the SBF solution for 1, 2 and 3 weeks.

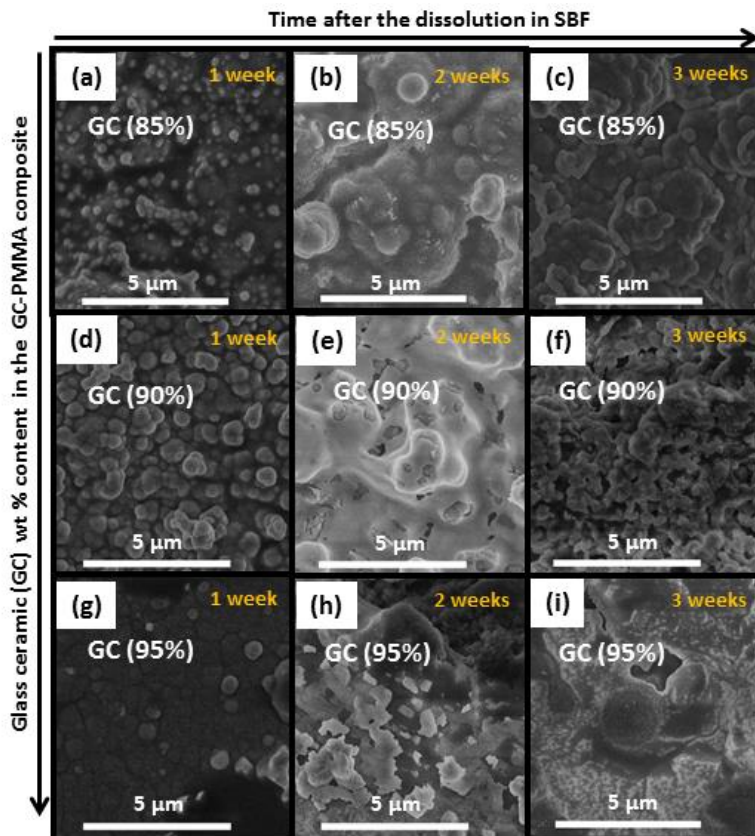


Figure 15. FE-SEM micrographs of the surface of the ((a)-(c)) GC(85%)-PMMA(15%), ((d)-(f)) GC(90%)-PMMA(10%) and ((g)-(i)) GC(95%)-PMMA(5%) composites after 1, 2 and 3 weeks of soaking in SBF.

One can see that the morphological features differ significantly compared to those obtained from as-prepared samples. These changes again indicate the leaching and diffusion processes of ions towards the composite surface, with subsequent formation of ceramic material on the surfaces of all the samples. Microscopic surface cracking was also observed after samples were soaked in SBF solution (Figure 15(a), (d) and (g)). Some cracks were slightly less pronounced when samples were soaked for 3 weeks. This indicates the formation of thicker ceramic component layer on the surface.

EDS analysis showed the elemental composition of newly formed ceramic material on the composite surface after the dissolution. The representative FE-SEM micrographs with EDS-based elemental mapping and EDS spectra of GC(95%)-PMMA(5%) composite before and three weeks after the dissolution are presented in Figure 16.

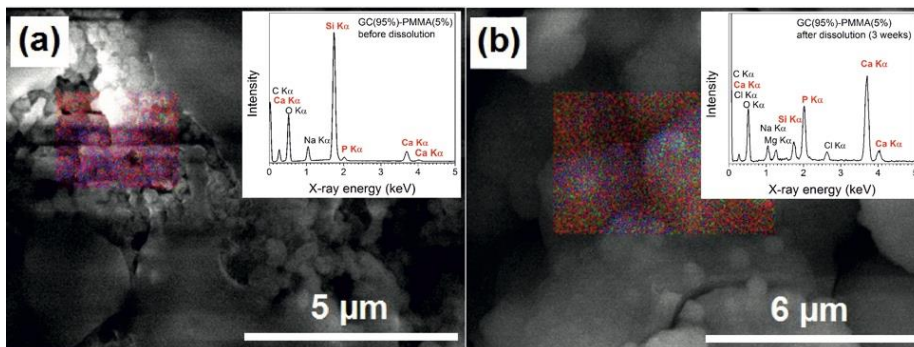


Figure 16. FE-SEM micrographs showing EDS-based elemental mapping and EDS spectra (insets) of GC(95%)-PMMA(5%) composites (a) before dissolution and (b) three weeks after the dissolution in SBF (designated EDS mapping colours: Ca – red, P – green, O – blue).

Elements such as C, O, Na, Mg, Si, P, Cl and Ca were detected and the average atomic per cent (%) ratios of Mg : Si : P : Ca were 2.6 : 4.6 : 11.9 : 19.6. The ceramic composition was similar to that of the HAP with an average Ca : P ratio of 1.65 ($n = 9$). Nonstoichiometric nature of deposited material generally can be explained by the existence of substitutions and vacancies in the crystal lattice of HAP (stoichiometry for HAP Ca/P is 1.67) [187]. Furthermore, the presence of different amorphous apatitic phases might also be present. Raynaud *et al.* demonstrated that HAP with a Ca/P atomic ratio of 1.65 dissociated into a mixture of HAP and β -TCP after heating at 1000 °C [188].

The surface of GC(95%)-PMMA(5%) composite before dissolution contained C, O, Na, Si, P and Ca and the average atomic % ratios of Si : P : Ca were 6.3 : 1.0 : 5.1 (10.95 : 1.2 : 7.8 and 10.88 : 8.62 : 1.09 : 5.72 for GC(90%)-PMMA(10%) and GC(85%)-PMMA(15%) composites, respectively). Based on these observations, we can conclude that the layer rich in calcium and phosphorus has been deposited on the surface of composite materials. The EDS-based mapping were observed over entire samples and showed homogeneous distribution of the P and Ca elements on the surface of composites after the dissolution.

The presence of newly formed ceramic material on the surface of composites was further examined by XRD and FTIR spectroscopy analysis. XRD patterns of GC(95%)-PMMA(5%) composite before and after the dissolution are presented in Figure 17.

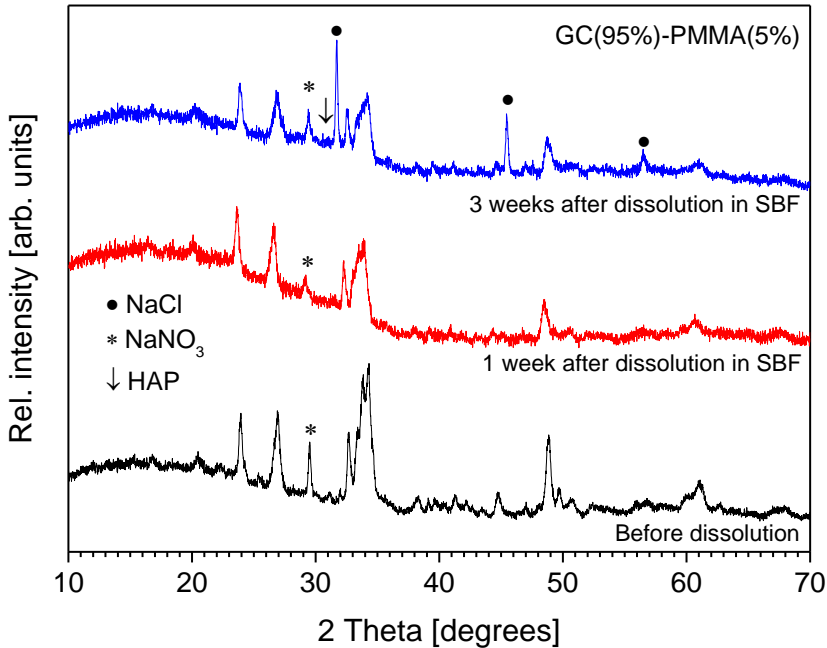


Figure 17. XRD diffractograms of GC(95%)-PMMA(5%) composite surface before and after the dissolution in SBF.

Generally, the poorly crystalline nature of deposited ceramic material is indicated by the broad peaks and low resolution. One can observe that the sharp diffraction peaks of sodium calcium silicate ($\text{Na}_6\text{Ca}_3\text{Si}_6\text{O}_{18}$) [JCPDS no. 77-2189] phase in the XRD pattern are less expressive and broader in comparison to those obtained from composites before dissolution. One shall also note, that intensity of reflections at $2\theta \sim 31.00^\circ$ and 32.50° increased compare to the main reflections of $\text{Na}_6\text{Ca}_3\text{Si}_6\text{O}_{18}$ phase observed at $2\theta = 33-34^\circ$. This result indicate the possible formation of poorly crystalline calcium phosphate after the composites were soaked in SBF solution (the main Bragg peaks characteristic of crystalline HAP arise in the region from 31 to 33θ degrees [JCPDS no. 09-0432] [19]). The rate of cHAP layer deposition was studied by Pereira *et al.* [186]. Furthermore, in the XRD pattern of composite materials three weeks after the dissolution sharp reflections at $2\theta = 31.68^\circ$, 45.42° and 56.50° were obtained and assigned to the NaCl [JCSFD no. 96-900-6375] phase. This result is attributed to the different post-dissolution treatment of the composite samples. It has been reported that to prevent aging of mineralized ceramic, materials are treated in acetone. However, we previously observed (data not reported) that such post-dissolution treatment induces slight demineralization of deposited ceramic and solvent becomes turbid.

Absorption FTIR spectra recorded from the surface of GC(95%)-PMMA(5%) composite material 1, 2 and 3 weeks after the dissolution are presented in Figure 18.

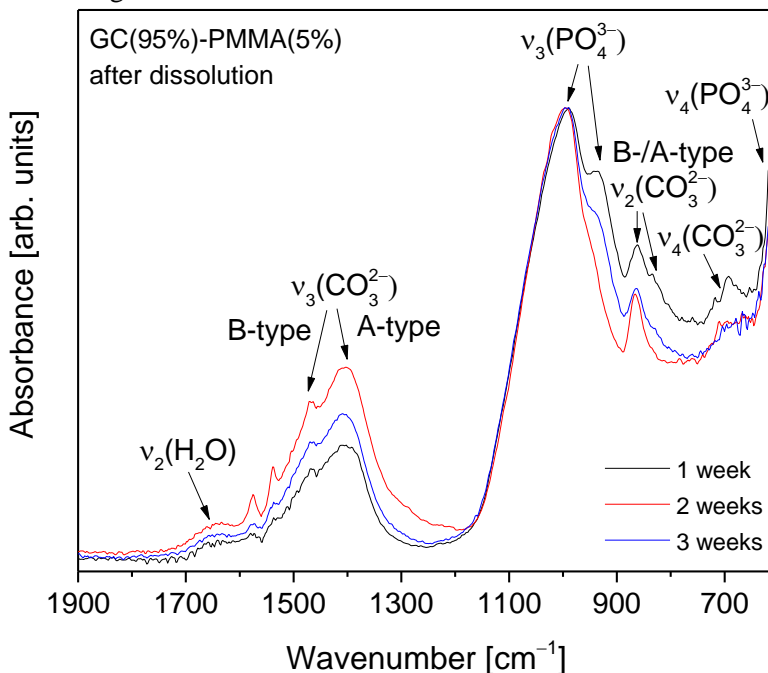


Figure 18. Absorption FTIR spectra recorded from the surface of GC(95%)-PMMA(5%) composites 1, 2 and 3 weeks after the dissolution in SBF.

FTIR spectra show characteristic bands of the phosphate (PO_4^{3-}) and carbonate (CO_3^{2-}) groups and the deposited material was identified as carbonate containing HAP. In the $1100\text{--}900\text{ cm}^{-1}$ region, a broad band with a maximum at 995 cm^{-1} (shoulder at 936 cm^{-1}) was obtained and assigned to the triply degenerate asymmetric stretching mode, ν_3 , of the apatitic PO_4^{3-} groups. It has been previously reported that band obtained at around 600 cm^{-1} indicates a formation of amorphous calcium phosphate phase, while splitting of this band shows the presence of the crystalline phase [174, 175, 187, 189]. In the low wavenumber region of $650\text{--}600\text{ cm}^{-1}$ (maxima at 608 cm^{-1}) obtained bands were attributed to the triply degenerated bending mode, ν_4 , of the O–P–O bonds [19]. A very insignificant splitting of this band indicates the deposition of poorly crystalline calcium phosphate – amorphous material as a major phase with a small presence of crystalline phase [83, 175]. Furthermore, the characteristic bands corresponding to the CO_3^{2-} group were obtained in the $1600\text{--}1350\text{ cm}^{-1}$ interval [19]. This suggests that carbonate group is being incorporated into the deposited ceramic to form cHAP. The

peaks appear for substitutions both in phosphate (B-type carbonate) and OH (A-type carbonate) sites: a band located at 1494 cm^{-1} was assigned to the stretching modes, ν_3 , while the bands at 1454 cm^{-1} and 1436 cm^{-1} to the bending modes, ν_4 or ν_3 , of C–O bond [76, 187]. In the lower wavenumber region a band arising from the bending mode, ν_2 , of C–O bond (CO_3^{2-} group) was observed at $\sim 865\text{ cm}^{-1}$ and assigned to the A-type substitution, while broad band $\sim 700\text{ cm}^{-1}$ was designated to the in-plane band, ν_4 , CO_3^{2-} group. In another work by Pereira *et al.* the formation of cHAP on the surface of sol-gel derived bioglass surfaces *in vitro* has been demonstrated [175].

It is known that HAP is thermodynamically the most stable phase in physiological conditions and has the ability for direct chemical bonding to the bone. However, previous studies have shown that mechanism of bone apatite formation involves metastable intermediate products including amorphous calcium phosphate [190]. This indicates the favourable transformation of deposited low crystallinity calcium phosphate into the crystalline hydroxyapatite. GC(90%)-PMMA(10%) and GC(85%)-PMMA(15%) (ESI Fig. S3) composites exhibited very similar spectral features showing the formation of A- and B-substituted carbonated apatite under identical experimental conditions.

Although we can conclude that in the current work the inorganic-organic composites were successfully prepared and the growth of low crystallinity carbonated HAP on the surface of composites immersed into SBF under static conditions was obtained, the studies examining the effect of the observed surface morphology on cell behaviour *in vitro* and *in vivo* still has to be performed and will be a subject of further studies.

3.2 Porous cHAP-Acrylate Composites Prepared Using Dipentaerythritol Hexaacrylate (Miramer M600) and Gelatin

In this part we report preparation of hybrid inorganic-organic composites. Scaffolds were prepared using a different amounts of gelatin which serves as a porosity forming agent.

3.2.1 Structural Evaluation of cHAP

The XRD pattern of Ca-P-O gel powders annealed at $800\text{ }^\circ\text{C}$ presented in Figure 19, show that powders produced at $800\text{ }^\circ\text{C}$ are already crystalline with well resolved diffraction peaks from the Bragg diffraction conditions for HAP [PDF# 00-3553] (hexagonal crystal system, space group of $P6_3/m$).

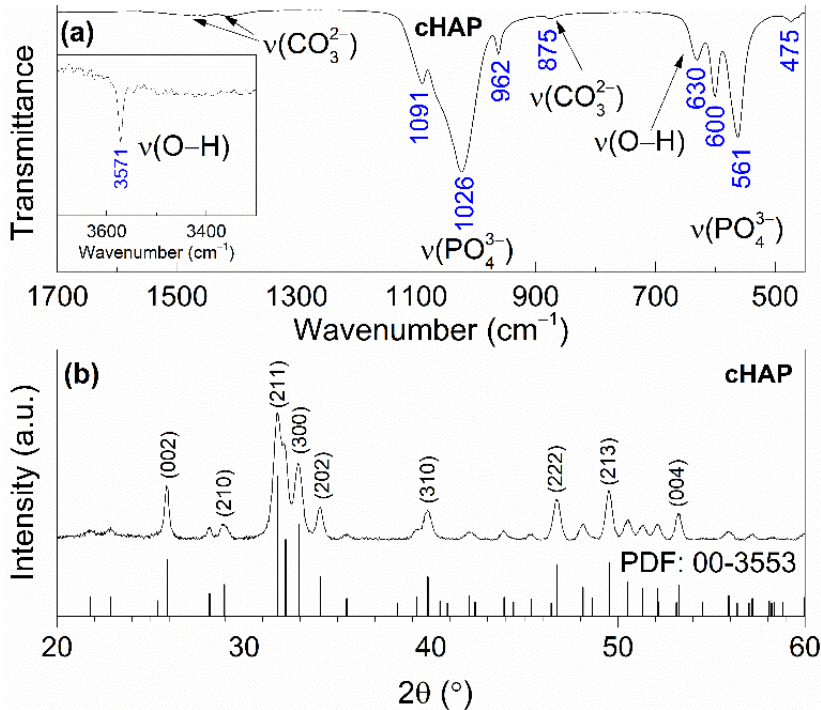


Figure 19. FT-IR spectrum (a) and XRD pattern (b) of cHAP powders calcined at 800 °C.

The FT-IR spectrum of cHAP calcined at 800 °C, presented in Figure 19, shows the characteristic bands of phosphate (PO_4^{3-}) and carbonate (CO_3^{2-}) groups. The absorption bands between 1200 and 900 cm^{-1} are due to the triple degenerated asymmetric stretching mode ν_3 , and the symmetric stretching mode ν_1 of the P–O bonds, while bands between 630 and 450 cm^{-1} are due to the triple degenerated bending mode ν_4 of the O–P–O of apatitic PO_4^{3-} groups. Bands in the 1550–1360 cm^{-1} region are characteristic of CO_3^{2-} groups in the cHAP [76, 191, 192]. The band at 875 cm^{-1} can be attributed to the CO_3^{2-} group substituted for the PO_4^{3-} group (type B carbonate apatite) [193]. Two distinctive peaks observed at 3571 and 630 cm^{-1} were assigned to the stretching mode ν_s and vibrational mode ν_L respectively of the structural hydroxyl anion (OH^-) in cHAP. Carbonate ions can substitute a hydroxide (OH^-) or phosphate (PO_4^{3-}) group in the HAP ($\text{Ca}_{10}(\text{PO}_4)_6(\text{OH})_2$) crystal lattice, leading respectively to A- or B-type carbonated apatites. Biological apatite is considered to be an AB carbonate-substituted apatite [30]. Studies have shown that cHAP is more soluble *in vivo* than pure HAP [29, 193], that it promote cell proliferation [194], and that it is therefore likely to lead to an

increase in the biological response of the bone mineral while in contact with a cHAP-based scaffold.

In addition, Rietveld analysis was performed. The calculated lattice parameters ($a = 9.4227(8) \text{ \AA}$ and $c = 6.8843(6) \text{ \AA}$) agree with to the parameters found in literature for HAP [192]. Rietveld refinement for XRD pattern (Figure 20) showed the elongation of reflection at $2\theta = 25.8^\circ$ for (002) indicating possible elongation of crystals along the $\langle 002 \rangle$ plane.

This is in agreement with our previous study where cHAP crystals produced from solutions containing polyethylene glycol exhibited slight lengthening compare to those produced from polyvinyl alcohol. [76] The average crystallite size was estimated to be $32 \pm 5 \text{ nm}$. Small crystal sizes are linked to the relatively high solubility of biological apatites with respect to stoichiometric HAP [30], which probably alters the nanoscale surface structure, increasing the surface area and surface wettability of the scaffold, offering favourable conditions for cell adhesion.

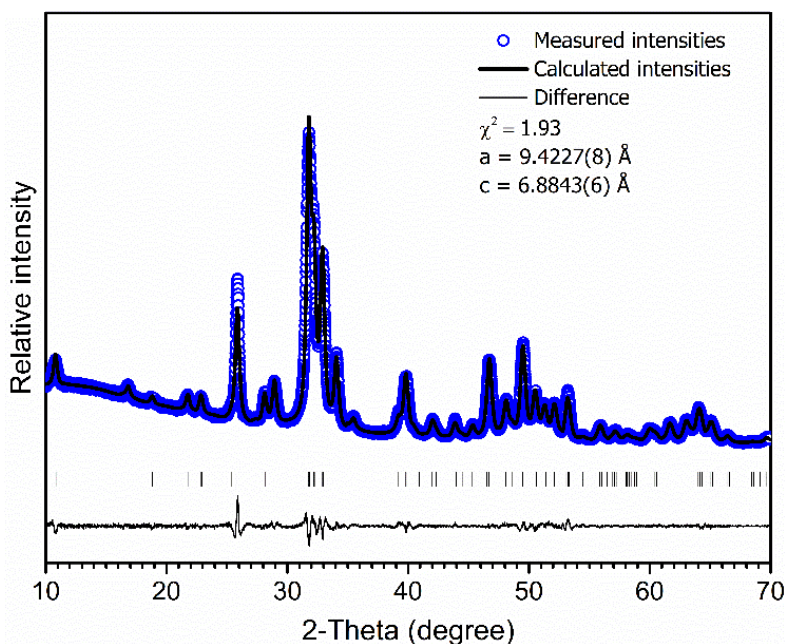


Figure 20. Rietveld fit to cHAP powders XRD data. Experimental (o) and calculated (–) patterns are shown along with the difference curve (–) and (i) Bragg positions.

Raman spectrum of cHAP powders annealed at $800 \text{ }^\circ\text{C}$ is presented in Figure 21. Characteristic vibrations of the PO_4^{3-} group appears in $1100\text{--}1000 \text{ cm}^{-1}$ region and at 964 cm^{-1} (the most intense band), 587 cm^{-1} and

430 cm^{-1} . These bands were attributed to the $n_3(\text{PO}_4^{3-})$, $n_1(\text{PO}_4^{3-})$, $n_4(\text{PO}_4^{3-})$ and $n_2(\text{PO}_4^{3-})$ modes, respectively [19, 195, 196]. The carbonate band in the Raman spectrum appears at 1070 cm^{-1} ; it is quite weak and overlaps with bands of the phosphate group (Figure 21 (inset)) [195].

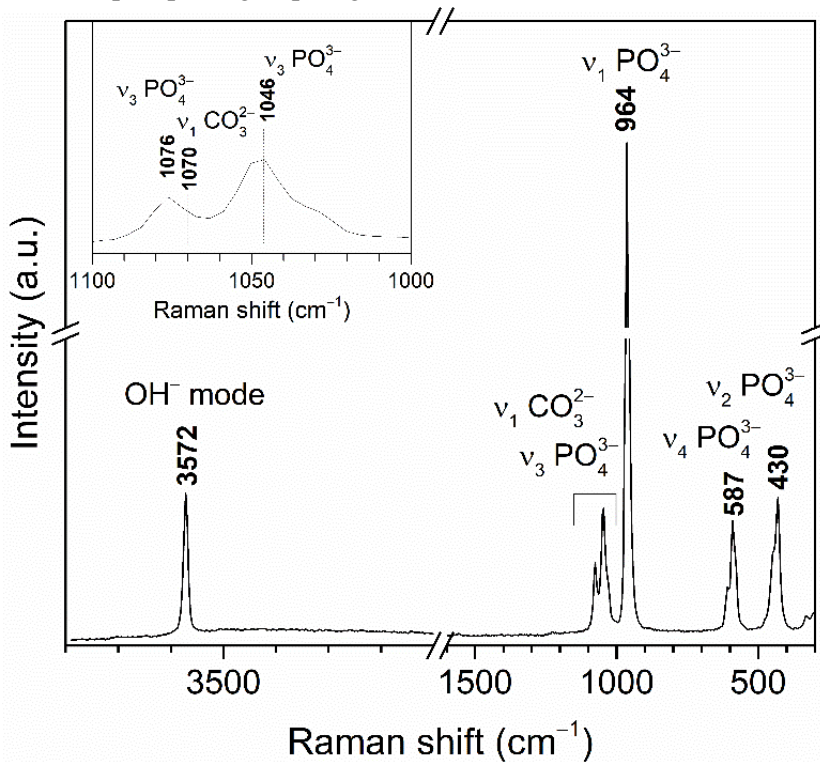


Figure 21. Raman spectrum of cHAP powders calcined at 800 °C (inset: enlarged spectrum region of overlapping PO_4^{3-} and CO_3^{2-} -bands).

Furthermore, obtained small band at 326 cm^{-1} can be assigned to the $n_4(\text{Ca-OH})$ mode [196]. Spectrum also shows the band located at 3572 cm^{-1} that was assigned to the stretching vibrations of the O–H group. The Raman spectrum agrees with the literature and the absence of a splitting in the most intense PO_4^{3-} band indicates a homogeneous carbonate incorporation into the HAP lattice.

3.2.2 Morphological Evaluation of Formed Acrylate-Gelatin-cHAP Composites

FE-SEM images of the acrylate-gelatin-cHAP composites are shown in Figure 22. One can observe that the cHAP particles are homogeneously imbedded in the continuous polymeric matrix. Voids and large agglomerate

blocks were also observed on parts of the composite pellets.

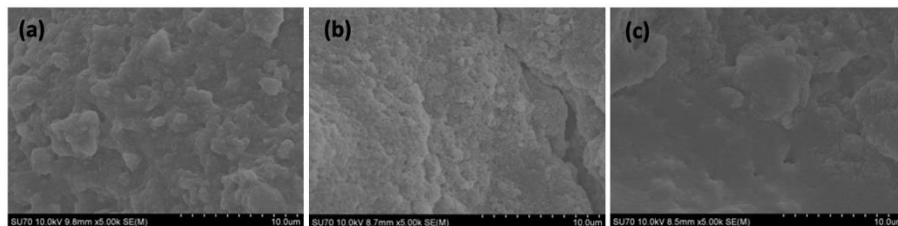


Figure 22. FE-SEM images showing surface morphology of acrylate-gelatin–cHAP composite scaffolds: (a) 50/50, (b) 75/25, and (c) 95/5.

The cHAP-acrylate(50%)-gelatin(50%) composites exhibited a slightly rougher surface, possibly due to the higher cHAP concentration. Figure 23 shows SEM images and corresponding EDS spectra of the multi-composites.

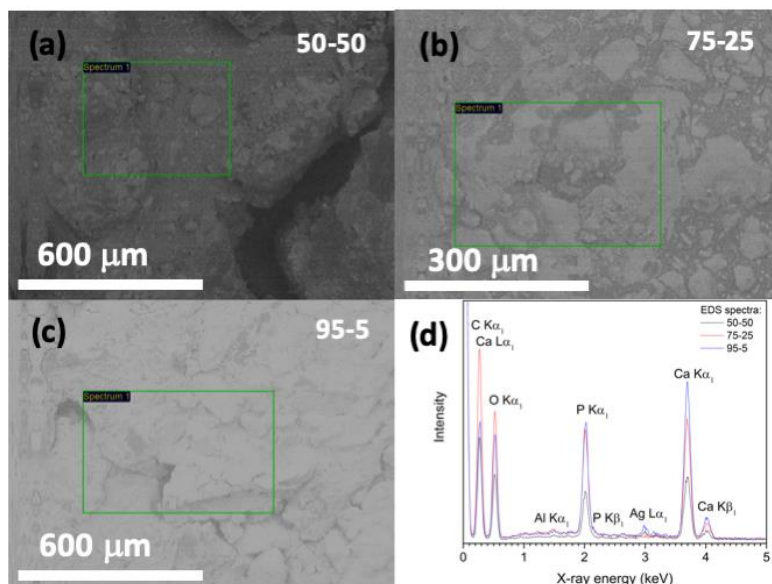


Figure 23. ((a)-(c)) SEM images (marked places show the surface regions examined) and (d) EDS spectra of acrylate-gelatin–cHAP composite scaffolds.

The 50/50 composite shows voids with a width of 300 µm. Elements C, O, P and Ca were detected. Al and Ag were also detected, but these were due to the sample holder and pre-sputtering, respectively. The average atomic% ratio of Ca/P was calculated to be 1.6 (n = 11) and place dependency was revealed. In the nonstoichiometric apatites, the Ca/P ratio depends on the ionic substitution in the crystal lattice. That is, when PO_4^{3-} ions are replaced by

CO₃²⁻ ions (B-substitution), the Ca/P ratio is larger than that of stoichiometric HAP, and when OH⁻ ions in the apatite structure are replaced by CO₃²⁻ ions (A-type substitution) or HPO₄³⁻ ions replace PO₄³⁻ the Ca/P ratio tends to be smaller than 1.67 [76, 197]. Other composites exhibited similar morphological features.

The presence of prominent components within the multi-composite scaffolds was confirmed by FTIR spectroscopy, where the IR spectrum of the representative acrylate(75%)-gelatin(25%)-cHAP composite scaffold, shown in Figure 24, exhibits characteristic bands assigned to acrylate, cHAP and gelatin. The absorption bands at 1089, 1024, 962 and 629 cm⁻¹ were assigned to the cHAP. The spectral features of the apatite do not appear to have changed after it was incorporated into the polymeric matrix. The spectrum of the multi-composite also shows a wide band in the 1730-1700 cm⁻¹ region which can be ascribed to the carbonyl (C=O) group stretching vibrations of acrylate [198, 199]. The important peaks for C=C deformation of the acrylate group appear at 1636, 1408 and 809 cm⁻¹, and this indicates that some residual C=C bonds remain inside the network structure.

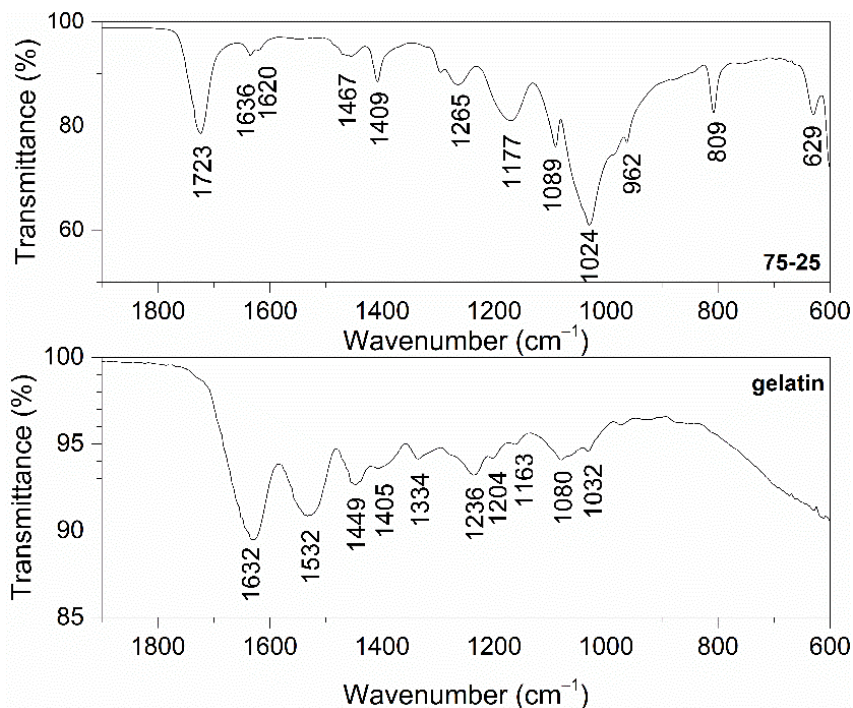


Figure 24. FT-IR spectra of the acrylate-gelatin(75%)-cHAP(25%) composite and neat gelatin powders.

The copolymerization of DPHA and EGDMA monomers under UV irradiation is a free radical chain growth cross-linking reaction that is diffusion-controlled. The molar ratios of C=C bonds in the different monomers, the concentration of initiator, the curing times, and the reaction temperatures affect the reaction kinetics and products. Although the formation of a cross-linked structure reduces the termination rate of free radicals, it also reduces the diffusion of reactants in the later stages of the reaction, so the final conversion is limited [200]. The relative intensities of the 1636 cm^{-1} (C=C stretching) and 1723 cm^{-1} (C=O stretching) peaks nevertheless indicate that the monomers were consumed during curing and that a highly crosslinked network was created. The simplified intermolecular cross-linking of monomers DPHA and EGDMA under UV irradiation is shown in Figure 25.

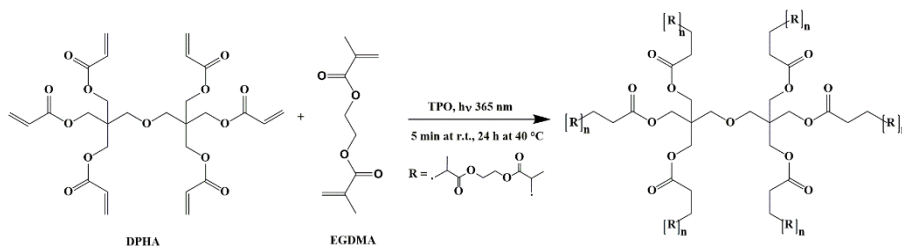


Figure 25. Simplified intermolecular cross-linkage of monomers DPHA and EGDMA under UV irradiation.

3.2.3 Computed Tomography Studies of cHAP-Acrylate Composites

Computed tomography (CT) was used to assess the density of the scaffolds. The cross-sectional CT images of acrylate-gelatin-cHAP scaffolds (scan performed at 80 kV) presented in Figure 26 (inset: camera photos of scaffolds) shows that the scaffolds with different compositions had different densities.

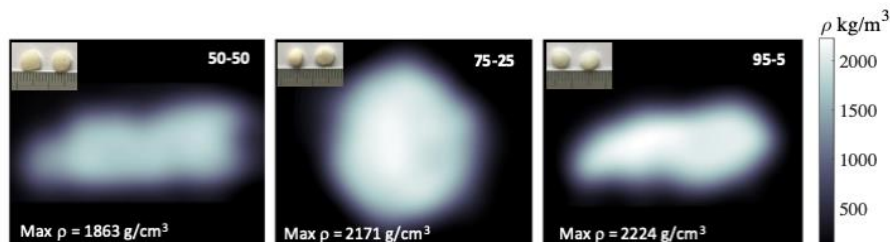


Figure 26. Cross-sectional CT images of the acrylate-gelatin-cHAP composites and the calculated density (inset: photographs of composites placed on the ruler, scale: 1 bar = 1 mm). The 50/50 and 95/5 composites were scanned in the radial

direction and the 75/5 composite in the axial direction (X-ray beam energy of 80 kV).

The average density was calculated to be 1863, 2171 and 2224 kg/m³ for the 50/50, 75/25 and 95/5 composite scaffolds, respectively. The difference in density is mainly due to a difference in material composition, but the density varied slightly within the specimen, the material density being higher in the central region than in the outer layer. The density values of the multi-composites were not changed when scan was performed at 110 kV. A number of bone-scaffold features affect scaffold resorption, cell penetration and the ingrowth of new bone [136, 201, 202]. Since the porosity of the material is related to its density, the rate of dissolution of surface components, the formation of voids within the scaffold, and the penetration of liquid phase into the inner layers of the composite can be predicted. Thus, the 50/50 multi-composite scaffolds probably have the fastest degradation and the greatest formation of voids within the scaffold when it is in contact with a liquid phase. Due to the higher atomic numbers of the elements, the ceramic material attenuates the X-ray beam more than the acrylate/gelatin matrix, but the internal microstructure of the composites was not resolved due to the lower resolution of the medical CT scanner compared to that of other (micro- and nano-) CT devices [203]. Extensive studies have demonstrated the micro-CT can reveal bone tissue density as well as new bone formation throughout the depth of the scaffolds, [153-155, 204] although the use of contrast agents or a complementary technique such as MRI may be needed [205].

To obtain more complete characterization in assessing inner architecture of scaffolds, a cone beam computed tomography (CBCT) analysis was performed. Figure 27(a) shows CBCT image of 50/50, 75/25 and 95/5 composites as well as segmented images (6 of total 24) of multiple projections of the 95/5 composite.

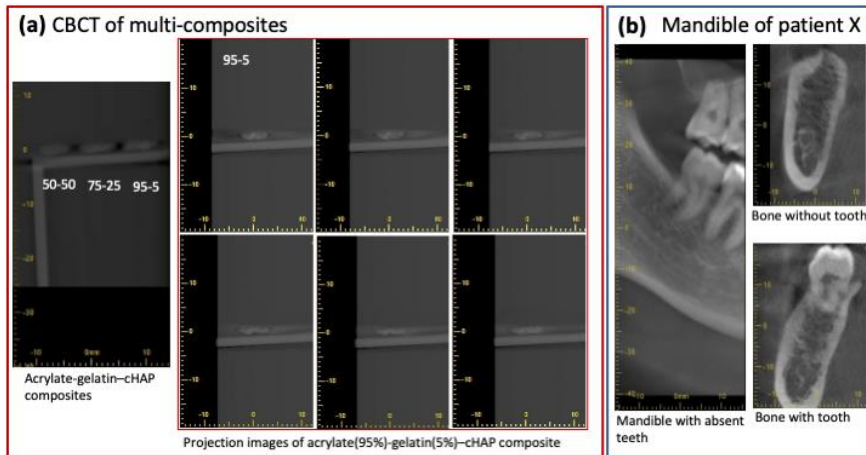


Figure 27. CBCT images of (a) acrylate-gelatin-cHAP composites and traversing images (6 of total 24) of multiple projections of the 95/5 composite, (b) orofacial region of patient X showing radiographic contrast between different bone tissues (CBCT was performed under the same conditions to compare the radiographic contrast).

Data demonstrate that radiographic contrast of the images is higher. Composite, although mostly radiolucent, it also contains apatite particles that are radiopaque. Some fogging in the images of the composites is also present and this was attributed to the scattered X-ray radiation. To compare a subject contrast, the mandible (lower jaw) images of patient X are presented in Figure 27(b). These intraoral CBCT images were taken under the same conditions as fabricated scaffolds. Comparison of images show that dental bone exhibits higher contrast indicating that fabricated multi-composites could be more easily distinguished after the implantation while observing anatomic structures of interest.

To further evaluate structural features of the scaffolds, conventional dental radiography was used, as shown in Figure 28 which presents a radiographic image of a representative acrylate(75%)-gelatin(25%)-cHAP scaffold.

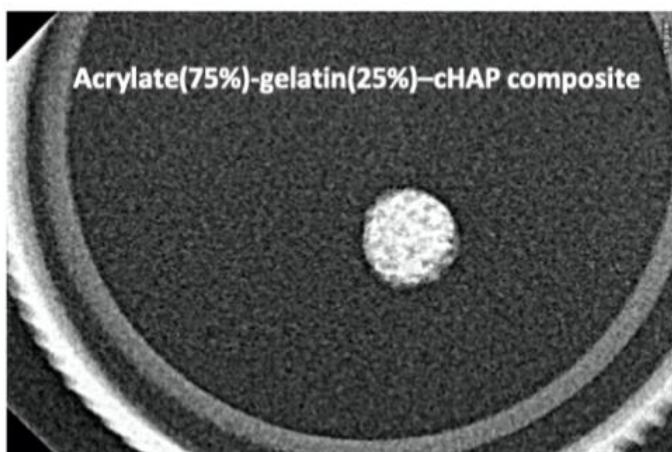


Figure 28. X-ray radiograph of the representative acrylic(75%)-gelatin(25%)-cHAP composite scaffold showing the distribution of cHAP (brighter places) within the organic matrix.

Composite is as a restorative material and their radiographic appearance vary depending on their thickness, density, and atomic number. Due to its higher radiological density compared to that of the organic matrix, the apatitic phase is clearly visible with a homogeneous distribution of the cHAP over the entire scaffold. This indicates the possibilities of achieving radiographic differentiation between the bone tissue and the restorative scaffold and of evaluating structural changes when it is replaced by de novo bone [206, 207].

3.2.4 Surface Hydrophilicity Evaluation of cHAP- Acrylate Composite

The wettability of the scaffolds was assessed by measuring the contact angle of water tinted with methylene blue dye which is frequently used as a cationic stain to examine cytological specimens [145, 207]. The sessile drop contact angles are presented as function of time in Figure 29.

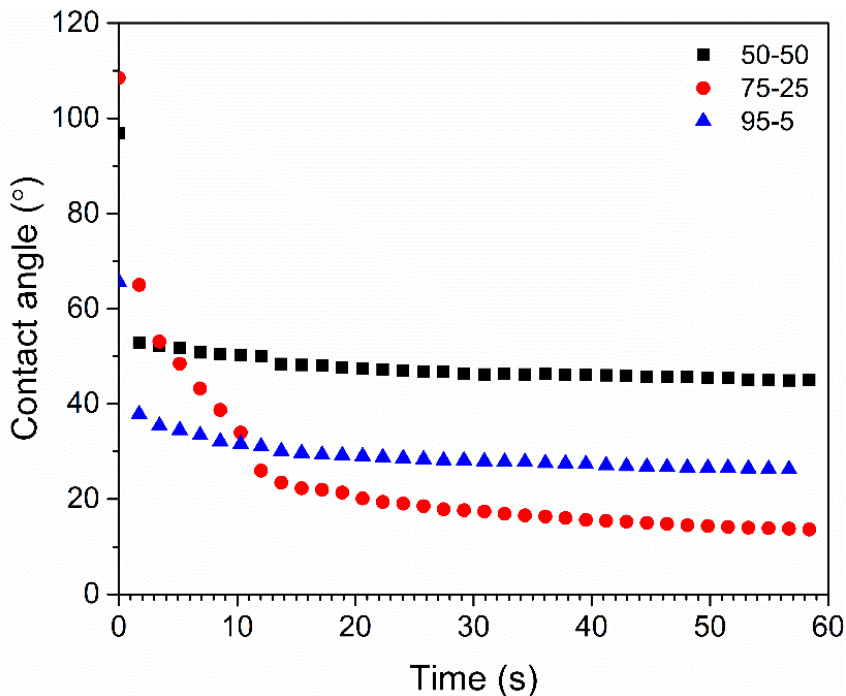


Figure 29. Contact angles vs. time (sessile drop of water tinted with methylene blue dye) on acrylate-gelatin–cHAP composite scaffolds (values of the first measurement are presented).

Within a few seconds, the contact angle on all the scaffolds decreased by 15–20° (initial average angles of 91°, 100° and 67° were measured for the 50/50, 75/25 and 95/5 composites, respectively ($n = 3$)). The angle then gradually decreased more slowly until it reached a plateau. The final values after 60 seconds were 47.6° and 31.4° for the 50/50 and 95/5 composites, respectively. The 75/5 composite however exhibited a slightly different behaviour. After the initial decrease, the contact angle decreased relatively rapidly from 63.4° to 21.5° (within 15 sec) and then continued to decline until the final angle after 50 seconds was found to be 16.6°, indicating that this was the most hydrophilic surface investigated. These differences in the contact angle were attributed to differences in surface morphology (Figures 23 and 24) which depend on the composition. The surface characteristics, such as the porosity (pore diameter, interconnectedness, pore orientation), roughness and topography as well as chemistry (element present, presence of polar/non-polar group, acid-base characteristics, dangling bonds), have a great effect on the hydrophilicity and subsequently bioactivity [208, 209].

The rates of degradation of DPHA, EGDMA and gelatin differ, and the combination of DPHA/EGDMA, gelatin and cHAP in bone tissue engineering

can therefore provide some advantages, as the composites may degrade faster than a pure acrylate-based polymer matrix. The hydrophilicity of the bioceramic and gelatin should enable water to penetrate more easily into the acrylate-based matrix and thus promote hydrolytic degradation where scaffolds and body fluids interact, and the microstructural architecture of the scaffold could enhance the mineralization of new bone in the interior of the composite material and allow deeper tissue ingrowth.

3.3 Porous Carbonated Hydroxyapatite (cHAP)-Poly(ethylene glycol) Diacrylate (PEGDA) Composite Prepared Using Foaming Agent Azodicarbonamide (ADCA)

Herein the characterization of porous cHAP-PEGDA composites prepared at the temperature range of 180-200°C, their fabrication is described in 3.1.2 section, using gas chromatography (GC), differential scanning calorimetry (DSC), optical microscopy and computed tomography analysis. Hydrophilicity of porous formed scaffolds was further elucidated studying sorption of water dyed with Methylene Blue dye.

3.3.1 Purity of cHAP-PEGDA Evaluation Using Chromatography and DSC

To estimate residual monomers in cHAP-PEGDA samples, gas chromatography (GC) analysis was performed. As it is seen in Figure 30 there is no residue of polyethylene glycol diacrylate nor ethylene glycol dimethacrylate in cHAP-PEGDA material (chromatogram of red colour) compared to the reference sample (chromatogram of black colour).

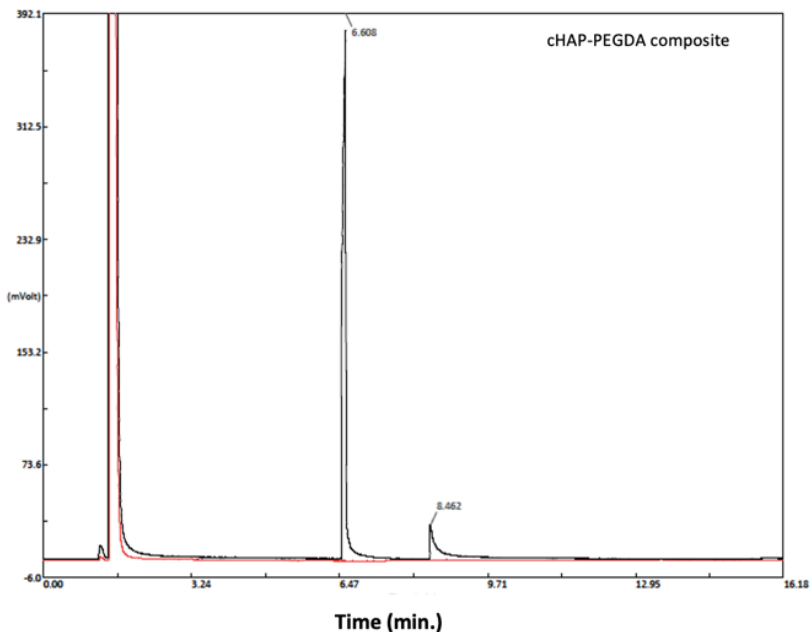


Figure 30. GC curves of cHAP-PEGDA composite (red line) and reference mixture of PEGDA and EGDMA (black line) showing no left residual of monomers within formed composite.

However further evaluation of the composites has shown the residues of foaming agent azodicarbonamide, and this was confirmed by differential scanning calorimetry analysis. DSC curves (Figure 31) of the representative cHAP-PEGDA composite show the exothermic event in the temperature range of 200-240 °C and this was attributed to the energy release due to the ADCA residual within the material left after incomplete copolymerization. Figure 32 shows DSC curves of ADCA and cHAP-PEGDA composite. The exothermic peaks with the maxima at 223 °C and 214 °C were observed for ADCA and cHAP-PEGDA composite, respectively. Results indicate that processing of such hybrid composites shall be altered in order to prepare pure and completely cross-linked polymeric composite material.

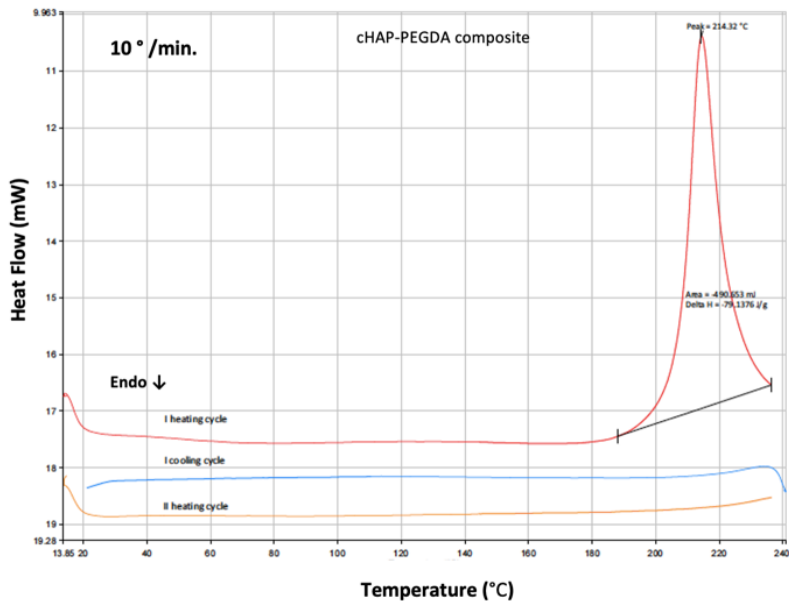


Figure 31. DSC curves of cHAP-PEGDA composite showing exothermic event due to ADCA residual.

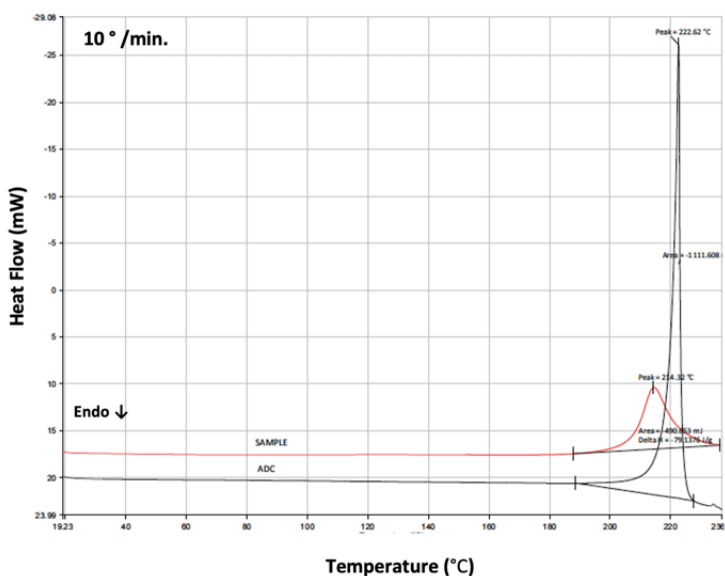


Figure 32. DSC curves of ADCA (black line) and cHAP-PEGDA composite (red line) showing a residual of ADCA within prepared composite.

3.3.2 Density and Morphology Evaluation of cHAP-PEGDA Composites

CT image of the representative cHAP-PEGDA composite is presented in Figure 33. The difference in density observed within entire scaffold was attributed to the foaming agent ADCA and processing conditions.

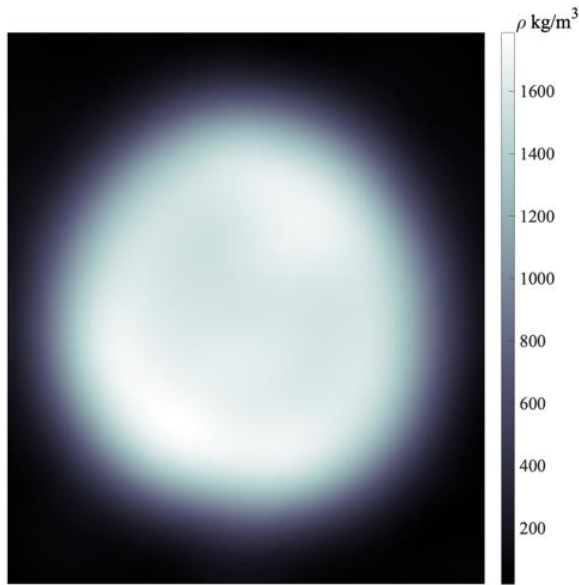


Figure 33. Cross-sectional CT image of the representative cHAP-PEGDA composite showing different contrast within entire composite (composite was scanned using X-ray beam energy of 80 kV).

Optical microscopy images of the representative cHAP-PEGDA composite is presented in Figure 34.



Figure 34. Optical microscopy showing surface morphology and microporous structure of the representative cHAP-PEGDA composite.

Images further confirmed the microporosity of the scaffolds suggesting better diffusivity of liquid phase into the internal part of the scaffold.

3.3.3 Studies of Methylene Blue (Toluidine Blue) Dye Absorption on Low Crystallinity cHAP-PEGDA

The dye absorption was used to confirm hydrophilicity and absorption of the liquid phase by the scaffold material. The images of the representative cHAP-PEGDA composites before and after the dye absorption are shown in Figure 35.

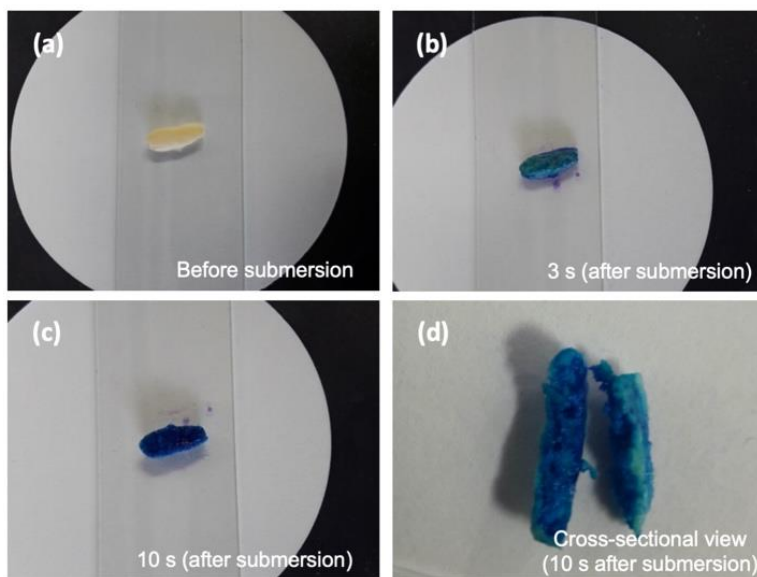


Figure 35. cHAP-PEGDA composite scaffold (a) before submersion and after submersion into Methylene blue dye (b) 3 s, ((c) and (d)) 10 s ((d) shows cross sectional-view of composite scaffold and porous structure).

Absorption changes on the scaffold surface using 0.05% aqueous solution of Toluidine Blue dye were observed after 1, 3, 5 and 10 s. The permeability of drop was observed and this was related to the porous structure of the scaffold. Cross-sectioned image of the scaffold (Figure 35(d)) confirmed the hollow structure of the fabricated scaffold. Overall results indicate that ADCA is well suited to form scaffolds with porous structure.

4. CONCLUSIONS

1. Proposed aqueous wet-chemistry approach with subsequent annealing steps is suitable to prepare low crystallinity carbonated HAP and glass-ceramic (Na-Ca-Si-O) powders.

2. Homogeneous hybrid composites consisting of glass-ceramic and polymethyl methacrylate (GC(85%)–PMMA(15%), GC(90%)–PMMA(10%), GC(95%)–PMMA(5%)) were successfully prepared via photopolymerization reaction.

3. It was determined that the mechanical compressive strength for GC–PMMA composites was in the range of 42.5–49.6 MPa, with GC(90%)–PMMA(10%) composites exhibiting the highest strength and lowest density.

4. The dissolution of glass-ceramic phase within GC–PMMA composites was confirmed by ICP-OES indicating the fastest degradation of GC(90%)–PMMA(10%) composites in SBF, and XRD and SEM/EDS analyses revealed that the alteration products are mostly amorphous material with the composition similar to that of the HAP (average atomic % ratio of Ca/P = 1.65). Moreover, FTIR analysis showed that the ceramic layer formed after the dissolution is low crystallinity calcium phosphate with crystalline phase attributed to carbonate A- and B- substituted HAP.

5. Proposed copolymerization reactions are suitable to prepare hydrophilic multi-composites consisting of acrylate (DPHA/EGDMA), cHAP and gelatin as well as highly porous cHAP-PEGDA composites when ADCA is used as a foaming agent.

6. Morphological studies revealed that cHAP particles were homogeneously imbedded within the continuous polymeric matrix, and that the scaffolds possessed voids and large agglomerate blocks in different parts of the composite pellets. Moreover, TG analysis confirmed that the residual inorganic material mass corresponded well with the initial quantity of cHAP.

7. FTIR analysis revealed the presence of prominent components within the multi-composite (acrylate-cHAP-gelatin) scaffolds, and that some residual C=C bonds remain inside the network structure after the copolymerization of DPHA and EGDMA monomers under UV irradiation.

8. CT analysis showed that the acrylate-cHAP-gelatin scaffolds had differing average densities and that the scaffolds had a higher density in the central region than in the outer layer. CBCT analysis revealed that dental bone exhibits higher radiographic contrast than fabricated multi-composites, and so indicate easier identification after the implantation while observing anatomic structures of interest. Moreover, conventional radiography images further

validated cHAP, exhibiting higher radiographic density compared to organic matrix, and homogeneous distribution within the entire scaffold.

9. Contact angle measurements revealed that the hydrophilicity was composition- and morphology-dependent, the greatest wettability of 16.6° being on the acrylate(75%)-gelatin(25%)-cHAP composite scaffold, indicating potential in porosity and hydrophilicity remodelling strategies, and subsequently promote scaffold-implant integration.

10. Results overall indicate that prepared and studied composites, GC-PMMA and lc-cHAP-PEGDA, have potential for bone tissue engineering applications.

5. LIST OF PUBLICATIONS

1. RSC Advances (PDF)
2. Materials Advances (PDF)

5.1 Articles in Journals

1. Fabrication and investigation of high-quality glass-ceramic (GC)–polymethyl methacrylate (PMMA) composite for regenerative medicine.

Golubevas, Ričardas; Žarkov, Aleksej; Alinauskas, Laurynas; Stankevičiūtė, Živilė; Balčiūnas, Giedrius; Garškaitė, Edita; Kareiva, Aivaras

Laisvai prieinamas internete / Unrestricted. ISSN: 2046-2069; DOI: 10.1039/c7ra05188c

RSC advances. Cambridge : Royal Society of Chemistry. 2017, Vol. 7, iss. 53, p. 33558-33567.

2. Acrylate-gelatin–carbonated hydroxyapatite(cHAP) composites for dental bone-tissue applications.

Golubevas, Ričardas; Stankevičiūtė, Živilė; Žarkov, Aleksej; Golubevas, Raimundas; Hansson, Lars; Raudonis, Rimantas; Kareiva, Aivaras; Garškaitė, Edita.

Laisvai prieinamas internete / Unrestricted. eISSN: 2633-5409; DOI: 10.1039/D0MA00498G

Materials advances. London : The Royal Society of Chemistry. 2020, vol. 1, no. 6, p. 1675-1684.

This article is part of the themed collections: Materials Advances HOT Article Collection and International Open Access Week 2020.

5.2 Attended Conferences

1. Preparation and characterization of the inorganic-organic (bioglass-poly(methyl methacrylate)) composite for bone tissue engineering.

Golubevas, Ričardas; Žarkov, Aleksej; Gražėnaitė, Eglė; Alinauskas, Laurynas; Garškaitė, Edita; Kareiva, Aivaras

ISSN: 1822-7759

Advanced materials and technologies : book of abstracts of the 18th international conference-school, 27-31 August 2016, Palanga, Lithuania. Kaunas: Technologija. 2016.

2. Preparation and Characterization of the Inorganic-Organic (Bioglass-Poly (Methyl Methacrylate) Composite for Bone Tissue Engineering.

There is no future without the past“ : science on the interface of XIX-XXI centuries : the international conference dedicated to the 215-th birth anniversary of Ignacy Domeyko : proceedings book, Vilnius, 2017. Vilnius : Vilniaus universiteto leidykla, 2017.

3. Investigation of high-quality glass-ceramic (GC) and polymerized methyl methacrylate (PMMA) composite for regenerative medicine.

R. Golubevas , A. Zarkov, Z. Stankeviciute, L. Alinauskas, E. Garskaite, A. Kareiva

Dalyvavimas tarptautinėje konferencijoje-mokykloje „Šiuolaikinės medžiagos ir technologijos 2018“

20 – oji tarptaurinė konferencija – mokykla, Rugpjūčio 27-31, 2018, Palanga, Lithuania. Kaunas : Technologija. 2018.

4. Preparation of porous glass–ceramic (gc) and polymerized 1,6-hexanediol diacrylate (hdda) composite using free radical copolymer crosslink reactions and blowing agent for bone tissue engineering.

Golubevas, Ričardas; Žarkov, Aleksej; Alinauskas, Laurynas; Kareiva, Aivaras; Garškaitė, Edita

EcoBalt 2018 : the international conference proceedings book, October 25-27, 2018, Vilnius, Lithuania. Vilnius : [Vilniaus universitetas]. 2018.

REFERENCES

1. *Calcium-phosphate-based composites*, in *Biological Materials Science: Biological Materials, Bioinspired Materials, and Biomaterials*, M.A. Meyers and P.-Y. Chen, Editors. 2014, Cambridge University Press: Cambridge. p. 223-291.
2. Bakheet, M., et al., *First principles study of the physical properties of pure and doped calcium phosphate biomaterial for tissue engineering*. 2016. p. 215-240.
3. Polo-Corrales, L., M. Latorre-Esteves, and J.E. Ramirez-Vick, *Scaffold design for bone regeneration*. Journal of nanoscience and nanotechnology, 2014. **14**(1): p. 15-56.
4. Yan, L.-P., et al., *Current Concepts and Challenges in Osteochondral Tissue Engineering and Regenerative Medicine*. ACS Biomaterials Science & Engineering, 2015. **1**(4): p. 183-200.
5. Stevens, M.M., *Biomaterials for bone tissue engineering*. Materials Today, 2008. **11**(5): p. 18-25.
6. Rezwani, K., et al., *Biodegradable and bioactive porous polymer/inorganic composite scaffolds for bone tissue engineering*. Biomaterials, 2006. **27**(18): p. 3413-3431.
7. Du, Y., et al., *Hierarchically designed bone scaffolds: From internal cues to external stimuli*. Biomaterials, 2019. **218**: p. 119334.
8. Conrad, B., C. Hayashi, and F. Yang, *Gelatin-Based Microribbon Hydrogels Support Robust MSC Osteogenesis across a Broad Range of Stiffness*. ACS Biomaterials Science & Engineering, 2020.
9. Gentleman, E., M.D. Ball, and M.M. Stevens, *Biomaterials*. In: *Medical Sciences. Encyclopedia of Life Support Systems (EOLSS)*. 2009: p. pp. 43-86.
10. Vuluga, Z., et al., *Collagen - Modified Layered Silicate Biomaterials for Regenerative Medicine of Bone Tissue*. In: Hutagalung, S. (Ed.), *Materials Science and Technology*. InTech, 2012: p. pp. 125–148.
11. Jones, J.R. and I.R. Gibson, *1.3.4 - Ceramics, Glasses, and Glass-Ceramics: Basic Principles*, in *Biomaterials Science (Fourth Edition)*, W.R. Wagner, et al., Editors. 2020, Academic Press. p. 289-305.
12. Canillas, M., et al., *Calcium phosphates for biomedical applications*. Boletín de la Sociedad Española de Cerámica y Vidrio, 2017. **56**(3): p. 91-112.
13. Habraken, W., et al., *Calcium phosphates in biomedical applications: materials for the future?* Materials Today, 2016. **19**(2): p. 69-87.

14. Huang, J., *Chapter 20 - Design and Development of Ceramics and Glasses*, in *Biology and Engineering of Stem Cell Niches*, A. Vishwakarma and J.M. Karp, Editors. 2017, Academic Press: Boston. p. 315-329.
15. Szcześ, A., L. Hołysz, and E. Chibowski, *Synthesis of hydroxyapatite for biomedical applications*. *Advances in Colloid and Interface Science*, 2017. 249: p. 321-330.
16. Dorozhkin, S.V., *Calcium Orthophosphates in Nature, Biology and Medicine*. *Materials*, 2009. **2**(2): p. 399-498.
17. Eliaz, N. and N. Metoki, *Calcium Phosphate Bioceramics: A Review of Their History, Structure, Properties, Coating Technologies and Biomedical Applications*. *Materials (Basel)*, 2017. **10**(4).
18. Madupalli, H., B. Pavan, and M.M.J. Tecklenburg, *Carbonate substitution in the mineral component of bone: Discriminating the structural changes, simultaneously imposed by carbonate in A and B sites of apatite*. *Journal of Solid State Chemistry*, 2017. **255**: p. 27-35.
19. Garskaite, E., et al., *Effect of processing conditions on the crystallinity and structure of carbonated calcium hydroxyapatite (CHAp)*. *CrystEngComm*, 2014. **16**(19): p. 3950-3959.
20. LeGeros, R.Z. and J.P. LeGeros, *DENSE HYDROXYAPATITE*, in *An Introduction to Bioceramics*. 1993, WORLD SCIENTIFIC. p. 139-180.
21. Best, S.M., et al., *Bioceramics: Past, present and for the future*. *Journal of the European Ceramic Society*, 2008. **28**(7): p. 1319-1327.
22. Kubota, T., et al., *The effect of chemical potential on the thermodynamic stability of carbonate ions in hydroxyapatite*. *Acta Biomaterialia*, 2014. **10**(8): p. 3716-3722.
23. Lobo, S.E. and T.L. Arinzeh, *Biphasic Calcium Phosphate Ceramics for Bone Regeneration and Tissue Engineering Applications*. *Materials*, 2010. **3**(2): p. 815-826.
24. LeGeros, R.Z., et al., *Biphasic calcium phosphate bioceramics: preparation, properties and applications*. *J Mater Sci Mater Med*, 2003. **14**(3): p. 201-9.
25. Wang, G., et al., *Ordered HAp nanoarchitecture formed on HAp-TCP bioceramics by "nanocarving" and mineralization deposition and its potential use for guiding cell behaviors*. *Journal of Materials Chemistry B*, 2013. **1**(19): p. 2455-2462.
26. Carrodeguas, R.G. and S. De Aza, *α -Tricalcium phosphate: Synthesis, properties and biomedical applications*. *Acta Biomaterialia*, 2011. **7**(10): p. 3536-3546.

27. Mirhadi, B., B. Mehdikhani, and N. Askari, *Synthesis of nano-sized ??-tricalcium phosphate via wet precipitation*. Processing and Application of Ceramics, 2011. **5**.
28. Frasnelli, M. and V.M. Sglavo, *Effect of Mg(2+) doping on beta-alpha phase transition in tricalcium phosphate (TCP) bioceramics*. Acta Biomater, 2016. **33**: p. 283-9.
29. Doi, Y., et al., *Sintered carbonate apatites as bioresorbable bone substitutes*. Journal of Biomedical Materials Research, 1998. **39**(4): p. 603-610.
30. Boanini, E., M. Gazzano, and A. Bigi, *Ionic substitutions in calcium phosphates synthesized at low temperature*. Acta Biomaterialia, 2010. **6**(6): p. 1882-1894.
31. Qi, C., et al., *Magnesium whitlockite hollow microspheres: a comparison of microwave-hydrothermal and conventional hydrothermal syntheses using fructose 1,6-bisphosphate, and application in protein adsorption*. RSC Advances, 2016. **6**(40): p. 33393-33402.
32. Shah, F.A., et al., *Micrometer-Sized Magnesium Whitlockite Crystals in Micropetrosis of Bisphosphonate-Exposed Human Alveolar Bone*. Nano Letters, 2017. **17**(10): p. 6210-6216.
33. Lagier, R. and C.A. Baud, *Magnesium Whitlockite, a Calcium Phosphate Crystal of Special Interest in Pathology*. Pathology - Research and Practice, 2003. **199**(5): p. 329-335.
34. Fernandez de Grado, G., et al., *Bone substitutes: a review of their characteristics, clinical use, and perspectives for large bone defects management*. Journal of tissue engineering, 2018. **9**: p. 2041731418776819-2041731418776819.
35. Jones, J.R., E. Gentleman, and J. Polak, *Bioactive Glass Scaffolds for Bone Regeneration*. Elements, 2007. **3**(6): p. 393-399.
36. Fu, Q., et al., *Bioactive glass scaffolds for bone tissue engineering: state of the art and future perspectives*. Materials Science and Engineering: C, 2011. **31**(7): p. 1245-1256.
37. Hannink, G. and J.J.C. Arts, *Bioresorbability, porosity and mechanical strength of bone substitutes: What is optimal for bone regeneration?* Injury, 2011. **42**: p. S22-S25.
38. Hench, L.L., *Bioceramics*. Journal of the American Ceramic Society, 1998. **81**(7): p. 1705-1728.
39. Rahaman, M.N., et al., *Bioactive glass in tissue engineering*. Acta biomaterialia, 2011. **7**(6): p. 2355-2373.

40. Kokubo, T., *A/W GLASS-CERAMIC: PROCESSING AND PROPERTIES*, in *An Introduction to Bioceramics*. 2012, IMPERIAL COLLEGE PRESS. p. 171-187.
41. Palmero, P., *15 - Ceramic-polymer nanocomposites for bone-tissue regeneration*, in *Nanocomposites for Musculoskeletal Tissue Regeneration*, H. Liu, Editor. 2016, Woodhead Publishing: Oxford. p. 331-367.
42. Ratner, B.D., et al., *Introduction - Biomaterials Science: An Evolving, Multidisciplinary Endeavor*, in *Biomaterials Science (Third Edition)*, B.D. Ratner, et al., Editors. 2013, Academic Press.
43. O'Brien, F.J., *Biomaterials & scaffolds for tissue engineering*. *Materials Today*, 2011. **14**(3): p. 88-95.
44. Hench, L.L., *Bioceramics: From Concept to Clinic*. *Journal of the American Ceramic Society*, 1991. **74**(7): p. 1487-1510.
45. Yamamuro, T., *Bioceramics*, in *Biomechanics and Biomaterials in Orthopedics*, D.G. Poitout, Editor. 2004, Springer London: London. p. 22-33.
46. Patel, N. and P. Gohil. *A Review on Biomaterials : Scope , Applications & Human Anatomy Significance*. 2012.
47. Khan, W., et al., *Implantable Medical Devices*, in *Focal Controlled Drug Delivery*, A.J. Domb and W. Khan, Editors. 2014, Springer US: Boston, MA. p. 33-59.
48. Treiser, M., et al., *Chapter 1.2.6 - Degradable and Resorbable Biomaterials*, in *Biomaterials Science (Third Edition)*, B.D. Ratner, et al., Editors. 2013, Academic Press. p. 179-195.
49. Habibovic, P., et al., *Osteoinduction by biomaterials--physicochemical and structural influences*. *J Biomed Mater Res A*, 2006. **77**(4): p. 747-62.
50. LeGeros, R.Z., *Calcium Phosphate-Based Osteoinductive Materials*. *Chemical Reviews*, 2008. **108**(11): p. 4742-4753.
51. Oonishi, H. and H. Oomamiuda, *Chapter 9 Degradation/resorption in Bioactive Ceramics in Orthopaedics*, in *Handbook of Biomaterial Properties*, W. Murphy, J. Black, and G. Hastings, Editors. 2016, Springer New York: New York, NY. p. 495-507.
52. Karashima, S., et al., *Fabrication of low-crystallinity hydroxyapatite foam based on the setting reaction of α -tricalcium phosphate foam*. *Journal of Biomedical Materials Research Part A*, 2009. **88A**(3): p. 628-633.

53. Tang, R., L. Wang, and G.H. Nancollas, *Size-effects in the dissolution of hydroxyapatite: an understanding of biological demineralization*. Journal of Materials Chemistry, 2004. **14**(14): p. 2341-2346.
54. Lotsari, A., et al., *Transformation of amorphous calcium phosphate to bone-like apatite*. Nature Communications, 2018. **9**(1): p. 4170.
55. Dorozhkin, S.V., *Dissolution mechanism of calcium apatites in acids: A review of literature*. World journal of methodology, 2012. **2**(1): p. 1-17.
56. Bellucci, D., V. Cannillo, and A. Sola, *A New Highly Bioactive Composite for Bone Tissue Repair*. International Journal of Applied Ceramic Technology, 2012. **9**(3): p. 455-467.
57. Oonishi, H., et al., *Comparative bone growth behavior in granules of bioceramic materials of various sizes*. J Biomed Mater Res, 1999. **44**(1): p. 31-43.
58. Webster, T.J., et al., *Enhanced functions of osteoblasts on nanophase ceramics*. Biomaterials, 2000. **21**(17): p. 1803-1810.
59. Ivanchenko, P., et al., *On the surface effects of citrates on nano-apatites: evidence of a decreased hydrophilicity*. Scientific Reports, 2017. **7**(1): p. 8901.
60. Bracci, B., et al., *Effect of Mg²⁺, Sr²⁺, and Mn²⁺ on the chemico-physical and in vitro biological properties of calcium phosphate biomimetic coatings*. Journal of Inorganic Biochemistry, 2009. **103**(12): p. 1666-1674.
61. Nabiyouni, M., et al., *Magnesium-based bioceramics in orthopedic applications*. Acta Biomaterialia, 2018. **66**: p. 23-43.
62. Hung, C.C., et al., *The role of magnesium ions in bone regeneration involves the canonical Wnt signaling pathway*. Acta Biomater, 2019. **98**: p. 246-255.
63. Wang, Y., et al., *Unraveling the osteogenesis of magnesium by the activity of osteoblasts in vitro*. Journal of Materials Chemistry B, 2018. **6**(41): p. 6615-6621.
64. Rude, R.K., et al., *Magnesium Deficiency: Effect on Bone and Mineral Metabolism in the Mouse*. Calcified Tissue International, 2003. **72**(1): p. 32-41.
65. Cai, S., et al., *Fabrication and biological characteristics of β -tricalcium phosphate porous ceramic scaffolds reinforced with calcium phosphate glass*. Journal of Materials Science: Materials in Medicine, 2009. **20**(1): p. 351-358.
66. Xie, J., et al., *Simultaneous mechanical property and biodegradation improvement of wollastonite bioceramic through magnesium dilute*

- doping*. Journal of the Mechanical Behavior of Biomedical Materials, 2016. **54**: p. 60-71.
67. Liu, A., et al., *The outstanding mechanical response and bone regeneration capacity of robocast dilute magnesium-doped wollastonite scaffolds in critical size bone defects*. Journal of Materials Chemistry B, 2016. **4**(22): p. 3945-3958.
 68. Adeleke, S.A., A.R. Bushroa, and I. Sopyan, *Recent development of calcium phosphate-based coatings on titanium alloy implants*. Surface Engineering and Applied Electrochemistry, 2017. **53**(5): p. 419-433.
 69. Kowalski, P.S., et al., *Smart Biomaterials: Recent Advances and Future Directions*. ACS Biomaterials Science & Engineering, 2018. **4**(11): p. 3809-3817.
 70. Bohner, M., et al., *Synthesis of spherical calcium phosphate particles for dental and orthopedic applications*. Biomatter, 2013. **3**(2): p. e25103.
 71. Klein, C.P.A.T., et al., *Studies of the solubility of different calcium phosphate ceramic particles in vitro*. Biomaterials, 1990. **11**(7): p. 509-512.
 72. Dorozhkin, S.V. and M. Epple, *Biological and medical significance of calcium phosphates*. Angew Chem Int Ed Engl, 2002. **41**(17): p. 3130-46.
 73. Shepherd, J.H., D.V. Shepherd, and S.M. Best, *Substituted hydroxyapatites for bone repair*. J Mater Sci Mater Med, 2012. **23**(10): p. 2335-47.
 74. Merry, J.C., et al., *Synthesis and characterization of carbonate hydroxyapatite*. J Mater Sci Mater Med, 1998. **9**(12): p. 779-83.
 75. Layrolle, P., A. Ito, and T. Tateishi, *Sol-Gel Synthesis of Amorphous Calcium Phosphate and Sintering into Microporous Hydroxyapatite Bioceramics*. Journal of the American Ceramic Society, 1998. **81**(6): p. 1421-1428.
 76. Garskaite, E., et al., *Fabrication of a composite of nanocrystalline carbonated hydroxyapatite (cHAP) with polylactic acid (PLA) and its surface topographical structuring with direct laser writing (DLW)*. RSC Advances, 2016. **6**(76): p. 72733-72743.
 77. Uota, M., et al., *Synthesis of High Surface Area Hydroxyapatite Nanoparticles by Mixed Surfactant-Mediated Approach*. Langmuir, 2005. **21**(10): p. 4724-4728.
 78. Fihri, A., et al., *Hydroxyapatite: A review of syntheses, structure and applications in heterogeneous catalysis*. Coordination Chemistry Reviews, 2017. **347**: p. 48-76.

79. Suchanek, W. and M. Yoshimura, *Processing and properties of hydroxyapatite-based biomaterials for use as hard tissue replacement implants*. Journal of Materials Research, 1998. **13**(1): p. 94-117.
80. Royer, A., et al., *Stoichiometry of hydroxyapatite: influence on the flexural strength*. Journal of Materials Science: Materials in Medicine, 1993. **4**(1): p. 76-82.
81. ŚAlósarczyk, A., et al., *Calcium Phosphate Materials Prepared from Precipitates with Various Calcium:Phosphorus Molar Ratios*. Journal of the American Ceramic Society, 1996. **79**(10): p. 2539-2544.
82. Islam, M.T., et al., *Bioactive calcium phosphate-based glasses and ceramics and their biomedical applications: A review*. J Tissue Eng, 2017. **8**: p. 2041731417719170.
83. Sepulveda, P., J.R. Jones, and L.L. Hench, *In vitro dissolution of melt-derived 45S5 and sol-gel derived 58S bioactive glasses*. Journal of Biomedical Materials Research, 2002. **61**(2): p. 301-311.
84. Li, J.J., D.L. Kaplan, and H. Zreiqat, *Scaffold-based regeneration of skeletal tissues to meet clinical challenges*. Journal of Materials Chemistry B, 2014. **2**(42): p. 7272-7306.
85. Dorozhkin, S.V., *Calcium Orthophosphate-Based Bioceramics*. Materials, 2013. **6**(9).
86. Prakasam, M., et al., *Fabrication, Properties and Applications of Dense Hydroxyapatite: A Review*. Journal of functional biomaterials, 2015. **6**(4): p. 1099-1140.
87. Brunski, J.B., *Chapter i.2.3 - Metals: Basic Principles*, in *Biomaterials Science (Third Edition)*, B.D. Ratner, et al., Editors. 2013, Academic Press. p. 111-119.
88. Ma, P.X., *Scaffolds for tissue fabrication*. Materials Today, 2004. **7**(5): p. 30-40.
89. Nair, L.S. and C.T. Laurencin, *Biodegradable polymers as biomaterials*. Progress in Polymer Science, 2007. **32**(8): p. 762-798.
90. Henton, D.E., et al., *Poly(lactic Acid) Technology*. in *Natural Fibers, Biopolymers, and Biocomposites*, 2005. Edited By Amar K. Mohanty, Manjusri Misra, Lawrence T. Drzal, 1st Edition, Taylor and Francis group, CRS Press (527-578 p.): p. eBook ISBN 9780429211607.
91. Engelberg, I. and J. Kohn, *Physico-mechanical properties of degradable polymers used in medical applications: A comparative study*. Biomaterials, 1991. **12**(3): p. 292-304.
92. Maurus, P.B. and C.C. Kaeding, *Bioabsorbable implant material review*. Operative Techniques in Sports Medicine, 2004. **12**(3): p. 158-160.

93. Woodruff, M.A. and D.W. Hutmacher, *The return of a forgotten polymer—Polycaprolactone in the 21st century*. Progress in Polymer Science, 2010. **35**(10): p. 1217-1256.
94. Huang, M.-H., et al., *Degradation characteristics of poly(ϵ -caprolactone)-based copolymers and blends*. Journal of Applied Polymer Science, 2006. **102**(2): p. 1681-1687.
95. Middleton, J.C. and A.J. Tipton, *Synthetic biodegradable polymers as orthopedic devices*. Biomaterials, 2000. **21**(23): p. 2335-2346.
96. Veronese, F.M. and G. Pasut, *PEGylation, successful approach to drug delivery*. Drug Discovery Today, 2005. **10**(21): p. 1451-1458.
97. Dee, K.C., Puleo, D.A. and Bizios, R., *Protein-Surface Interactions*. An Introduction To Tissue-Biomaterial Interactions, 2002: p. 37-52.
98. A., L.R., *Biomaterials: Protein–Surface Interactions*. Encyclopedia of Biomaterials and Biomedical Engineering, 2005. Edited By Gary E. Wnek, Gary L. Bowlin, Ch: p. 1-15.
99. Yamaoka, T., Y. Tabata, and Y. Ikada, *Distribution and Tissue Uptake of Poly(ethylene glycol) with Different Molecular Weights after Intravenous Administration to Mice*. Journal of Pharmaceutical Sciences, 1994. **83**(4): p. 601-606.
100. Zhu, J., *Bioactive modification of poly(ethylene glycol) hydrogels for tissue engineering*. Biomaterials, 2010. **31**(17): p. 4639-4656.
101. Allen, T.M. and P.R. Cullis, *Drug Delivery Systems: Entering the Mainstream*. Science, 2004. **303**(5665): p. 1818.
102. Hans, M.L. and A.M. Lowman, *Biodegradable nanoparticles for drug delivery and targeting*. Current Opinion in Solid State and Materials Science, 2002. **6**(4): p. 319-327.
103. Oh, J.K., *Poly(lactide (PLA))-based amphiphilic block copolymers: synthesis, self-assembly, and biomedical applications*. Soft Matter, 2011. **7**(11): p. 5096-5108.
104. Lee, J.H., et al., *Tissue anti-adhesion potential of ibuprofen-loaded PLLA–PEG diblock copolymer films*. Biomaterials, 2005. **26**(6): p. 671-678.
105. Liu, S., et al., *Prevention of peritendinous adhesions with electrospun ibuprofen-loaded poly(L-lactic acid)-polyethylene glycol fibrous membranes*. Tissue Eng Part A, 2013. **19**(3-4): p. 529-37.
106. Yang, D.-J., et al., *Tissue anti-adhesion potential of biodegradable PELA electrospun membranes*. Acta Biomaterialia, 2009. **5**(7): p. 2467-2474.

107. Zhang, Z., et al., *Biodegradable and thermoreversible PCLA–PEG–PCLA hydrogel as a barrier for prevention of post-operative adhesion*. *Biomaterials*, 2011. **32**(21): p. 4725-4736.
108. Park, S.N., et al., *Preparation and characterization of biodegradable anti-adhesive membrane for peritoneal wound healing*. *J Mater Sci Mater Med*, 2007. **18**(3): p. 475-82.
109. Tessmar, J.K. and A.M. Göpferich, *Customized PEG-derived copolymers for tissue-engineering applications*. *Macromol Biosci*, 2007. **7**(1): p. 23-39.
110. Ignjatović, N., et al., *A study of HAp/PLLA composite as a substitute for bone powder, using FT-IR spectroscopy*. *Biomaterials*, 2001. **22**(6): p. 571-575.
111. Cao, L., et al., *Degradation and osteogenic potential of a novel poly(lactic acid)/nano-sized β -tricalcium phosphate scaffold*. *International journal of nanomedicine*, 2012. **7**: p. 5881-5888.
112. Ródenas-Rochina, J., J.L. Ribelles, and M. Lebourg, *Comparative study of PCL-HAp and PCL-bioglass composite scaffolds for bone tissue engineering*. *J Mater Sci Mater Med*, 2013. **24**(5): p. 1293-308.
113. Poh, P.S.P., et al., *In vitro and in vivo bone formation potential of surface calcium phosphate-coated polycaprolactone and polycaprolactone/bioactive glass composite scaffolds*. *Acta Biomater*, 2016. **30**: p. 319-333.
114. Kang, Y., et al., *Enhanced mechanical performance and biological evaluation of a PLGA coated β -TCP composite scaffold for load-bearing applications*. *Eur Polym J*, 2011. **47**(8): p. 1569-1577.
115. Zhang, P., et al., *In vivo mineralization and osteogenesis of nanocomposite scaffold of poly(lactide-co-glycolide) and hydroxyapatite surface-grafted with poly(l-lactide)*. *Biomaterials*, 2009. **30**(1): p. 58-70.
116. Zhang, B., et al., *Tissue-engineered composite scaffold of poly(lactide-co-glycolide) and hydroxyapatite nanoparticles seeded with autologous mesenchymal stem cells for bone regeneration*. *J Zhejiang Univ Sci B*, 2017. **18**(11): p. 963-976.
117. Saravanan, S., R.S. Leena, and N. Selvamurugan, *Chitosan based biocomposite scaffolds for bone tissue engineering*. *International Journal of Biological Macromolecules*, 2016. **93**: p. 1354-1365.
118. Yan, J., et al., *Injectable alginate/hydroxyapatite gel scaffold combined with gelatin microspheres for drug delivery and bone tissue engineering*. *Mater Sci Eng C Mater Biol Appl*, 2016. **63**: p. 274-84.

119. Ferreira, A.M., et al., *Collagen for bone tissue regeneration*. Acta Biomaterialia, 2012. **8**(9): p. 3191-3200.
120. Zhao, J., et al., *Apatite-coated silk fibroin scaffolds to healing mandibular border defects in canines*. Bone, 2009. **45**(3): p. 517-527.
121. Noori, A., et al., *A review of fibrin and fibrin composites for bone tissue engineering*. International journal of nanomedicine, 2017. **12**: p. 4937-4961.
122. Zhai, P., et al., *The application of hyaluronic acid in bone regeneration*. International Journal of Biological Macromolecules, 2020. **151**: p. 1224-1239.
123. Filippi, M., et al., *Natural Polymeric Scaffolds in Bone Regeneration*. Frontiers in bioengineering and biotechnology, 2020. **8**: p. 474-474.
124. Mariani, E., et al., *Biomaterials: Foreign Bodies or Tuners for the Immune Response?* International journal of molecular sciences, 2019. **20**(3): p. 636.
125. Miranda-Nieves, D. and E.L. Chaikof, *Collagen and Elastin Biomaterials for the Fabrication of Engineered Living Tissues*. ACS Biomaterials Science & Engineering, 2017. **3**(5): p. 694-711.
126. Ber, S., G. Torun Köse, and V. Hasırcı, *Bone tissue engineering on patterned collagen films: an in vitro study*. Biomaterials, 2005. **26**(14): p. 1977-1986.
127. Gómez-Guillén, M.C., et al., *Functional and bioactive properties of collagen and gelatin from alternative sources: A review*. Food Hydrocolloids, 2011. **25**(8): p. 1813-1827.
128. Teotia, A.K., et al., *Gelatin-Modified Bone Substitute with Bioactive Molecules Enhance Cellular Interactions and Bone Regeneration*. ACS Applied Materials & Interfaces, 2016. **8**(17): p. 10775-10787.
129. Luo, Y., et al., *3D printing of concentrated alginate/gelatin scaffolds with homogeneous nano apatite coating for bone tissue engineering*. Materials & Design, 2018. **146**: p. 12-19.
130. Vázquez, B., et al., *Acrylic bone cements modified with -TCP particles encapsulated with poly(ethylene glycol)*. Biomaterials, 2005. **26**(20): p. 4309-4316.
131. Singh, M.K., et al., *Hydroxyapatite Modified with Carbon-Nanotube-Reinforced Poly(methyl methacrylate): A Nanocomposite Material for Biomedical Applications*. Advanced Functional Materials, 2008. **18**(5): p. 694-700.
132. Chen, L., et al., *Silicate bioceramic/PMMA composite bone cement with distinctive physicochemical and bioactive properties*. RSC Advances, 2015. **5**(47): p. 37314-37322.

133. Ravarian, R., et al., *Bioactive poly(methyl methacrylate) for bone fixation*. RSC Advances, 2015. **5**(75): p. 60681-60690.
134. Davis, H. and J.K. Leach, *Hybrid and composite biomaterials for tissue engineering (Ch. 10) in Multifunctional Biomaterials and Devices* (Ed. N. Ashammakhi), 2008: p. p.26.
135. Salinas, A.J. and M. Vallet-Regi, *Bioactive ceramics: from bone grafts to tissue engineering*. RSC Advances, 2013. **3**(28): p. 11116-11131.
136. Poh, P.S.P., et al., *Optimization of Bone Scaffold Porosity Distributions*. Scientific Reports, 2019. **9**(1): p. 9170.
137. Kuttappan, S., D. Mathew, and M.B. Nair, *Biomimetic composite scaffolds containing bioceramics and collagen/gelatin for bone tissue engineering - A mini review*. International Journal of Biological Macromolecules, 2016. **93**: p. 1390-1401.
138. Essa, D., et al., *The Design of Poly(lactide-co-glycolide) Nanocarriers for Medical Applications*. Frontiers in Bioengineering and Biotechnology, 2020. **8**(48).
139. Makadia, H.K. and S.J. Siegel, *Poly Lactic-co-Glycolic Acid (PLGA) as Biodegradable Controlled Drug Delivery Carrier*. Polymers, 2011. **3**(3): p. 1377-1397.
140. Arahira, T., et al., *Development and characterization of a novel porous β -TCP scaffold with a three-dimensional PLLA network structure for use in bone tissue engineering*. Materials Letters, 2015. **152**: p. 148-150.
141. Selvaraju, S., S. Ramalingam, and J.R. Rao, *Inorganic apatite nanomaterial: Modified surface phenomena and its role in developing collagen based polymeric bio-composite (Coll-PLGA/HAp) for biological applications*. Colloids and Surfaces B: Biointerfaces, 2018. **172**: p. 734-742.
142. Costantini, M. and A. Barbetta, *6 - Gas foaming technologies for 3D scaffold engineering*, in *Functional 3D Tissue Engineering Scaffolds*, Y. Deng and J. Kuiper, Editors. 2018, Woodhead Publishing. p. 127-149.
143. Chen, W., et al., *Gas-foaming calcium phosphate cement scaffold encapsulating human umbilical cord stem cells*. Tissue engineering. Part A, 2012. **18**(7-8): p. 816-827.
144. Hesaraki, S., F. Moztarzadeh, and D. Sharifi, *Formation of interconnected macropores in apatitic calcium phosphate bone cement with the use of an effervescent additive*. J Biomed Mater Res A, 2007. **83**(1): p. 80-7.

145. Habibovic, P., et al., *3D microenvironment as essential element for osteoinduction by biomaterials*. *Biomaterials*, 2005. **26**(17): p. 3565-3575.
146. Barbetta, A., et al., *Tailoring the Porosity and Morphology of Gelatin-Methacrylate PolyHIPE Scaffolds for Tissue Engineering Applications*. *Langmuir*, 2005. **21**(26): p. 12333-12341.
147. Schardosim, M., et al., *Freeze-casting for PLGA/carbonated apatite composite scaffolds: Structure and properties*. *Materials Science and Engineering: C*, 2017. **77**: p. 731-738.
148. Lee, A., et al., *Bioceramic nanocomposite thiol-acrylate polyHIPE scaffolds for enhanced osteoblastic cell culture in 3D*. *Biomaterials Science*, 2017. **5**(10): p. 2035-2047.
149. Gendviliene, I., et al., *Assessment of the morphology and dimensional accuracy of 3D printed PLA and PLA/HAp scaffolds*. *Journal of the Mechanical Behavior of Biomedical Materials*, 2020. **104**: p. 103616.
150. Lee, J. and G. Kim, *Calcium-Deficient Hydroxyapatite/Collagen/Platelet-Rich Plasma Scaffold with Controlled Release Function for Hard Tissue Regeneration*. *ACS Biomaterials Science & Engineering*, 2018. **4**(1): p. 278-289.
151. Shuai, C., et al., *Development of composite porous scaffolds based on poly(lactide-co-glycolide)/nano-hydroxyapatite via selective laser sintering*. *The International Journal of Advanced Manufacturing Technology*, 2013. **69**(1): p. 51-57.
152. "Dental Radiographic Examinations: Recommendations for Patient Selection and Limiting Radiation Exposure". American Dental Association (ADA), Council on Scientific Affairs, 2012. U.S. Department of Health and Human Services, Food and Drug Administration (FDA).
153. Mashiatulla, M., R.D. Ross, and D.R. Sumner, *Validation of cortical bone mineral density distribution using micro-computed tomography*. *Bone*, 2017. **99**: p. 53-61.
154. Jones, J.R., et al., *Non-destructive quantitative 3D analysis for the optimisation of tissue scaffolds*. *Biomaterials*, 2007. **28**(7): p. 1404-1413.
155. Jones, A.C., et al., *Assessment of bone ingrowth into porous biomaterials using MICRO-CT*. *Biomaterials*, 2007. **28**(15): p. 2491-2504.
156. Wagoner Johnson, A.J. and B.A. Herschler, *A review of the mechanical behavior of CaP and CaP/polymer composites for applications in bone replacement and repair*. *Acta Biomaterialia*, 2011. **7**(1): p. 16-30.

157. Weiner, S. and H.D. Wagner, *THE MATERIAL BONE: Structure-Mechanical Function Relations*. Annual Review of Materials Science, 1998. **28**(1): p. 271-298.
158. Kazakia, G.J., et al., *Assessment of bone tissue mineralization by conventional x-ray microcomputed tomography: comparison with synchrotron radiation microcomputed tomography and ash measurements*. Medical physics, 2008. **35**(7): p. 3170-3179.
159. Hu, H., et al., *Four Multidetector-Row Helical CT: Image Quality and Volume Coverage Speed*. Radiology, 2000. **215**(1): p. 55-62.
160. Mozzo, P., et al., *A new volumetric CT machine for dental imaging based on the cone-beam technique: preliminary results*. Eur Radiol, 1998. **8**(9): p. 1558-64.
161. Baba, R., et al., *Comparison of flat-panel detector and image-intensifier detector for cone-beam CT*. Comput Med Imaging Graph, 2002. **26**(3): p. 153-8.
162. Baba, R., K. Ueda, and M. Okabe, *Using a flat-panel detector in high resolution cone beam CT for dental imaging*. Dentomaxillofac Radiol, 2004. **33**(5): p. 285-90.
163. Loubele, M., et al., *Comparison between effective radiation dose of CBCT and MSCT scanners for dentomaxillofacial applications*. Eur J Radiol, 2009. **71**(3): p. 461-8.
164. Faure, J., et al., *A new sol-gel synthesis of 45S5 bioactive glass using an organic acid as catalyst*. Materials Science and Engineering: C, 2015. **47**: p. 407-412.
165. Kokubo, T. and H. Takadama, *How useful is SBF in predicting in vivo bone bioactivity?* Biomaterials, 2006. **27**(15): p. 2907-2915.
166. Boccaccini, A.R., et al., *Sintering, crystallisation and biodegradation behaviour of Bioglass[registered sign]-derived glass-ceramics*. Faraday Discussions, 2007. **136**(0): p. 27-44.
167. Massera, J., et al., *Crystallization Mechanism of the Bioactive Glasses, 45S5 and S53P4*. Journal of the American Ceramic Society, 2012. **95**(2): p. 607-613.
168. Golovchak, R., et al., *Influence of phase separation on the devitrification of 45S5 bioglass*. Acta Biomaterialia, 2014. **10**(11): p. 4878-4886.
169. Kramer, C.M., Z.A. Munir, and J.V. Volponi, *Differential scanning calorimetry of sodium and potassium nitrates and nitrites*. Thermochemica Acta, 1982. **55**(1): p. 11-17.

170. Siqueira, R.L., O. Peitl, and E.D. Zanotto, *Gel-derived SiO₂–CaO–Na₂O–P₂O₅ bioactive powders: Synthesis and in vitro bioactivity*. *Materials Science and Engineering: C*, 2011. **31**(5): p. 983-991.
171. Cacciotti, I., et al., *Sol–gel derived 45S5 bioglass: synthesis, microstructural evolution and thermal behaviour*. *Journal of Materials Science: Materials in Medicine*, 2012. **23**(8): p. 1849-1866.
172. Pirayesh, H. and J.A. Nychka, *Sol–Gel Synthesis of Bioactive Glass–Ceramic 45S5 and its in vitro Dissolution and Mineralization Behavior*. *Journal of the American Ceramic Society*, 2013. **96**(5): p. 1643-1650.
173. González-Benito, J. and G. González-Gaitano, *Interfacial Conformations and Molecular Structure of PMMA in PMMA/Silica Nanocomposites. Effect of High-Energy Ball Milling*. *Macromolecules*, 2008. **41**(13): p. 4777-4785.
174. Salinas, A.J., M. Vallet-Regi, and I. Izquierdo-Barba, *Biomimetic Apatite Deposition on Calcium Silicate Gel Glasses*. *Journal of Sol-Gel Science and Technology*, 2001. **21**(1): p. 13-25.
175. Pereira, M.M., A.E. Clark, and L.L. Hench, *Calcium phosphate formation on sol-gel-derived bioactive glasses in vitro*. *Journal of Biomedical Materials Research*, 1994. **28**(6): p. 693-698.
176. Riau, A.K., et al., *Surface Modification of PMMA to Improve Adhesion to Corneal Substitutes in a Synthetic Core–Skirt Keratoprosthesis*. *ACS Applied Materials & Interfaces*, 2015. **7**(39): p. 21690-21702.
177. Serizawa, T., et al., *Stepwise Stereocomplex Assembly of Stereoregular Poly(methyl methacrylate)s on a Substrate*. *Journal of the American Chemical Society*, 2000. **122**(9): p. 1891-1899.
178. Thavornnyutikarn, B., et al., *Porous 45S5 Bioglass®-based scaffolds using stereolithography: Effect of partial pre-sintering on structural and mechanical properties of scaffolds*. *Materials Science and Engineering: C*, 2017. **75**: p. 1281-1288.
179. Wang, X., et al., *45S5 Bioglass analogue reinforced akermanite ceramic favorable for additive manufacturing mechanically strong scaffolds*. *RSC Advances*, 2015. **5**(124): p. 102727-102735.
180. Minaberry, Y. and M. Jobbágy, *Macroporous Bioglass Scaffolds Prepared by Coupling Sol–Gel with Freeze Drying*. *Chemistry of Materials*, 2011. **23**(9): p. 2327-2332.
181. Daguano, J.K.M.F., et al., *Effect of partial crystallization on the mechanical properties and cytotoxicity of bioactive glass from the 3CaO.P₂O₅–SiO₂–MgO system*. *Journal of the Mechanical Behavior of Biomedical Materials*, 2012. **14**: p. 78-88.

182. Sabree, I., J.E. Gough, and B. Derby, *Mechanical properties of porous ceramic scaffolds: Influence of internal dimensions*. *Ceramics International*, 2015. **41**(7): p. 8425-8432.
183. Shinzato, S., et al., *A new bioactive bone cement: Effect of glass bead filler content on mechanical and biological properties*. *Journal of Biomedical Materials Research*, 2001. **54**(4): p. 491-500.
184. Lewis, G., *Alternative acrylic bone cement formulations for cemented arthroplasties: Present status, key issues, and future prospects*. *Journal of Biomedical Materials Research Part B: Applied Biomaterials*, 2008. **84B**(2): p. 301-319.
185. Arora, M., et al., *Polymethylmethacrylate bone cements and additives: A review of the literature*. *World Journal of Orthopedics*, 2013. **4**(2): p. 67-74.
186. Pereira, M.M., A.E. Clark, and L.L. Hench, *Effect of Texture on the Rate of Hydroxyapatite Formation on Gel-Silica Surface*. *Journal of the American Ceramic Society*, 1995. **78**(9): p. 2463-2468.
187. Querido, W., et al., *Ultrastructural and Mineral Phase Characterization of the Bone-Like Matrix Assembled in F-OST Osteoblast Cultures*. *Calcified Tissue International*, 2011. **89**(5): p. 358.
188. Raynaud, S., et al., *Calcium phosphate apatites with variable Ca/P atomic ratio I. Synthesis, characterisation and thermal stability of powders*. *Biomaterials*, 2002. **23**(4): p. 1065-1072.
189. Radin, S., et al., *The effect of in vitro modeling conditions on the surface reactions of bioactive glass*. *Journal of Biomedical Materials Research*, 1997. **37**(3): p. 363-375.
190. Maria Vallet-Regi, D.A.N., *Biological Apatites in Bone and Teeth*. in *Nanoceramics in Clinical Use: From Materials to Applications (Ed 2)*, 2015. **Chapter 1**: p. 1-29.
191. Golubevas, R., et al., *Fabrication and investigation of high-quality glass-ceramic (GC)-polymethyl methacrylate (PMMA) composite for regenerative medicine*. *RSC Advances*, 2017. **7**(53): p. 33558-33567.
192. Jevtić, M., et al., *Crystal Structure of Hydroxyapatite Nanorods Synthesized by Sonochemical Homogeneous Precipitation*. *Crystal Growth & Design*, 2008. **8**(7): p. 2217-2222.
193. Hasegawa, M., Y. Doi, and A. Uchida, *Cell-mediated bioresorption of sintered carbonate apatite in rabbits*. *The Journal of Bone and Joint Surgery*. British volume, 2003. **85-B**(1): p. 142-147.
194. Germaini, M.-M., et al., *Osteoblast and osteoclast responses to A/B type carbonate-substituted hydroxyapatite ceramics for bone regeneration*. *Biomaterials*, 2017. **12**(3): p. 035008.

195. de Mul, F.F., et al., *Micro-Raman line broadening in synthetic carbonated hydroxyapatite*. J Dent Res, 1986. **65**(3): p. 437-40.
196. Marques, M.P.M., et al., *Heat-induced Bone Diagenesis Probed by Vibrational Spectroscopy*. Scientific Reports, 2018. **8**(1): p. 15935.
197. Yasukawa, A., K. Kandori, and T. Ishikawa, *TPD-TG-MS Study of Carbonate Calcium Hydroxyapatite Particles*. Calcified Tissue International, 2003. **72**(3): p. 243-250.
198. Tuncel, A. and E. Pişkin, *Nonswellable and swellable poly(EGDMA) microspheres*. Journal of Applied Polymer Science, 1996. **62**(5): p. 789-798.
199. Minhas, M.U., et al., *Synthesis and Characterization of Biodegradable Hydrogels for Oral Delivery of 5-Fluorouracil Targeted to Colon: Screening with Preliminary In Vivo Studies*. Advances in Polymer Technology, 2018. **37**(1): p. 221-229.
200. Huang, C.-W., Y.-M. Sun, and W.-F. Huang, *Curing kinetics of the synthesis of poly(2-hydroxyethyl methacrylate) (PHEMA) with ethylene glycol dimethacrylate (EGDMA) as a crosslinking agent*. Journal of Polymer Science Part A: Polymer Chemistry, 1997. **35**(10): p. 1873-1889.
201. Cipitria, A., et al., *Porous scaffold architecture guides tissue formation*. Journal of Bone and Mineral Research, 2012. **27**(6): p. 1275-1288.
202. Petersen, A., et al., *A biomaterial with a channel-like pore architecture induces endochondral healing of bone defects*. Nature communications, 2018. **9**(1): p. 4430-4430.
203. Kampschulte, M., et al., *Nano-Computed Tomography: Technique and Applications*. Rofo-Fortschritte Auf Dem Gebiet Der Rontgenstrahlen Und Der Bildgebenden Verfahren, 2016. **188**(2): p. 146-154.
204. Borkowski, L., et al., *New approach in evaluation of ceramic-polymer composite bioactivity and biocompatibility*. Analytical and bioanalytical chemistry, 2017. **409**(24): p. 5747-5755.
205. Novakofski, K.D., et al., *High-Resolution Methods for Diagnosing Cartilage Damage In Vivo*. Cartilage, 2016. **7**(1): p. 39-51.
206. Kotnis, N.A., et al., *Chronology of the radiographic appearances of the calcium sulphate–calcium phosphate synthetic bone graft composite following resection of bone tumours—a preliminary study of the normal post-operative appearances*. Skeletal Radiology, 2011. **40**(5): p. 563-570.
207. Duan, R., et al., *Modulating Bone Regeneration in Rabbit Condyle Defects with Three Surface-Structured Tricalcium Phosphate*

- Ceramics*. ACS Biomaterials Science & Engineering, 2018. **4**(9): p. 3347-3355.
208. Karageorgiou, V. and D. Kaplan, *Porosity of 3D biomaterial scaffolds and osteogenesis*. Biomaterials, 2005. **26**(27): p. 5474-5491.
209. Dalby, M.J., et al., *Increasing hydroxyapatite incorporation into poly(methylmethacrylate) cement increases osteoblast adhesion and response*. Biomaterials, 2002. **23**(2): p. 569-576.

ACKNOWLEDGEMENTS

I would like to express my gratitude to all of those who enabled me to develop and produce my PhD research work.

Huge thanks to **Prof. Habil. Dr. Aivaras Kareiva** who integrated me into his amazing group of scientists; to my supervisor **Assoc. Prof. Dr. Edita Garškaitė** for her suggestions, dedication and all the support throughout the development of my research work and exchange of ideas as well as for her help all along the process of completing my PhD; to my colleagues **Dr. Živilė Stankevičiūtė, Laurynas Alinauskas, Dr. Aleksej Žarkov, Doc. dr. Ramūnas Skaudžius** from Vilnius University Faculty of Chemistry and Geosciences who directly helped me during the development of my PhD; to my brother **Raimundas Golubevas** MD, DDS oral & maxillofacial surgeon from the Hospital of the Lithuanian University of Health Sciences Kaunas Clinics for his support, dedication and exchange of knowledge. Thanks to my Best Friends, for their motivation, support and dedication.

Special Thanks to my **Parents**, and my wife **Živilė** and my son **Mykolas** for their support, dedication, motivation and for their faith in me.

TO EVERYONE, MY SINCERE THANKS.

SANTRAUKA

TURINYS

ĮVADAS.....	96
1. EKSPERIMENTINĖ DALIS	97
2. REZULTATAI IR JŲ APTARIMAS.....	98
IŠVADOS.....	115

ĮVADAS

Įvairūs kaulų defektai yra viena iš pagrindinių gyvenimo kokybės sumažėjimo priežasčių. Dažnu atveju tai nulemia traumos ar ligos (pvz., vėžio, su osteoporozė susijusių lūžių, įgimtų kaulų apsigimimų), senėjimo procesai, intensyvi sportinė veikla, nutukimas ar jonų trūkumas (pvz., lemia disfunkciją ir kaulinio audinio ligas, pvz., osteoporozė ir osteomalacija). Natūralus kaulų regeneravimo procesas yra pakankamas, kad atsinaujintų daugumoje kaulų lūžių, tačiau būna atvejų kai kaulinis audinys negali susidoroti su didelio dydžio „kritiniais“ pažeidimais.

Nuosavas paciento kaulas, žmogaus donoro ar kitos giminingos rūšies donoro kaulas buvo pirmieji terapiniai metodai kaulų audinio pakeitimui ir vis dar pagrindinis pasirinkimas chirurginėms procedūroms. Siekiant parinkti idealų transplantatą, pvz.: autotransplantus (t.y. kaulų transplantaciją iš vienos dalies į kitą to paties kūno dalį), alotransplantus (t.y. kaulų transplantaciją iš tos pačios rūšies donoro) ir ksenotransplantus (t.y. iš kitų rūšių), reikia įvertinti kaulinį audinį, kaulo defektų dydį, audinių gyvybingumą, biomechanines savybes, transplantato tvarkymą ir išlaidas.

Kaulinio audinio regeneracijos srityje pagrindinis uždavinys yra pasiekti veiksmingą terapiją, kuri padėtų visiškai atsistatyti audiniams be pakartotinės operacijos. Kita vertus, išmaniosios biomedžiagos gali būti sukurtos kaip sistemos terapinėms medžiagoms tiekti tiesiai į tikslinę vietą, taip išvengiant sisteminio vartojimo. Pažanga šiuo atžvilgiu gali garantuoti standartizuotą veikimą (pvz., priešingai nei autologinis ar heterologinis kaulas), taip pat sumažinti neigiamą poveikį ir pagerinti osteokonduktyvumą, osteoinduktyvumą ir osteointegraciją.

Audinių inžinerija (AI) buvo tirta kaip novatoriškas būdas sukurti biomimetinius šablonus kaulinio audinio defektams regeneruoti. Aštuntojo dešimtmečio viduryje Langeris ir Vacanti apibrėžė audinių inžineriją kaip „besiformuojančią ir daugiapakopę mokslo sritį, kurioje inžinerijos ir gyvybės mokslų principai taikomi kuriant biologinius pakaitalus, kurie atstato ar sustiprina audinių ir organų funkcijas“, derindami ląsteles, biomedžiagas taip, jog pagerėja biomolekuliniai signalai (pvz., augimo faktoriai ar kaulų morfogeniniai baltymai) ir biomedžiagų osteogeniškumas, osteokonduktyvumas ir osteoinduktyvumo savybės. Kita vertus, tinkamos mechaninės savybės ir tinkamas skilimo greitis buvo pasiektas taikant tradicinius kaulų transplantacijos metodus, nes juos lengva naudoti klinikinėje praktikoje.

Šioje disertacijoje aprašyto darbo originali idėja buvo sukurti naujas biomimetines hibridines biomedžiagas, kurias būtų galima panaudoti naujoviškose išmaniose ir individualizuotose medicinos srityse, ypač kaulų audinio inžinerijos srityje. Ši veikla yra svarbi bioaktyvioms, bioresorbuojamoms ir protingoms biomedžiagoms, galinčioms iš esmės suaktyvinti, skatinti ir palaikyti biologinius procesus, užtikrinančius audinių regeneraciją. Ypač reikalingos į dirgiklius reaguojančios, biologiškai suderinamos medžiagos, kurios veiksmingiau ir individualizuotai pritaikomos medicinoje.

Šio **darbo tikslas** yra daugiafunkcinių neorganinių (biokeraminių)-organinių (polimerinių) kompozitų, kaip potencialių kaulinio audinio pakaitalų, sukūrimas.

Šiam tikslui įgyvendinti suformuluotos tokios užduotys:

1. Susintetinti ir apibūdinti Na-Ca-Si-P-O stiklo keramikos biomedžiagą ir apibūdinti vienfazį nanokristalinį karbonato jonais pakeistą hidroksiapatitą (cHAP).

2. Pagaminti hibridinius neorganinius-organinius kompozitus, susidedančius iš Na-Ca-Si-P-O stiklo keramikos ir polimetilmetakrilato (PMMA), ir apibūdinti jų tirpumą fiziologinius skysčius imituojančiame tirpale bei ištirti mechanines savybes.

3. Pagaminti hibridinius neorganinius-organinius kompozitus, susidedančius iš cHAP, akrilato ir želatinos, ir ištirti jų hidrofiliškumo savybes.

4. Pagaminti porėtus hibridinius neorganinius-organinius kompozitus, susidedančius iš cHAP ir polietilenglikolioldiakrilato (PEGDA), naudojant putojimo agentą azodikarbonamidą (ADCA) ir ištirti jų sorbcines savybes.

1. EKSPERIMENTINĖ DALIS

Eksperimento metodikos skyrius sudarytas iš trijų poskyrių. Pirmame poskyryje yra išvardintos pradinių junginių sintezei ir kompozitų gamybai naudotos medžiagos, nurodant jų grynumą bei gamintoją. Antrame poskyryje yra pateiktas detalus disertacijoje nagrinėtų junginių ir kompozitų sintezės aprašymas, t.y. stiklo-keramikos sintezė zolių-gelių metodu, stiklo-keramikos ir polimetilmetakrilato kompozitinės medžiagos sintezė iš pirminio monomero panaudojant foto iniciatorius, karbonatinio hidroksiapatito (cHAP) sintezė, multikompozitinio karkaso sintezė panaudojant želatiną ir tinklinę polimerizaciją inicijuojančius monomerus bei fotoiniciatorius. Taip pat aprašytas fiziologinius skysčius imituojančio tirpalo (SBF) gamybos

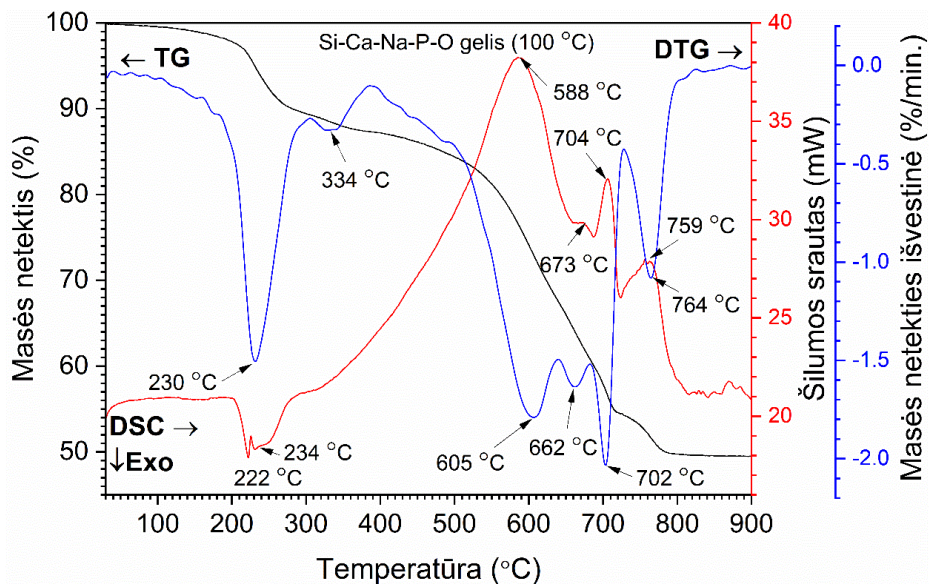
metodika. Trečiame poskyryje yra išsamiai aprašyta susintetintų junginių bei pagamintų kompozitų cheminės sudėties, struktūros, morfologijos, mechaninių, hidrofiliškumo bei kitų fizikinių ir cheminių savybių tyrimams naudota įranga.

2. REZULTATAI IR JŲ APTARIMAS

2.1. Stiklo-keramikos (GC)-polimetilmetakrilato (PMMA) kompozitinės medžiagos

Šioje dalyje pateikti Na-Ca-Si-P-O bioaktyvaus stiklo ir kompozitinių BG-PMMA mėginių sintezės ir apibūdinimo rezultatai. Aptariamos šių kompozitų mechaninės, t.y. atsparumo gniuždymui, ir tirpumo SBF tirpale savybės.

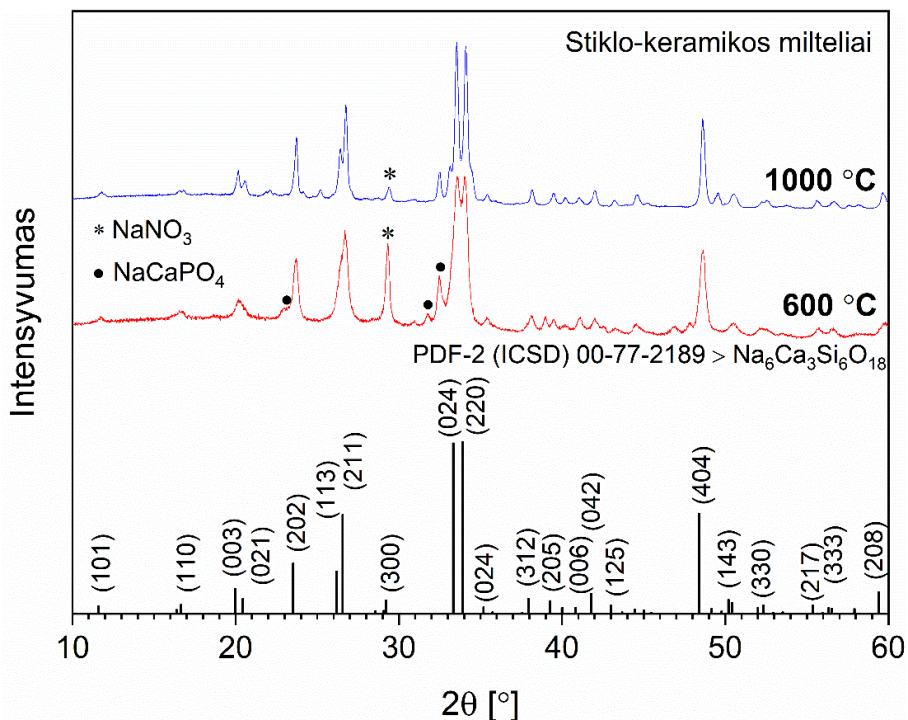
Stiklo keramika buvo susintetinta zolių-gelių metodu. Susintetinto Na-Ca-Si-P-O gelio termogravimetrinė analizė (TGA) buvo atlikta siekiant įvertinti optimalią bioaktyvaus stiklo kaitinimo temperatūrą, t.y. kad visos pašalinės medžiagos (nitratai, karbonatai, organinės medžiagos) pasišalintų ir būtų gauta kuo grynesnė medžiaga. Na-Ca-Si-P-O gelio terminės analizės TG/DSC/DTG kreivės yra pateiktos 1 pav. Masės pokyčio išvestinės kreivėje (DTG) matomi šeši pagrindiniai masės praradimo žingsniai. Pirmasis nedidelis masės sumažėjimas (~ 3%) stebimas iki 200 °C temperatūros. Jis priskiriamas adsorbuoto ir kristalizacinio vandens pasišalinimui. Antrasis 6% masės sumažėjimas yra stebimas 220–270 °C temperatūrų intervale. Šis etapas siejamas su pradinio gelio skilimu ir NOx dujų bei organinių fragmentų išsiskyrimu. Šį teiginį patvirtina iš DSC kreivės matomi egzoterminio proceso signalai (smailių viršūnės ties 222 °C ir 234 °C).



1 pav. Si-Ca-Na-P-O gelio, džiovinto 100 °C temperatūroje, TG/DTG ir DSC kreivės.

Kitas nedidelis svorio sumažėjimas apie 2% ties 334 °C (DTG kreivė), priskirtas organinių medžiagų skilimui ir absorbuoto vandens išsiskyrimui. Temperatūrų intervale 580–710 °C stebimas ganėtinai reikšmingas masės pokytis, tuo pačiu metu vyksta endoterminė reakcija (plati smailė DSC kreivėje 588, 673 ir 704 °C) su trimis maksimumais 605, 662 ir 702 °C DTG kreivėje. Šis žingsnis yra susijęs su tarpinių produktų skilimu ir stiklo keramikos kristalizacijos procesais. Pažymėtina, kad termiškai apdorojant Ca-P-Na-Si-O gelio miltelius, priklausomai nuo temperatūros, gali susidaryti daugiau nei viena kristalinė fazė. Paskutinis šiluminis endoterminis efektas, kurio masės netekimas yra ~ 5%, pastebimas esant 764 °C (DTG kreivė) ir 759 °C (DSC kreivė).

Ca-Na-Si-P-O gelio miltelių, iškaitintų 600 ir 1000 °C temperatūrose, XRD difraktogramos yra pateiktos 2 pav. Jose matosi difrakcijos atspindžiai ties $2\theta = 11,68^\circ, 16,73^\circ, 20,13^\circ, 23,64^\circ, 26,65^\circ, 33,56^\circ, 34,07^\circ, 35,33^\circ, 38,03^\circ, 39,46^\circ, 41,04^\circ, 41,95^\circ, 43,18^\circ, 48,60^\circ, 50,48^\circ, 52,18^\circ, 55,69^\circ, 56,50^\circ$ ir $59,69^\circ$, patvirtinantys kristalinės kietos medžiagos susidarymą 600 °C temperatūroje. Šie atspindžiai yra priskirti natrio kalcio silikato ($\text{Na}_6\text{Ca}_3\text{Si}_6\text{O}_{18}$) kristalinei fazei.



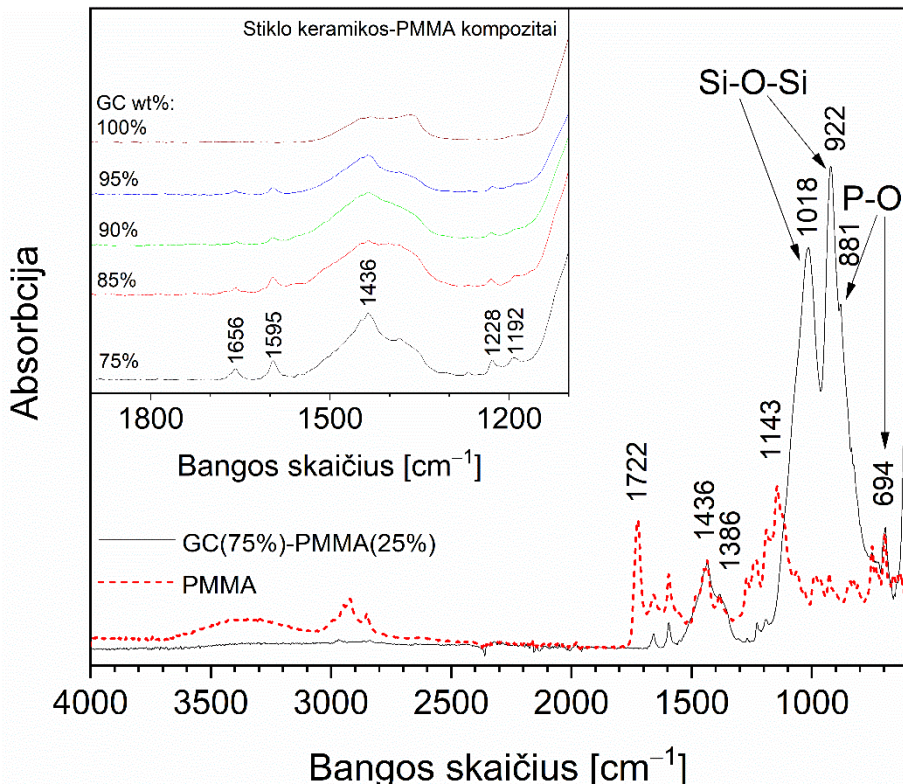
2 pav. Stiklo keramikos, iškaitintos 600 ir 1000 °C temperatūrose, Rentgeno spindulių difraktogramos. Difrakcinės PDF kortelės smailės atitinka $\text{Na}_6\text{Ca}_3\text{Si}_6\text{O}_{18}$ junginio [JCPDS Nr. 77-2189] kristalinę fazę.

Difraktogramose taip pat matomos ir kitų natrio kalcio silikatų, t.y. $\text{Na}_2\text{Ca}_2\text{Si}_3\text{O}_9$ [JCPDS Nr. 22-1455] ir $\text{Na}_4\text{Ca}_4\text{Si}_6\text{O}_{18}$ [JCPDS Nr. 79-1089], fazių smailės. Atspindžiai, pastebėti ties $2\theta = 23,12^\circ$, $31,04^\circ$, $31,75^\circ$ ir $32,50^\circ$, buvo priskirti buchvaldito (NaCaPO_4) [JCPDS Nr. 29-1193] fazei, o intensyvus difrakcinis atspindys ties $2\theta = 29,37^\circ$ buvo priskirtas natrio nitratui (NaNO_3 fazė [JCPDS nr. 36-1474]). Iškaitinus gelį 700 °C temperatūroje (duomenys nepateikti) ir 1000 °C temperatūroje, padidėjo medžiagos kristališkumas, tuo tarpu NaNO_3 fazės smailė XRD difraktogramoje šiek tiek sumažėjo. Šios smailės intensyvumo sumažėjimą lėmė medžiagos fazės pasikeitimas, nes esant aukštesnei temperatūrai nitratai skyla iki nitritų (NaNO_2 [JCPDS nr. 83-2254]) ir išsiskiria deguonis.

Norint nustatyti stiklo keramikos pasiskirstymą PMMA matricioje, buvo atlikta SEM analizė. Kai kuriose kompozito paviršiaus vietose buvo pastebėta netaisyklingų mikroduobučių, tuo tarpu gryno PMMA bandiniai atrodė tankūs. Tuštumų kiekis ir pasiskirstymas įvairiose tiriamose paviršiaus srityse skiriasi ir didėjant PMMA kiekiui didėja. Tai galima paaiškinti neorganinio-organinio kompozito paruošimo procedūra ir nevienodu stiklo keramikos

medžiagos pasiskirstymu polimerinėje matricoje. Apskaičiuota, kad netaisyklingų paviršiuje esančių tuštumų dydis yra $20 \times 10 \pm 5 \mu\text{m}$ ir $1 \times 0,5 \pm 0,25 \mu\text{m}$ atitinkamai GC(75 %)-PMMA(25%) ir GC(95%)-PMMA(5%) kompozituose. Manoma, kad susidariusios tuštumos gali lemti tam tikrą porėtumą, kuris yra viena iš svarbiausių medžiagų savybių, nes sudaro sąlygas osteoblastų ir mezenchiminių ląstelių (ląstelės galinčios diferencijuotis į daugelį audinių bei pasižyminčios imuninį atsaką reguliuojančiomis imunomoduliacinėmis savybėmis) migracijai ir proliferacijai, efektyviai vaskuliarizacijai, kaulo įaugimui, taip pat pagerina mechaninį dirbtinio implanto biomedžiagos ir ją supančio natūralaus kaulo tarpusavio ryšį.

Kompozitų cheminei sudėčiai įvertinti buvo atlikta FTIR spektroskopijos analizė. PMMA ir GC(75%)-PMMA(25%) kompozito sugerties FTIR spektrai pateikti 3 pav.

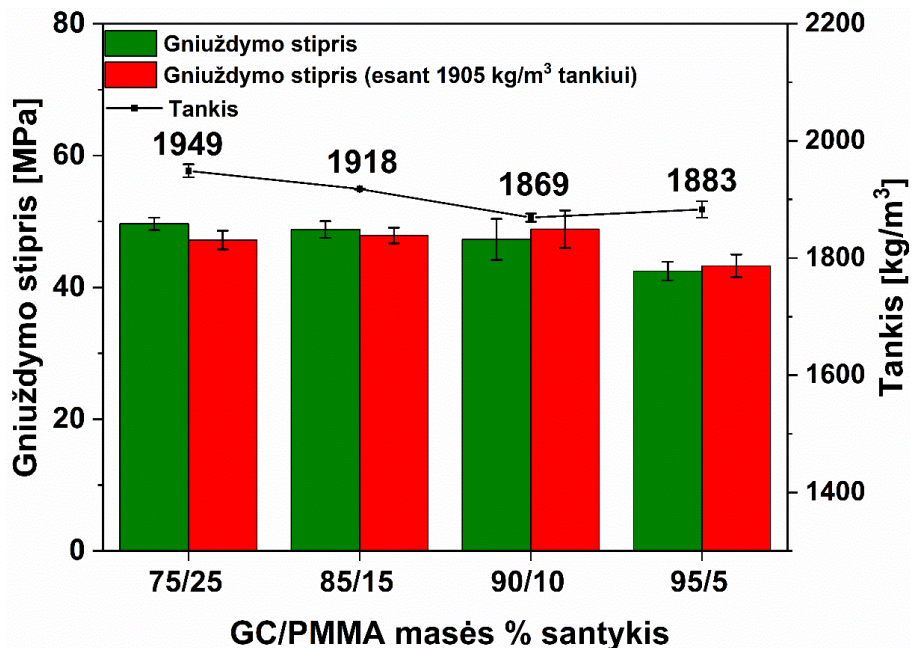


3 pav. GC(75%)-PMMA(25%) kompozito ir gryno PMMA FTIR spektrai. Įterptas grafikas: GC susintetinto 600 °C temperatūroje ir GC-PMMA kompozitų FTIR spektrai 1100-1900 cm^{-1} srityje.

Gryno PMMA FTIR spektre 1700-1100 cm^{-1} srityje matomos būdingos absorbcijos juostos, kurių smailės yra ties 1722, 1656, 1595, 1436, 1386, 1228, 1192 ir 1143 cm^{-1} . GC(75%)-PMMA(25%) kompozito FTIR spektre matomos plačios ir intensyvios absorbcijos juostos 1100-850 cm^{-1} srityje. Juostos, kurių smailės yra ties 1018 ir 922 cm^{-1} , priskirtos ortosilikato (SiO_4^{4-}) tetraedrinės grupės Si-O-Si virpesiams. Petys ties 881 cm^{-1} ir kelios smailės 600-550 cm^{-1} srityje susijusios su P-O virpesiais, kurie sutampa su mišriais Si-O-Si ryšio virpesiais. 1500-1350 cm^{-1} srityje plačios smailės, kurios priskirtos PMMA matricai, sutampa su karbonato grupės C-O virpesiais. Stiklo keramikos miltelių ir GC-PMMA kompozitų FTIR spektrai 1900-1100 cm^{-1} srityje pateikti 3 pav. įterptame grafike. Rezultatai rodo, kad didėjant PMMA kiekiui didėja ir PMMA virpesių intensyvumas (smailės esančios ties 1656, 1595, 1228 ir 1192 cm^{-1}). Be to, GC-PMMA kompozitų spektruose išnyksta intensyvi PMMA juosta, kuri matoma ties 1722 cm^{-1} ir priskiriama C=O tempimo virpesiams.

GC-PMMA kompozitų mechaninės savybės buvo ištirtos atliekant vienašio gniuždymo stiprumo bandymą (4 pav.). Šių kompozitų gniuždymo stipris (σ_i) buvo 42-50 MPa intervale (išmatuotas gryno PMMA granulių gniuždymo stipris buvo 126 MPa) ir mažėjo didėjant stiklo keramikos ir polimero santykiui. Kompozitų, kuriuose yra 75, 85 ir 90 % stiklo keramikos, gniuždymo stiprio vertės buvo labai panašios.

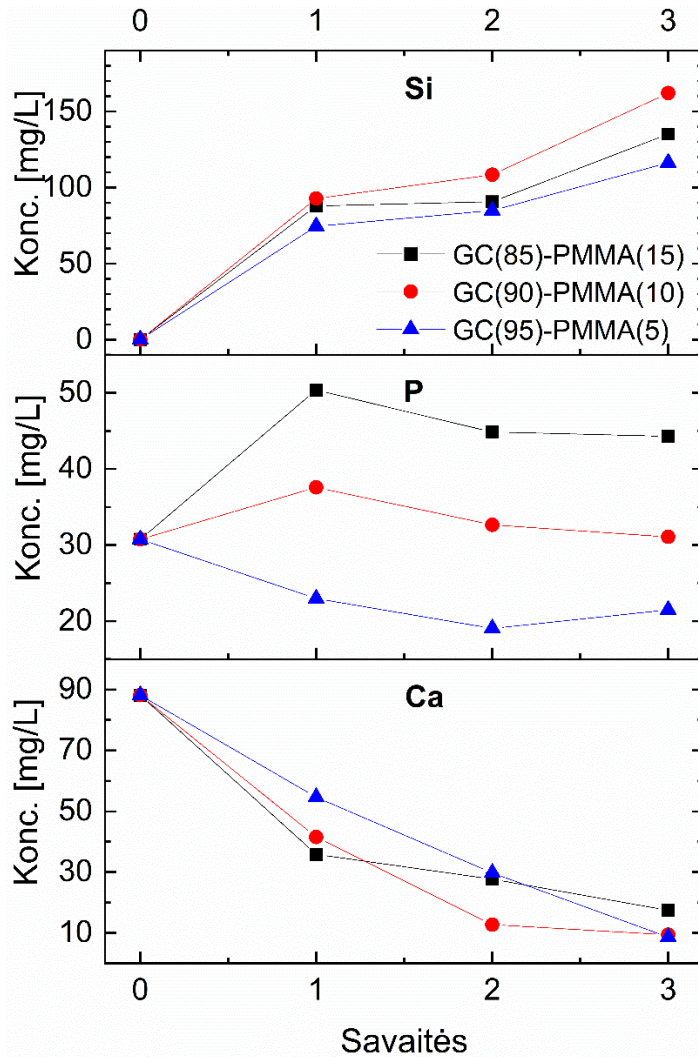
Rezultatai rodo, kad GC(90%)-PMMA(10%) kompozitas iš visų pagamintų medžiagų pasižymi didžiausiu stipriu ir mažiausiu tankiu. Gauti rezultatai leidžia teigti, kad pagaminti kompozitai gali būti potenciali medžiaga kaulinio audinio inžinerijai, kai nereikia ypatingai didelio stiprumo.



4 pav. GC-PMMA kompozitinių medžiagų mėginių tankis, išmatuotas stipris gniuždant ir numatomas stipris gniuždant esant 1905 kg / m³ tankiui.

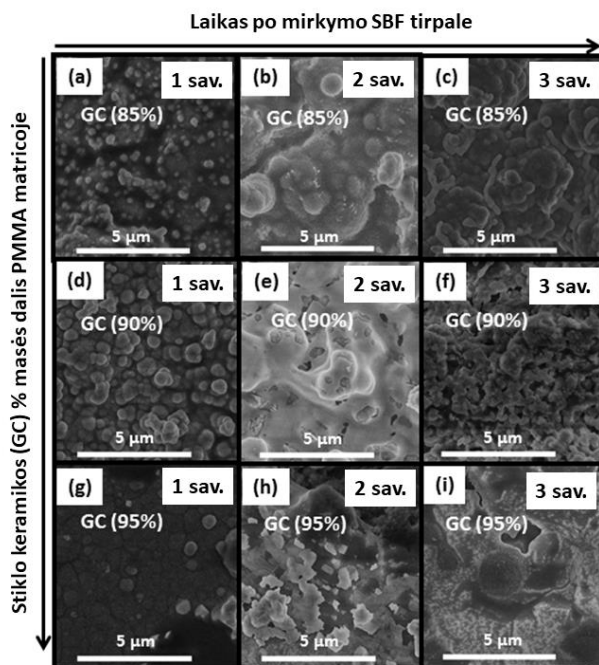
5 pav. pavaizduota Si, P ir Ca koncentracijos priklausomybė nuo GC(85%)-PMMA(15%), GC(90%)-PMMA(10%) ir GC(95%)-PMMA(5%) kompozitų mirkinimo SBF tirpaluose laiko. Silicio koncentracija SBF terpėje palaipsniui didėjo ir po 3 savaičių pasiekė 115 ppm (GC(95%)-PMAA(5%)), 135 ppm (GC(85 %)-PMMA(15%)) ir 165 ppm (GC(90%)-PMMA(10%)) atvejais. Didžiausias pokytis buvo aptiktas po pirmosios mirkinimo savaitės (70-90 ppm). Toks staigus Si koncentracijos padidėjimas rodo greitą stiklo keramikos tirpimą SBF. Didžiausia Si koncentracija nustatyta tirpale, kuriame buvo GC(90%)-PMMA(10%) kompozitas. Tai galima paaiškinti didesniu kompozito porėtumu ir didesniu paviršiaus aktyvumu. Kalcio koncentracija tirpinimo terpėje, priešingai, mažėja palaipsniui (ji svyruoja nuo 90 ppm iki 10-20 ppm), o fosforo kiekis kitimas svyravo. Po pirmosios pamerkimo savaitės GC(85%)-PMMA(15%) ir GC(90%)-PMMA(10%) kompozituose pastebėtas P koncentracijos padidėjimas, o po antrosios ir trečiosios tirpinimo savaitės - nedidelis sumažėjimas. GC(95%)-PMMA(5%) kompozito P koncentracija iš pradžių mažėjo, o paskutinę tirpinimo savaitę šiek tiek padidėjo. Paprastai šie procesai vyksta dėl tirpimo ir nusodinimo reakcijų, vykstančių stiklo keramikos paviršiuje, kuris yra sąlytyje su SBF. Greiti jonų mainai tarp stiklo keramikos paviršiaus ir tirpinimo terpės sukelia hidratuoto silicio dioksido turtingo sluoksnio susidarymą. Vėliau Ca²⁺ ir HPO₄²⁻ jonai

difunduoja link kompozito paviršiaus, todėl heterogeninės nukleacijos būdu susidaro kalcio fosfato keramika.



5 pav. Ca, P ir Si jonų koncentracijų kitimas SBF tirpaluose, kuriuose buvo pamerktos kompozitų tabletės.

6 pav. pavaizduotos tablečių, suformuotų iš GC-PMMA kompozitinių medžiagų ir 1, 2 ir 3 savaites mirkytų SBF tirpale, paviršiaus FE-SEM nuotraukos. Kompozitų paviršiuose po mirkymo susiformavo skirtingos struktūros, kurių morfologija priklausė nuo kompozito sudėties. Šie pokyčiai rodo jonų išplovimo ir difuzijos į kompozito paviršių procesus, o vėliau visų bandinių paviršiuje naujos keraminės medžiagos susidarymą.



6 pav. FE-SEM mėginių paviršiaus nuotraukos ((a)-(c) GC(85%)-PMMA(15%), ((d)-(f) GC(90%)-PMMA(10%) and ((g)-(i) GC(95%)-PMMA(5%) darytos po 1, 2 ir 3 savaičių mirkymo SBF tirpale.

EDS analizės duomenys leido padaryti išvadą, kad kompozito paviršiuje naujai susidariusios keraminės medžiagos cheminę sudėtį (duomenys nepateikti). Paviršiaus keramikos sudėtis buvo panaši į HAP, o vidutinis Ca : P santykis buvo 1,65 (n = 9).

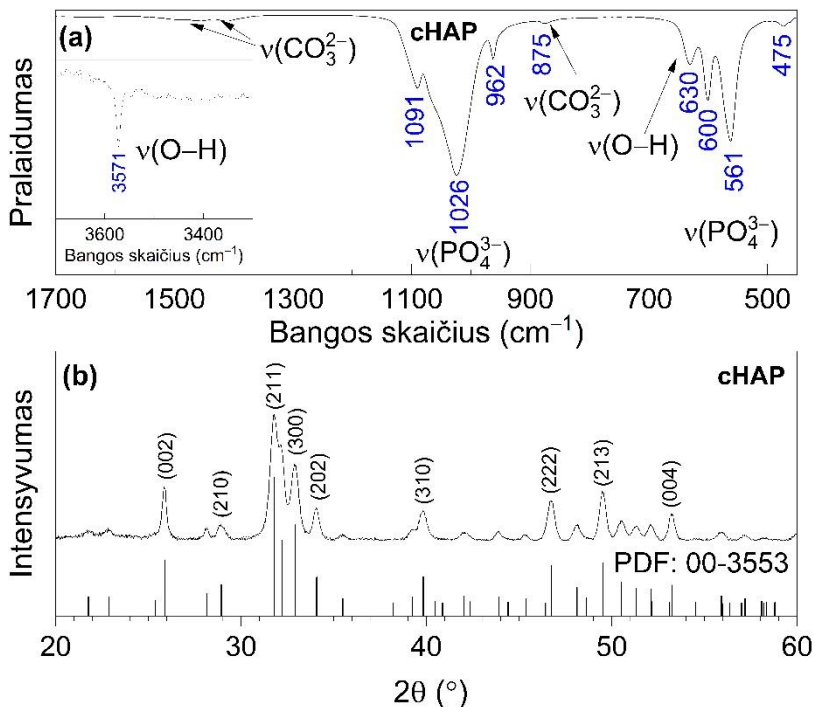
Kompozitų paviršiuje susiformavusios naujos medžiagos struktūra buvo tiriama XRD ir FTIR spektroskopijos metodais. GC(95%)-PMMA(5%). XRD analizė parodė, kad išsodinta neorganinė medžiaga yra žemo kristališkumo. XRD difraktogramoje esančios natrio kalcio silikato ($\text{Na}_6\text{Ca}_3\text{Si}_6\text{O}_{18}$) [JCPDS Nr. 77-2189] difrakcinių smailių intensyvumai sumažėjo lyginant jas su smailėmis, esančiomis difraktogramoje prieš kompozitų mirkymą SBF tirpale. XRD rezultatai leido teigti, kad po kompozitų mirkymo SBF tirpale susidarė žemo kristališkumo kalcio fosfato fazė.

Gauti rezultatai leido daryti išvadą, kad šiame darbe buvo sėkmingai paruošti neorganiniai-organiniai kompozitai, o jų paviršiuje iš SBF tirpalų buvo išsodintas mažo kristališkumo karbonato jonais pakeistas HAP.

2.2 Porėti cHAP-akrilato kompozitai, paruošti naudojant dipentaeritritolio heksaakrilatą (Miramer M600) ir želatiną

Šioje dalyje pateikiama nusodinimo metodu susintetinto cHAP ir suformuotų hibridinių neorganinių-organinių kompozitų tyrimo rezultatai. Kompozitiniai mėginiai buvo paruošti naudojant skirtingus kiekius želatinos, kuri tarnauja kaip porėtumą formuojanti medžiaga.

800 °C temperatūroje iškaitintų Ca-P-O miltelių XRD difraktograma bei FTIR spektras yra pateikti 7 pav. XRD difraktograma rodo, kad 800 °C temperatūroje susidarė kristalinis junginys su gerai išskirtomis difrakcijos smailėmis, atitinkančiomis cHAP standartinius duomenis [PDF# 00-3553].



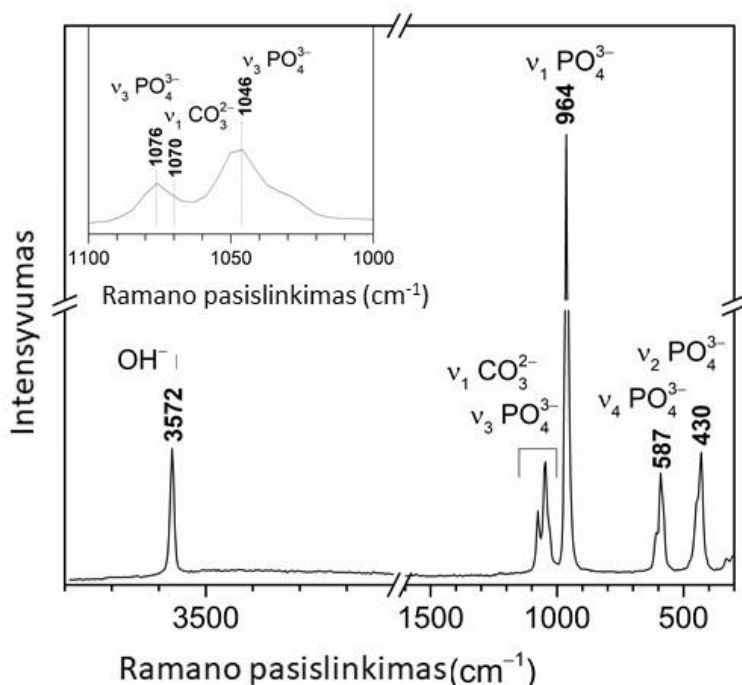
7 pav. cHAP miltelių, iškaitintų 800 °C temperatūroje, FTIR spektras (a) ir XRD difraktograma (b).

FTIR spektre matyti fosfato (PO_4^{3-}) ir karbonato (CO_3^{2-}) grupėms būdingos absorbcijos juostos. Absorbcijos juostos 1200-900 cm^{-1} srityje atsiranda dėl trigubo degeneruoto asimetrinio tempimo ir simetrinio tempimo P-O ryšiui būdingų virpesių, o juostos 630-450 cm^{-1} srityje atsiranda dėl apatitinių PO_4^{3-} grupių O-P-O trigubų degeneruotų lenkimo virpesių. Juostos 1550-1360 cm^{-1} srityje yra charakteringos CO_3^{2-} grupėms cHAP. Dvi išskirtinės smailės, pastebėtos ties 3571 cm^{-1} ir 630 cm^{-1} buvo priskirtos

cHAP struktūrinio –OH anijono ν_s ir ν_L virpesiams. CO_3^{2-} jonai gali pakeisti hidroksido (OH) arba fosfato (PO_4^{3-}) grupę.

Susintetinto cHAP struktūra buvo patvirtinta papildomai atlikus Rietveldo analizę, o apskaičiuoti kristalinės gardelės parametrai ($a = 9,4227(8) \text{ \AA}$ ir $c = 6,8843(6) \text{ \AA}$) sutampa su literatūroje nustatytais HAP kristalinės gardelės parametrais.

cHAP miltelių, iškaitintų $800 \text{ }^\circ\text{C}$ temperatūroje, Ramano spektras yra pateiktas 8 pav. PO_4^{3-} grupei būdingi virpesiai yra $1100\text{-}1000 \text{ cm}^{-1}$ srityje, smailės ties 964 cm^{-1} (intensyviausia juosta), 587 cm^{-1} ir 430 cm^{-1} . Karbonatui būdinga juosta Ramano spektre atsiranda ties 1070 cm^{-1} , tačiau ji persidengia su juostomis, būdingomis PO_4^{3-} fosfato grupei (8 pav. įterptas paveikslukas).

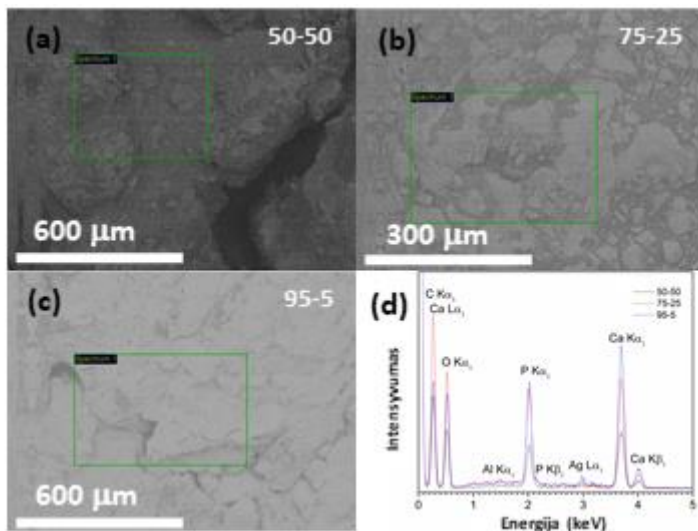


8 pav. cHAP miltelių, iškaitintų $800 \text{ }^\circ\text{C}$ temperatūroje, Ramano spektras (persidengiančios PO_4^{3-} ir CO_3^{2-} grupėms būdingos juostos pateiktos įterptame paveiksle).

Spektre esanti juosta ties 3572 cm^{-1} yra priskirta O-H grupės tempimo virpesiams. Ramano spektras sutampa su literatūros duomenimis, o intensyviausios PO_4^{3-} juostos ties 964 cm^{-1} skilimo nebuvimas rodo homogenišką karbonato jonų inkorporavimą į HAP kristalinę gardelę.

Akrilato-želatinos-cHAP kompozitų FE-SEM nuotraukos ir atitinkami EDS spektrai pateikti 9 pav. SEM nuotraukos parodė, kad cHAP

aglomeruotos dalelės yra homogeniškai įsiterpusios išsitinėje polimerinėje matricoje. Kai kuriose kompozito granuliu dalyse taip pat pastebėta tuštumų ir didelių cHAP aglomeratų blokų. Kompozitų paviršiuje buvo galima aptikti ir tuštuminių tarpų (pavyzdžiui, 9 pav. (a) nuotraukoje matosi 50/50 kompozito paviršiuje esanti 300 μm pločio tuštuma).

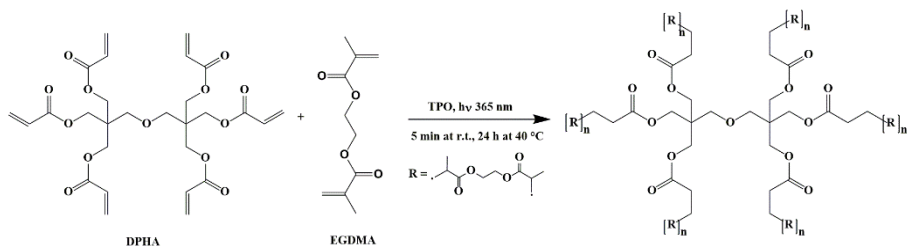


9 pav. ((a)-(c)) Akrilato-želatinos-cHAP kompozitų paviršiaus SEM nuotraukos ir (d) atitinkami EDS spektrai.

Suformuotų kompozitų paviršiaus sudėtis buvo nustatyta atlikus EDS analizę. Apskaičiuota, kad vidutinis Ca/P atominių % santykis yra 1,6 ($n = 11$), kuris šiek tiek keitėsi analizuojant skirtingas mėginio paviršiaus vietas. Kitų kompozitų elementinė sudėtis buvo panaši.

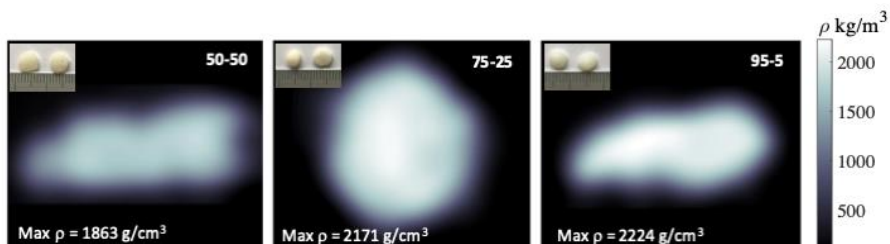
Konkretūs komponentai daugiakompozitiniuose hibridiniuose karkasuose buvo patvirtinti FTIR spektroskopijos analizės.

Supaprastintas tarpmolekulinis monomerų DPHA ir EGDMA susikabinimas veikiant UV spinduliutei parodytas 10 pav.



10 pav. Supaprastintas tarpmolekulinis monomerų DPHA ir EGDMA susikabinimas veikiant UV spinduliutei.

Kompiuterinė tomografija (KT) buvo naudojama mėginių tankiui įvertinti. Iš 11 pav. pateiktų akrilato-želatino-cHAP mėginių skerspjūvio KT vaizdų (skenavimas atliktas esant 80 kV įtampai) (įterptiniuose paveikslukuose yra mėginio skaitmeninės nuotraukos) matyti, kad skirtingos sudėties mėginių tankis skyrėsi.

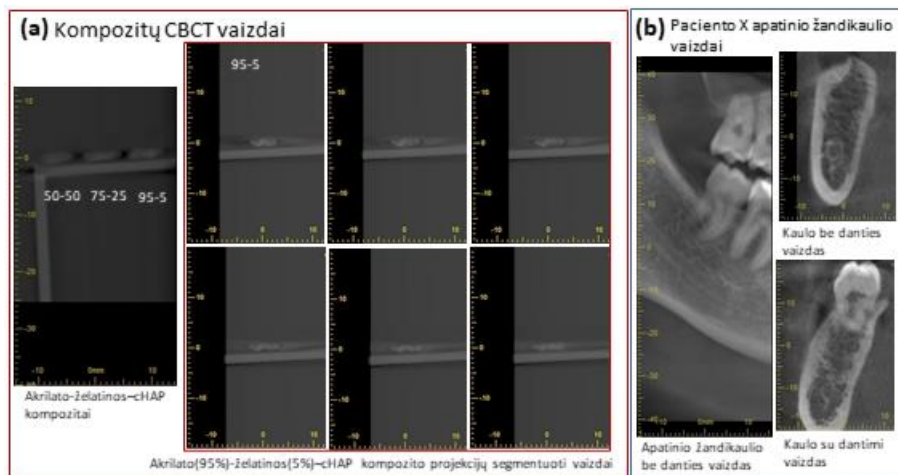


11 pav. Akrilato-želatinos-cHAP kompozitų skersinio pjūvio kompiuterinės tomografijos nuotraukos ir atitinkama tankio skalė (įterptiniuose paveiksluose pavaizduoti atitinkami mėginiai; liniuotės skalės viena padala = 1 mm).

Apskaičiuotas 50/50, 75/25 ir 95/5 kompozitinių mėginių vidutinis tankis yra 1863, 2171 ir 2224 kg/m^3 . Tankio skirtumą daugiausia lėmė skirtinga medžiagos sudėtis, tačiau tankis šiek tiek skyrėsi ir bandinio viduje - medžiagos tankis centrinėje srityje buvo didesnis nei išoriniame sluoksnyje. Daugiakompozitinių medžiagų tankio vertės nepakito, kai skenavimas buvo atliekamas esant 110 kV įtampai.

Išsamiais tyrimais įrodyta, kad mikrokompiuterinė tomografija leidžia nustatyti kaulinio audinio tankį bei naujo kaulo formavimąsi visame kompozitinio mėginio gylyje.

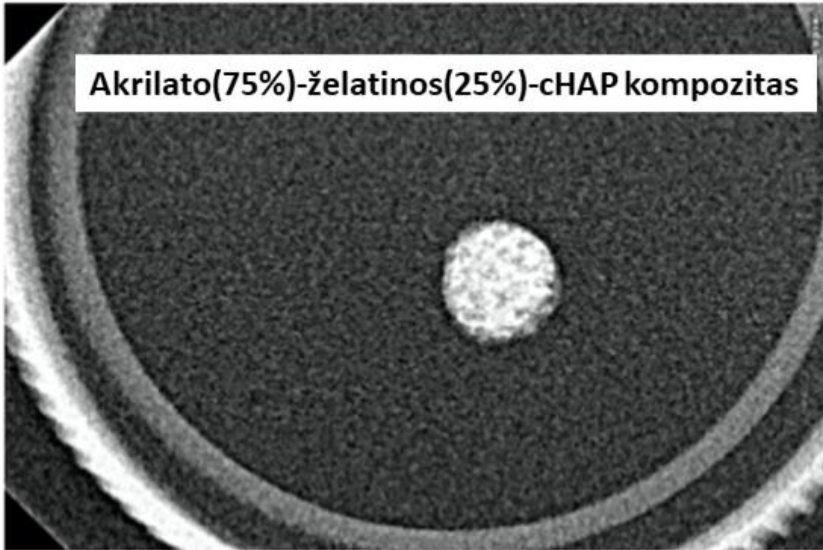
Siekiant išsamiau apibūdinti vidinę mėginių struktūrą, buvo atlikta kūginio spindulio kompiuterinės tomografijos (CBCT) analizė. 12(a) pav. parodytas bendras 50/50, 75/25 ir 95/5 kompozitų CBCT vaizdas, taip pat 95/5 kompozito kelių projekcijų segmentuoti vaizdai (6 iš 24).



12 pav. CBCT nuotraukos (a) akrilato-želatinos-cHAP kompozitai ir segmentuoti vaizdai (6 iš 24) 95/5 kompozito, (b) X paciento apatinio žandikaulio ir kaulo be danties bei su dantimi vaizdai (CBCT buvo atlikta tomis pačiomis sąlygomis).

CBCT duomenys rodo, kad rentgenografinių vaizdų kontrastas yra ganėtinai didesnis. Pats kompozitas dažniausiai yra radiolucentinis. Tačiau šiame darbe pagamintuose kompozituose yra apatito dalelių, kurios yra rentgenokonstrastinės. Kompozitų vaizduose taip pat yra šiek tiek "rūko" ir tai buvo priskirta išsklaidytai rentgeno spinduliutei. Norint palyginti objekto kontrastą, paciento X apatinio žandikaulio atvaizdai pateikti 12(b) pav. Šie intraoraliniai CBCT vaizdai buvo padaryti tomis pačiomis sąlygomis kaip ir pagamintų karkasų. Palyginus vaizdus matyti, kad dantų kaulas pasižymi didesniu kontrastu, o tai rodo, kad pagamintus daugiasluoksnius kompozitus galima lengviau atskirti po implantacijos stebint dominančias anatomines struktūras.

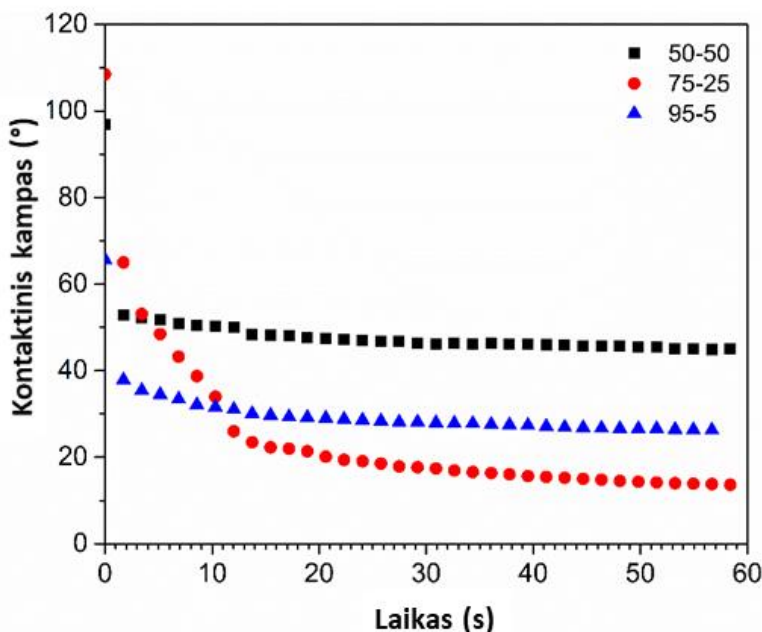
Siekiant išsamiau įvertinti struktūrinės savybes, naudota ir įprastinė dantų rentgenografija. 13 pav. pateikiamas tipinio akrilato (75 %), želatinos (25 %) ir cHAP kompozito rentgenografinis vaizdas.



13 pav. Akrilato(75%)-želatinos(25%)-cHAP kompozito įprastinės dantų rentgenografijos nuotrauka.

Dėl didesnio neorganinės medžiagos radiologinio tankio, lyginant su organinės matricos tankiu, kompozito nuotraukoje aiškiai matoma apatitinė fazė ir homogeniškas cHAP pasiskirstymas visame karkase. Tai leidžia daryti prielaidą apie galimybes pasiekti radiografinį kaulinio audinio ir atkuriamojo karkaso diferencijavimą bei įvertinti struktūrinius pokyčius, kai jis pakeičiamas "naujai užaugintu kaulu".

Kompozitinių karkasų drėkinimosi savybės buvo įvertintos matuojant vandens, nuspalvinto metileno mėlynuoju dažikliu, kuris dažnai naudojamas kaip katijoninis dažiklis citologiniams mėginiams tirti, kontaktinį kampą. 14 pav. pateikta lašų kontaktinio kampo priklausomybė nuo laiko.



14 pav. Akrilato-želatinos-cHAP kompozitų statinių lašų kontaktinių kampų vertės.

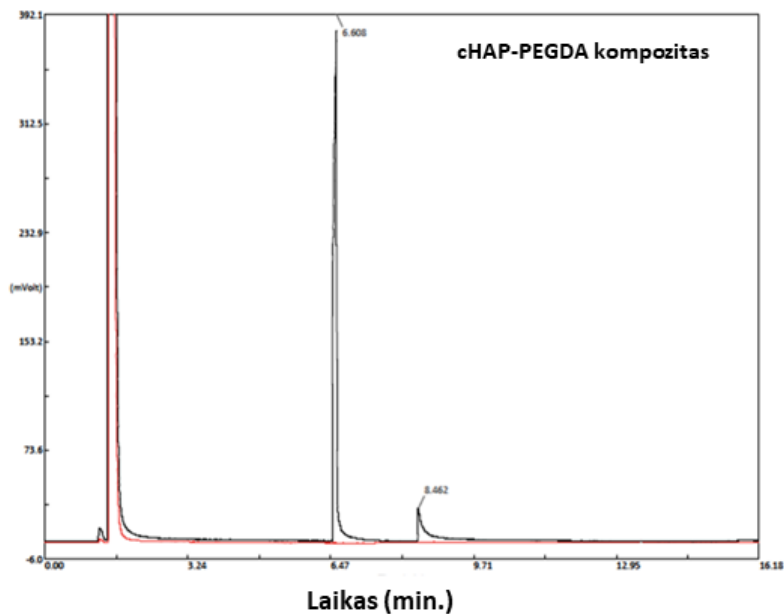
Per kelias sekundes visų mėginių kontaktinis kampas sumažėjo 15-20° (pradiniai vidutiniai kampai, išmatuoti 50/50, 75/25 ir 95/5 kompozitams, atitinkamai 91°, 100° ir 67°). Po to kampas palaipsniui mažėjo vis lėčiau. Galutinės vertės po 60 sekundžių buvo 47,6° ir 31,4° atitinkamai 50/50 ir 95/5 kompozitams. Vandens lašo ir 75/5 kompozito sąveika skyrėsi: po pradinio sumažėjimo kontaktinis kampas gana greitai sumažėjo nuo 63,4° iki 21,5° (per 15 s) ir toliau mažėjo, kol po 50 s buvo nustatyta, kad galutinis kampas yra 16,6°, o tai rodo, kad tai buvo labiausiai hidrofilinis tiriamasis paviršius. Šie kontaktinio kampo skirtumai buvo paaiškinti paviršiaus morfologijos skirtumais, kurie priklausė nuo kompozito sudėties.

DPHA, EGDMA ir želatinos suirimo greičiai skiriasi, todėl DPHA/EGDMA, želatinos ir cHAP derinys kaulinio audinio inžinerijoje gali suteikti tam tikrų privalumų, nes kompozitai gali suirti greičiau nei gryna akrilato pagrindu pagaminta polimerinė matrica. Biokeramikos ir želatinos hidrofiliskumas turėtų sudaryti sąlygas vandeniui lengviau prasiskverbti į akrilato pagrindo matricą ir taip skatinti hidrolitinį skilimą ten, kur sąveikauja kompozitinis karkasas ir kūno skysčiai, o mikrostruktūrinė karkasų architektūra galėtų sustiprinti naujo kaulo mineralizaciją kompozitinės medžiagos viduje ir sudaryti sąlygas gilesniam audinių įaugimui.

2.3 Porėtas hidroksiapatito (cHAP)-poli(etilenglikolio) diakrilato (PEGDA) kompozitas, paruoštas naudojant putojimo agentą azodikarbonamidą (ADCA)

Šiame skyriuje aprašomas porėtų cHAP-PEGDA kompozitų, paruoštų 180-200 °C temperatūroje, charakterizavimas dujų chromatografijos (GC), diferencinės skenuojančiosios kalorimetrijos (DSC), optinės mikroskopijos ir kompiuterinės tomografijos metodais. Susiformavusių porėtų mėginių hidrofiliškumui apibūdinti buvo tirta vandens, nudažyto metileno mėlynuoju dažikliu, sorbcija.

Iš GC kreivių, pateiktų 15 pav. matyti, kad cHAP-PEGDA medžiagoje lyginant su etaloninio mėginio GC kreive nėra nei polietilenglikolio diakrilato, nei etilenglikolio dimetakrilato likučių.



15 pav. cHAP-PEGDA kompozito (raudona spalva) ir standarto mišinio, sudaryto iš PEGDA ir EGDMA (juoda spalva), GC kreivės.

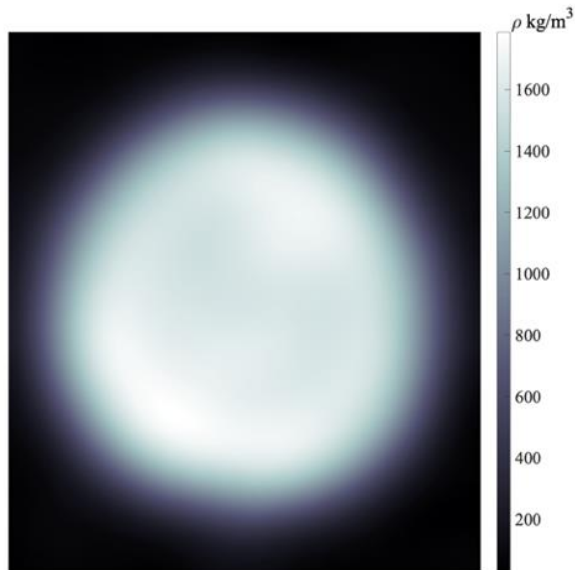
Tačiau diferencinės skenuojančios kalorimetrijos analizė patvirtino, kad kompozituose yra azodikarbonamido likučių.

Suformuotų kompozitų porėtumui įvertinti buvo atlikta optinės mikroskopijos analizė. Reikalingas cHAP-PEGDA kompozito optinės mikroskopijos vaizdai pateikti 16 pav.



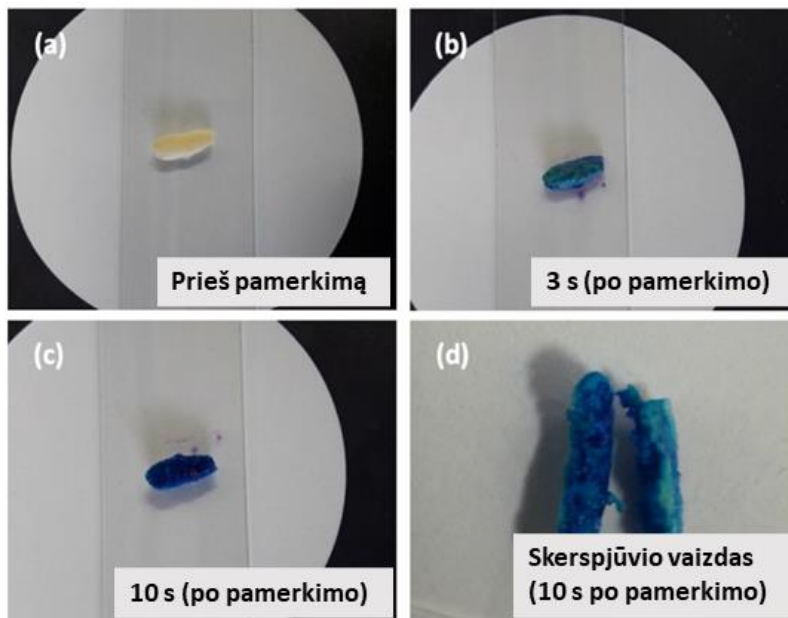
16 pav. Reikalingas cHAP-PEGDA kompozito optinio mikroskopo nuotraukos.

Optinės mikroskopijos nuotraukos patvirtino mėginių mikroporėtumą, o tai leidžia daryti išvadą apie geresnę skystosios fazės difuziją į vidinę kompozitinių karkasų dalį. Verta pažymėti, kad optinės mikroskopijos rezultatai sutapo su CT rezultatais. Reikalingas cHAP-PEGDA kompozito kompiuterinės tomografijos vaizdas pateiktas 17 pav. Visame karkase pastebėtas tankio skirtumas buvo susijęs su putojančia medžiaga ADCA ir apdorojimo sąlygomis.



17 pav. Reikalingas cHAP-PEGDA kompozito skersinio pjūvio kompiuterinės tomografijos nuotrauka. (Skanuota naudojant 80 kV Rentgeno spindulių energiją)

Toluidino mėlynojo dažiklio vandeninis tirpalas (0,05 %) buvo naudojamas hidrofiliškumui ir skystos fazės absorbcijai kompozituose patvirtinti. Reprezentatyvių cHAP-PEGDA kompozitų vaizdai prieš ir po dažų absorbcijos pateikti 18 pav.



18 pav. Iš cHAP-PEGDA kompozito pagamintų karkasų skaitmeninės nuotraukos (a) prieš pamerkimą ir (b-d) po pamerkimo į vandenį, nuspalvintą Toluidino mėlynuoju dažikliu).

Absorbcijos pokyčiai ant mėginių paviršiaus naudojant Toluidino mėlynojo dažiklio vandeninį tirpalą buvo stebimi po 1, 3, 5 ir 10 s. Pastebėtas lašo pralaidumas, kuris buvo susijęs su porėta suformuotų karkasų struktūra. Kompozito skerspjūvio vaizdas (18(d) pav.) patvirtino porėtą pagaminto kompozitinio karkaso struktūrą. Bendri rezultatai rodo, kad ADCA yra tinkama medžiaga norint formuoti akytos struktūros karkasus.

IŠVADOS

1. Pasiūlyti vandeniniai nusodinimo ir zolių-gelių sintezės metodai bei skirtingi kaitinimo režimai yra tinkami norint susintetinti žemo kristališkumo ir karbonato jonų turinčius hidroksiapatito (HAP) bei stiklo keramikos (Na-Ca-Si-O) miltelius.

2. Homogeniški hibridiniai kompozitai, sudaryti iš stiklo keramikos ir polimetilmetakrilato (GC(85%)-PMMA(15%), GC(90%)-PMMA(10%), GC(95%)-PMMA(5%)) buvo sėkmingai paruošti fotopolimerizacijos reakcijos būdu.

3. Nustatyta, kad GC-PMMA kompozitų mechaninis atsparumas gniuždymui buvo 42,5–49,6 MPa intervale, o 90% GC ir 10% PMMA sudėties kompozitai pasižymėjo didžiausiu stiprumu bei mažiausiu tankiu.

4. Nustatyta, kad GC(90%)-PMMA(10%) kompozito keramikos fazės tirpimas SBF tirpale buvo didžiausias. Konstatuota, kad naujai išsodinta medžiaga yra dalinai amorfinė, kurios sudėtis panaši į HAP (vidutinis Ca/P atomų% santykis = 1,65). FTIR analizė parodė, kad po tirpinimo SBF tirpale naujai susidaręs keramikos sluoksnis yra mažo kristališkumo kalcio fosfatas, kurio kristalinė fazė yra karbonato jonais A- ir B- pakeistas HAP.

5. Pasiūlytos kopolimerizacijos reakcijos yra tinkamos norint paruošti hidrofilinėmis savybėmis pasižyminčius daugianarius kompozitus, susidedančius iš akrilato (DPHA/EGDMA), cHAP ir želatinos, bei didelio porėtumo cHAP-PEGDA kompozitus, panaudojant putojimo agentą azodikarbonamidą (ADCA).

6. Morfologiniai tyrimai parodė, kad cHAP dalelės buvo homogeniškai įterptos į ištisinę polimerinę matricą ir kad suformuotuose mėginiuose buvo tuštumų bei didelių apatitinės fazės aglomeratinių blokų skirtingose sudėtinių granulių dalyse. TG analizė patvirtino, kad likusi neorganinės medžiagos masė gerai atitiko pradinį cHAP kiekį.

7. Daugiakomponentinė akrilato-cHAP-želatinos mėginių sudėtis buvo patvirtinta FTIR spektroskopijos metodu. IR spektruose buvo identifikuotos juostos, kurios buvo priskirtos C=C jungčiams, ir tai parodė, kad paruoštuose mėginiuose po UV spinduliuotės yra likę DPHA ir EGDMA monomerų.

8. KT analizė parodė, kad akrilato-cHAP-želatinos mėginių vidutinis tankis buvo skirtingas ir kad kiekvieno mėginio centrinės dalies tankis buvo didesnis nei išorinio sluoksnio. Konusinio pluošto kompiuterinės tomografijos (KPKT) analizė atskleidė, kad danties kaulo rentgenografinis kontrastas yra didesnis nei pagamintų daugiakompozicinių medžiagų, ir tai rodo, kad po implantacijos būtų lengviau identifikuoti dominančias anatomines struktūras. Taip pat, įprastinės rentgenografijos gauti vaizdai parodė skirtingą mėginių rentgenografinį tankį, kuris patvirtino cHAP komponento homogenišką pasiskirstymą visame mėginyje.

9. Kontaktinio kampo matavimai parodė, kad paruoštų mėginių hidrofiliškumas priklausė nuo kompozito sudėties ir morfologijos. Akrilato(75%)-želatinos(25%)-cHAP kompozitai pasižymėjo geriausiomis drėkinimo savybėmis, ir jų drėkinimo kampas buvo 16,6°. Tai parodo šių

mėginių perspektyvumą modeliuojant junginių porėtumo ir hidrofiliškumo savybes bei šių kompozitinių junginių potencialias galimybes skatinti implantų į kaulinį audinį integraciją.

10. Tyrimų rezultatai rodo, kad paruošti ir ištirti kompozitai, GC-PMMA bei lc-cHAP – PEGDA, yra perspektyvūs pritaikant juos kaulinio audinio atstatymo procedūrose.

CURRICULUM VITAE

Gyvenimo aprašymas

Vardas, Pavardė Ričardas Golubevas
Gimimo metai 1983 m.
Gyvenama vieta Vilnius, Lietuva
El. paštas Ricardas.G@gmail.com
Šeimyninė padėtis Vedęs, sūnus.

Išsilavinimas

- 2015 – dabar Vilniaus universitetas, Chemijos ir Geomokslų fakultetas, Doktorantūros studijos, chemija
- 2006 – 2008 Vilniaus Gedimino technikos universitetas, Magistro laipsnis, aplinkos apsauga
Papildoma informacija: Aplinkos apsaugos katedroje apgintas magistrinis darbas, kurio tema - importuojamų vaisių cheminiai bei radiologiniai tyrimai ir vertinimas. Studijų kryptis - aplinkos apsaugos inžinerija.
- 2002 - 2006 Vilniaus universitetas, Chemijos fakultetas chemija
Papildoma informacija: Studijų specializacija - neorganinė chemija.
- 1990 - 2002 Varėnos Ryto vidurinė mokykla
Papildoma informacija: Sustiprinta matematinė klasė. Aktyviai dalyvavau užklasinėje veikloje, Jaunųjų mokslininkų konkursuose, olimpiadose.

Kvalifikacijos kėlimas

- The iPrint institute, University of Applied Sciences Western, Switzerland, Fribourg Skaitmeninės spaudos rašalų spausdinimo kursai, praktiniai laboratorijos kursai rašalų inžinerijos ir rašalų chemijos srityje
- X-Rite Spalvų valdymo sprendimai
- Nacionalinis maisto ir veterinarijos rizikos vertinimo institutas Analitinių metodų validavimas
- Kalbų mokykla "lingua perfecta" Anglų kalbos tobulinimosi kursai, 2010 m. vasaris – birželis, C1 ir C2 lygis
- Užsienio kalbų mokymo centras, VšĮ Anglų kalbos tobulinimosi kursai, 2007 m. kovas – rugpjūtis

Papildoma informacija: Įgytas B2 lygio anglų kalbos žinių sertifikatas.

NRD, UAB

Kompiuterinis raštingumas pažengusiems, 2007 m. 40 akademinų valandų

Darbo patirtis

2021 m. rugpjūčio - dabar
AB „Utenos trikotažas“ Tyrėjas-technologas. Tekstilės dažymo technologinio proceso optimizavimas. Dažymo technologinė-eksperimentinė veikla ir diegimas gamyboje.

2012 m. lapkričio – 2021 m. rugpjūčio
UAB „Veika“ Tyrėjas. Pigmentinių pastų, dažų vandens pagrindu, dažų tirpiklių pagrindu, gamyba ir tyrimai. Efektinės spaudos skirtos lauko reklamai projekto vykdymas. Naujų produktų eksperimentinė gamyba, eksperimentų planavimas, eksperimentinės gamybos organizavimas, technologijų perkėlimas iš eksperimentinės į gamybines apimtis, žaliavų paieška ir žaliavų kokybės vertinimas, bendravimas su žaliavų gamybos/tiekimo atstovais, techninių-technologinių nesklaidumų nustatymas ir šalinimas.

2005 – 2012
Nacionalinis maisto ir veterinarijos rizikos vertinimo institutas Laboratorijos departamento Cheminių tyrimų skyriaus vyr. inžinierius. Darbas su dujų chromatografijos, dujų chromatografijos-masių spektrometrijos analitine įranga.

2004 -2006
Vilniaus universitetas Chemijos fakulteto Bendrosios ir neorganinės chemijos katedros anglinių tyrimų laboratorijos asistentas.

Kalbiniai įgūdžiai

Lietuvių gimtoji kalba
Anglų žodžiu Gerai, raštu Gerai
Rusų žodžiu Gerai, raštu Pagrindai
Prancūzų žodžiu Pagrindai, raštu Pagrindai

Darbo su kompiuteriu

Specialisto lygmuo

Dominančios mokslinės sritys

Zolių-gelių sintezė, neorganinių-organinių kompozitų sintezė, UV polimerizacija ir pritaikomumas 3D spausdinimui, biosuderinamų kompozitų sintezė

CONFERENCES

1. Preparation and characterization of the inorganic-organic (bioglass-poly(methyl methacrylate)) composite for bone tissue engineering.

Golubevas, Ričardas; Žarkov, Aleksej; Gražėnaitė, Eglė; Alinauskas, Laurynas; Garškaitė, Edita; Kareiva, Aivaras

ISSN: 1822-7759

Advanced materials and technologies : the 18th international conference-school, 27-31 August 2016, Palanga, Lithuania.

2. Preparation and Characterization of the Inorganic-Organic (Bioglass-Poly (Methyl Methacrylate) Composite for Bone Tissue Engineering

There is no future without the past“ : science on the interface of XIX-XXI centuries: the international conference dedicated to the 215-th birth anniversary of Ignacy Domeyko : proceedings book, Vilnius, 2017. Vilnius: Vilniaus universiteto leidykla, 2017.

3. Investigation of high-quality glass-ceramic (GC) and polymerized methyl methacrylate (PMMA) composite for regenerative medicine.

R. Golubevas, A. Zarkov, Z. Stankeviciute, L. Alinauskas, E. Garskaite, A. Kareiva

„Šiuolaikinė medžiaga ir technologija 2018“

20 – oji tarptaurinė konferencija – mokykla, Rugsėjučio 27-31, 2018, Palanga, Lithuania.

4. Preparation of porous glass-ceramic (gc) and polymerized 1,6-hexanediol diacrylate (hdda) composite using free radical copolymer crosslink reactions and blowing agent for bone tissue engineering.

Golubevas, Ričardas; Žarkov, Aleksej; Alinauskas, Laurynas; Kareiva, Aivaras; Garškaitė, Edita

EcoBalt 2018 : the international conference proceedings book, October 25-27, 2018, Vilnius, Lithuania.

PUBLICATIONS

1. Acrylate-gelatin-carbonated hydroxyapatite(cHAP) composites for dental bone-tissue applications.

Golubevas, Ričardas; Stankevičiūtė, Živilė; Žarkov, Aleksej; Golubevas, Raimundas; Hansson, Lars; Raudonis, Rimantas; Kareiva, Aivaras; Garškaitė, Edita

Laisvai prieinamas internete / Unrestricted. eISSN: 2633-5409 ; DOI: 10.1039/D0MA00498G

Materials advances. London : The Royal Society of Chemistry. 2020, vol. 1, no. 6, p. 1675-1684.

This article is part of the themed collections: Materials Advances HOT Article Collection and International Open Access Week 2020

2. Fabrication and investigation of high-quality glass-ceramic (GC)-polymethyl methacrylate (PMMA) composite for regenerative medicine.

Golubevas, Ričardas; Žarkov, Aleksej; Alinauskas, Laurynas; Stankevičiūtė, Živilė; Balčiūnas, Giedrius; Garškaitė, Edita; Kareiva, Aivaras

Laisvai prieinamas internete / Unrestricted. ISSN: 2046-2069 ; DOI: 10.1039/c7ra05188c

RSC advances. Cambridge : Royal Society of Chemistry. 2017, Vol. 7, iss. 53, p. 33558-33567.

1 publikacija / 1st publication

Fabrication and investigation of high-quality glass ceramic (GC)–polymethyl methacrylate (PMMA) composite for regenerative medicine

Ricardas Golubevas, Aleksej Zarkov, Laurynas Alinauskas, Zivile Stankeviciute.

RSC Adv., 2017, 7, 33558

DOI: 10.1039/c7ra05188c

<https://pubs.rsc.org/en/content/articlelanding/2017/ra/c7ra05188c>

2 publikacija / 2nd publication

**Acrylate–gelatin–carbonated hydroxyapatite
(cHAP) composites for dental bone-tissue
applications**

Ricardas Golubevas, Zivile Stankeviciute, Aleksej Zarkov,
Raimundas Golubevas, Lars Hansson, Rimantas Raudonis, Aivaras
Kareiva and Edita Garskaite.

Mater. Adv., 2020, (1, 1675)

DOI: 10.1039/d0ma00498g

<https://pubs.rsc.org/en/content/articlelanding/2020/ma/d0ma00498g>

Vilniaus universiteto leidykla
Saulėtekio al. 9, III rūmai, LT-10222 Vilnius
El. p. info@leidykla.vu.lt, www.leidykla.vu.lt
Tiražas 15 egz.